Probing an interacting Bose gas in a quasi-two-dimensional trap

by

Shih-Kuang Tung

B.A., National Tsing Hua University, 1999

M.S., National Tsing Hua University, 2001

A thesis submitted to the

Faculty of the Graduate School of the

University of Colorado in partial fulfillment

of the requirements for the degree of

Doctor of Philosophy

Department of Physics

2010

This thesis entitled:
Probing an interacting Bose gas in a quasi-two-dimensional trap
written by Shih-Kuang Tung
has been approved for the Department of Physics

E. A. Cornell

D. S. Jin

Date _____

The final copy of this thesis has been examined by the signatories, and we find that both the content and the form meet acceptable presentation standards of scholarly work in the above mentioned discipline.

Tung, Shih-Kuang (Ph.D., Physics)

Probing an interacting Bose gas in a quasi-two-dimensional trap

Thesis directed by Prof. E. A. Cornell

A fluctuating regime associated with the Berenzinskii-Kosterlitz-Thouless (BKT) transition is studied in a two-dimensional system of near-degenerate bosons (^{87}Rb atoms). Two imaging procedures, the *in-situ* imaging method and the focusing-imaging method, are implemented to image the coordinate-space and momentum-space density distributions. The scaled compressibility is extracted from the coordinate-space density distributions obtained from *in-situ* images. Comparing the measured compressibility to the prediction from our semiclassical mean-field model, an onset of a regime which is beyond the mean-field prediction is identified and first resolved at phase-space density $n\lambda^2 \gtrsim 3$. Information about the coherence of the system is extracted from the momentum-space distributions obtained from the focusing images. The spatial extent of the coherence at a size of the high density region in the system only appears at a distinguishably higher phase-space density of $n\lambda^2 \approx 8$. Therefore, a very interesting regime that is beyond mean-field prediction, but not yet a quasicondensate, is identified. This regime, which does not exist in three dimensions, is a product of the enhanced interactions associated with reduced dimensionality.

Dedication

To Claire, Tse-Chi, Mei-Shia, and Shih-Hong.

Acknowledgements

Until this day, I still feel lucky that I can be one of those guys working at JILA. Therefore, the first person I should give my gratitude to is my boss, Eric. Not only he gave me this opportunity to work with all these wonderful people, but also reminded me how much I love baseball. As a graduate student, one of the worst things you can do is probably rooting for a baseball team that has a long rivalry history with your boss' team. Through those going-back-and-forth emails and conversations, I learned how to talk baseball *in the proper way*. Here, I also have to give credit to Aaron and Russ. They also helped equally with my ability of formal baseball talking. All I can say is that this was all beyond my imagination, and it was fun. So thank you all for the great experience.

In the lab, I would like to give my special thanks to three people, Peter Engels, Volker Schweikhard, and Giacomo Lamporesi. Peter was my first teacher in the lab and helped me survive through my first year. Volker told me everything I need to know to run the machine and showed me what the "German engineering" means. I had been working with Volker for almost five years, and with Volker, we had done some works that I am very proud of. Giacomo joined the lab, when I just took over the lab from Volker. Giacomo is always very patient with what I have to say about physics whether it makes sense or not. Giacomo and I had done some very interesting works. Some of those works are still very advance and very interesting. Also, thanks to Giacomo, I finally knew what the "Italian dinning" really means. In my last year at JILA, Dan and Lin joined the lab. I wish them good luck in the lab.

I would like also thank Russ, Laura, and Huanqian at the EDM labs, Juan and Rob at the ^{85}Rb lab, Jason and John at the ^{40}K lab, John and Ty in the ^{87}Rb-^{40}K mixer lab for loaning me equipments and discuss physics with me. Also, I would like to thank Dan, Matt, Phil, and Tyler for bringing my English conversation skill up to another level.

At JILA, I learned from all the best, Eric, Debbie, Jun, and many others. I learned from them how to be a successful physicist, and what it takes to be successful. Eric always has the magic to make complicated things easy to understand. Debbie always has the magic to asks the right and tough questions to make me think deeper and push myself forward. Although I didn't have a very direct connection with Jun in physics, I still learned from him by watching when lights in his office goes off. Jun has this magic to stay awake and stay enthusiastic for physics. He works so hard to make me want to work even harder. So, I thank these great teachers.

People at JILA shops is always happy to help. Here I would like to thank several people whom I often asked for help. They are Carl at electronic shop. Hans and Tom at the machine shop. J. R. at the JILA computing team. Those are the guys who makes my work at JILA much easier.

Very special thanks to Russ and Juan. They tried very hard to make this place like my second home, and I surely felt that way. In the end, I would like to give my gratitude to my lovely wife, Claire, for bringing me happiness outside the physics world.

Contents

Chapter

Chapter 1

Introduction

1.1 My work at JILA

In my early work at JILA (2003–2006), I participated in experiments studying rotating Bose-Einstein condensates (BEC). My first experiment at JILA studied the dynamics of two-component vortex lattices [4]. In this experiment, we first prepared our rotating BEC in one hyperfine state, then used a microwave pulse to transfer some of the atoms into another state. Because of interactions between two different vortex lattices, interlaced vortex lattices were observed. In the process of achieving equilibrium, the structure of each vortex lattice changed from a triangular one to a square one. This interaction-induced structural transition was studied in the experiment. In the meantime, I also helped in the experiment studying the equilibrium properties of rotating BECs [5].

In another experiment, we used a two-dimensional (2D) optical lattice to manipulate a single-component vortex lattice [2]. The optical lattice was made to co-rotate with a vortex lattice and to provide pinning forces to pin the vortices. After carefully stabilizing and aligning our experiment, we were able to make the rotating optical lattice co-rotate such that a vortex lattice saw a stationary pinning potential in its rotating frame. By using a square optical lattice to pin a triangular vortex lattice, we observed the structure of vortices changes from a triangular lattice to a square lattice. The structural transition in this experiment was caused by the pinning force provided by the optical lattice. In this

experiment, we studied the dynamics of a pinned vortex lattice and interactions between a vortex lattice and an optical lattice.

Following the pinning experiment, we changed our focus from the physics happening in the rotating frame to the physics in the stationary frame. We loaded a three-dimensional (3D) stationary BEC into a 2D trapping array that was provided by the optical lattice. By changing the height of the optical potential in each trapping site, we were able to go from the condition of $E_J \gg E_T$ to the condition of $E_J \ll E_T$, where E_J is the tunneling energy between adjacent trapping sites, and E_T is the thermal energy. In this experiment [3], we observed how the phase of the small BECs in each trapping site became random by watching how the small BECs reconnected once the optical lattice was turned off. In the case of $E_J \gg E_T$, the atoms in different condensates communicated with each other via tunneling. Therefore, they maintained their phase coherence. When $E_J \ll E_T$, the thermal fluctuations in the system were large enough to destroy phase coherence in the system. In this case, when we reconnected the small BECs, vortices resulted. In contrast to previous experiments, vortices occurred in the stationary frame. This phenomenon is related to the Berezinskii-Kosterlitz-Thouless (BKT) transition in the X-Y model [6, 7]. My work in this experiment was more than changing the mirrors and tweaking the knobs. I developed a 3D Gross-Pitaveskii equation (GPE) solver to calculate the tunneling energy between adjacent trapping sites.

In 2007–2008, Giacomo and I tried a couple of experiments. First, we tried to rotate a stationary condensate using a rotating optical lattice. We watched its rotation decaying as a function of temperature. Second, we tried to rotate a 2D condensate in a one-dimensional (1D) optical lattice. In this experiment, we successfully rotated a BEC, observed tens of vortices, and kept a similar number of vortices in the optical lattice "more than 10 seconds." In the end, we didn't submit the work for publication. We decided to switch the focus of the experiment to studying the BKT transition in a continuous system.

For the work described in the main body of this thesis, we used a similar setup to the Paris group [8, 9] to create many isolated 2D systems. We then used a microwave-pumping scheme to image *in-situ* one layer (or one 2D system) in the trap. We then compared the measured result with the one predicted from the semiclassical Hartree-Fock mean-field model. This model is similar to the one reported in [10]. The amazing thing about the semiclassical Hartree-Fock mean-field model is that there is really nothing amazing about it. This model discards all the interaction-related magic such as phonons and vortices. As much as one needs the phonons and vortices to account for BKT physics, which are beyond the mean-field description, we were able to identify the onset of a deviation in our measurement from the semiclassical Hartree-Fock mean-field model.

We also used a complementary imaging technique known as the focusing-imaging method [11, 12] to measure the momentum distribution of the system more accurately than previous measurements [13, 14]. From the momentum distribution of the system, we observed the onset of a long spatial extent of coherence in the system. By comparing both the *in-situ* and focusing-imaging methods, we were able to identify rather accurately a very interesting regime that was beyond the mean-field description, but not quite yet a quasicondensate. Using our data, we also tested the critical phase-space density proposed in [15].

1.2 This thesis

The organization of my thesis is as follows: In chapter 2, I give some "simple" 2D physics that might help readers understand our work in this experiment. Also, I give a short review of previous experiments that studied the BKT transition in a continuous system. In Chapter 3, I give some details of our experimental setup for creating a 2D system and controlling its temperature. I also discuss a couple of imaging artifacts that influence the measurements. In the end of the chapter, I discuss two different imaging methods used for measuring the coordinate-space and momentum-space density distributions. Chapter 4

gives the model and the method we used to identify a very interesting regime that is beyond mean-field description. I will detail the development of the model we call the semiclassical, mean-field, local-density approximations. This model is used to compare with coordinate-space images. A couple interesting features of the model are also shown in this chapter. In Chapter 5, I show the identification of the BKT temperature T_{BKT}, below which the system possesses a coherent fraction. The measurement of the coherent fraction is also presented in this chapter. In Chapter 6, I summarize our experiment on exploring the interesting physics around the BKT transition. Next, I present my personal outlook on the studies of 2D ultracold-atom systems. Appendix A is a *Physical Review Letter* [2] I wrote on the interactions between rotating optical lattices and vortex lattices. Appendix B is also a *Physical Review Letter* [3] I co-authored on some precursor experiments to the work of this thesis. There, we looked at the BKT transition in a superfluid on a 2D lattice. More details about this experiment can be found in Ref. [16]. I am proud of both of these papers, but they are so far removed from the topic of a 2D Bose gas in a continuous system, that I chose not to include a discussion of these earlier works in the main body of my thesis.

Chapter 2

Interacting bosons in two dimensions

2.1 Introduction

It is known that the statistical behavior of systems can be very different in lower dimensions from it is in three dimensions (3D). In 3D, many-body systems can possess a long-range order (LRO) or undergo Bose-Einstein condensation. Take a Bose gas in 3D for example. The system can undergo Bose-Einstein condensation at a critical temperature. For this system at the critical temperature or lower, the atomic populations in excited states are saturated, and atoms begin to accumulate in the ground state of the system, as shown in Fig.2.1. For a 3D homogeneous system, the Bose-Einstein condensation happens when the phase-space density of the system reaches 2.612 [17]. For weakly interacting atoms in a 3D homogenous system, the BEC transition still exists.

For a two-dimensional (2D) system, things change dramatically. In a 2D crystal, a long-range order does not exist, as was pointed out by Peierls [18]. In a 2D crystal at a finite temperature, the uncertainty in the relative position of two atoms is given by

$$\langle(\vec{u}(\vec{r}) - \vec{u}(0))^2\rangle \propto T \ln\left(\frac{r}{a}\right), \tag{2.1}$$

where $\vec{u}(\vec{r})$ is the displacement vector of an atom from its equilibrium position at $\vec{r}$, and a is the lattice constant of the 2D crystal. Equation (2.1) diverges as the separation between two atoms goes to infinity. This fact tells us that at any finite temperature, one cannot *predict*

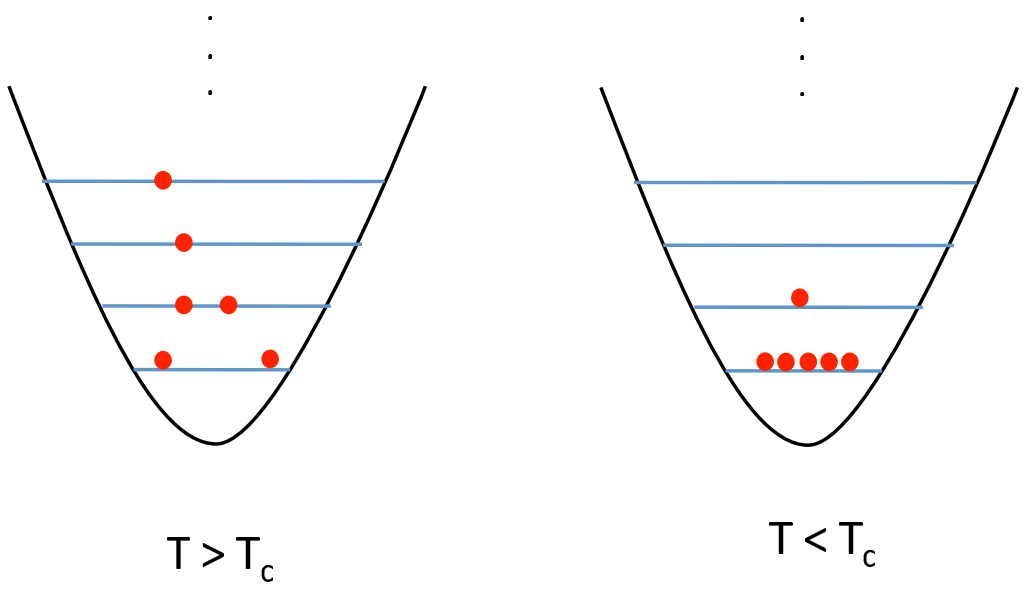

Figure 2.1: At a temperature $T > T_c$, atoms have a very small probability to populate any state of the harmonic trap. However, at $T < T_c$, atoms begin to accumulate in the ground state of the system. This phenomenon is known as Bose-Einstein condensation.

the position of an atom far away by knowing the position of another atom at the origin of the coordinate. In contrast, in a 3D crystal, the uncertainty of the displacement of two atoms is smaller than the lattice constant a as long as the temperature of the system is smaller than the melting temperature. After Peierls' finding, Mermin and Wagner [19] and Hohenberg [20] proved that the lack of long-range order (LRO) [21] at a nonzero temperature in a 2D crystal is also true for other systems in lower dimensions.

For an interacting Bose gas in 2D, the above statement says there is no Bose-Einstein condensation at any finite temperature. In a system with weakly interacting bosons, the dispersion of excitations of the system at small momentum is linear instead of quadratic [17, 22]. The linear part of the dispersion is usually referred to as phonons. The existence of the low energy phonons causes phase fluctuations at finite temperatures. In a lower dimensional system, the enhanced phase fluctuations can destroy the LRO or the condensate. The absence of the BEC in a 2D system can be seen by examining the decay of its first-order correlation functions.

2.2 First-order correlation function

The absence of Bose-Einstein condensation can be equivalently written, using first-order correlation functions, as

$$\lim_{|\vec{r}-\vec{r}'|\to\infty} G^{(1)}(\vec{r},\vec{r}') = 0, \tag{2.2}$$

where $G^{(1)}(\vec{r},\vec{r}')$ is the first-order correlation function defined as [23]

$$G^{(1)}(\vec{r},\vec{r}') \equiv \langle \hat{\Psi}^\dagger(\vec{r})\hat{\Psi}(\vec{r}')\rangle, \tag{2.3}$$

where $\hat{\Psi}^\dagger(r)$ and $\hat{\Psi}(r)$ are, respectively, the creation and annihilation field operators that create or annihilate a particle at position r. In the case of $\vec{r}' = \vec{r}$,

$$\begin{aligned} G^{(1)}(\vec{r},\vec{r}) &= \langle \hat{\Psi}^\dagger(\vec{r})\hat{\Psi}(\vec{r})\rangle \\ &= n(\vec{r}). \end{aligned} \tag{2.4}$$

$G^{(1)}(\vec{r},\vec{r})$ is also known as the one-body density matrix, which gives the density distribution $n(\vec{r})$ in the coordinate space.

In an infinite homogeneous system, an important relation exists between the momentum distribution of the system and the first-order correlation function. The momentum distribution of the system can be expressed as

$$n(\vec{p}) = \langle \hat{\Psi}^\dagger(\vec{p})\hat{\Psi}(\vec{p})\rangle, \tag{2.5}$$

where $\hat{\Psi}^\dagger(\vec{p})$ and $\hat{\Psi}(\vec{p})$ are, respectively, the creation and annihilation operators in momentum space. These operators are

$$\hat{\Psi}(\vec{p}) = \frac{1}{2\pi\hbar}\int d\vec{r} e^{-i\vec{p}\cdot\vec{r}/\hbar}\hat{\Psi}(\vec{r}), \tag{2.6}$$

$$\hat{\Psi}^\dagger(\vec{p}) = \frac{1}{2\pi\hbar}\int d\vec{r} e^{i\vec{p}\cdot\vec{r}/\hbar}\hat{\Psi}^\dagger(\vec{r}). \tag{2.7}$$

Putting Eqs. (2.6) and (2.7) into Eq. (2.5), one finds that

$$n(\vec{p}) = \frac{A}{(2\pi\hbar)^2}\int d\vec{s} G^{(1)}(s) e^{i\vec{p}\cdot\vec{s}/\hbar}, \tag{2.8}$$

where $\vec{s} = \vec{r} - \vec{r}'$, A is the area of the 2D system, and $G^{(1)}(s) = G^{(1)}(|\vec{s}|)$. As one can see from Eq. (2.8), the momentum distribution is the inverse Fourier transform of the first-order correlation function. In other words, the first-order correlation function is the Fourier transform of the momentum distribution, i.e.,

$$G^{(1)}(\vec{s}) = \frac{1}{A}\int d^2p\, n(\vec{p}) e^{-i\vec{p}\cdot\vec{s}/\hbar}. \tag{2.9}$$

In the presence of a BEC, the momentum distribution would have a singularity at $\vec{p} = 0$, and

$$n(p) = N_0\delta(\vec{p} = 0) + n_T(\vec{p} \neq 0), \tag{2.10}$$

where n_T is a smooth function of $\vec{p}$. One can see, after plugging Eq. (2.10) into Eq. (2.9), the first-order correlation function approaches a constant value of N_0/A, which is the condensate

density, as $s \to \infty$. In contrast, in the absence of the condensate, the first-order correlation function goes to zero when $s \to \infty$. As mentioned earlier, in 2D, there is no condensate at any finite temperature. Therefore, one would expect the correlation function to approach zero at infinity for any 2D system with continuous symmetry.

2.2.1 The ideal Bose gas

How $G^{(1)}(s)$ decays depends on the behavior of n_T. For a highly nondegenerate ideal Bose gas in a 2D box, the distribution is well described by the Boltzmann distribution,

$$n_k = e^{-(\frac{\hbar^2 k^2}{2m} - \mu)/k_b T}, \tag{2.11}$$

where the chemical potential is determined by

$$\begin{aligned} N &= \frac{L^2}{(2\pi)^2} \int_0^\infty dk\, 2\pi k e^{-(\frac{\hbar^2 k^2}{2m} - \mu)/k_b T} \\ &= \frac{L^2}{\lambda_{db}^2} e^{\mu/k_b T}, \end{aligned} \tag{2.12}$$

where λ_{db} is the de-Broglie wavelength, L^2 is the area of the 2D box, and N is the total number of atoms. Using Eqs.(2.9), (2.11), and (2.12), one finds that in the high-temperature regime, the first-order correlation function can be written as

$$G^{(1)}(s) = n e^{-\pi(\frac{s}{\lambda_{db}})^2}. \tag{2.13}$$

In this regime, $n\lambda_{db}^2 \ll 1$, and $G^{(1)}(r)$ is a Gaussian with a width of $\lambda_{db}/\sqrt{2\pi}$.

In the regime close to degeneracy, where $n\lambda_{db}^2 \sim O(1)$, only the states with $\frac{\hbar^2 k^2}{2m} \ll k_b T$ are strongly occupied. In this case, the number of atoms in state k is given by

$$n_k = \frac{kT}{\frac{\hbar^2 k^2}{2m} - \mu}. \tag{2.14}$$

Using Eqs. (2.9) and (2.14), one can get

$$G^{(1)}(s) = \frac{2}{\lambda_{db}^2} K_0(r/l_c), \tag{2.15}$$

where K_0 is the zero order of the modified Bessel function of the second kind [24], and $l_c = \lambda_{db} e^{n\lambda_{db}^2/2}/\sqrt{4\pi}$. The asymptotic behavior (at large r) of K_0 can be found as $e^{-r/l_c}/\sqrt{r/l_c}$. As one can see from Eqs. (2.13) and (2.15), the correlation functions for 2D ideal Bose gases eventually decay to zero at $r \to \infty$. In a system close to degeneracy, the spatial extent of coherence l_c can still be very long and increases exponentially according to its phase-space density i.e. $l_c \propto e^{n\lambda_{db}^2/2}$. Interestingly, in the 1D case, the spatial extent of coherence in this regime increases only linearly according to $n\lambda_{db}^2$ [25].

2.2.2 The weakly interacting Bose gas

Let's consider the first-order correlation function for an interacting 2D Bose gas. At high temperature, when $n\lambda_{db}^2 \ll 1$, the interactions have little effect. Therefore, one expects a very similar result with ideal-gas model. In the low temperature regime, Petrov *et al.* [26, 27] found a similar result for the spatial extent of coherence for weakly interacting bosons in a harmonically trapped system. They used a method developed for 3D-trapped condensates to calculate the excitation spectrum of the system. Then, using the excitation spectrum to calculate the mean-square fluctuations of the phase, they found that at temperatures below the critical temperature, the characteristic radius of the phase fluctuation was

$$R_\phi \approx \lambda_{db} e^{\frac{n\lambda_{db}^2}{2}}, \tag{2.16}$$

where n is the density of the system. From the exponentially increasing spatial extent of coherence, one expects a slow decay in the first-order correlation function.

Calculating the first-order correlation function for a weakly interacting Bose gas requires some serious mathematics. However, at low temperature $T \ll T_{BKT}$, the calculation can be simplified by a series of approximations. The approach I adopted here is a 2D version of the 1D derivation in [25]. A similar 2D derivation can be also found in [28]. First, in the

framework of the second quantization, the Hamiltonian of the system can be written as

$$\hat{H} = \int dr\ \hat{\Psi}^\dagger \frac{-\hbar^2}{2m}\nabla^2\hat{\Psi} + \frac{U_0}{2}\int dr\ \hat{\Psi}^\dagger\hat{\Psi}^\dagger\hat{\Psi}\hat{\Psi}, \tag{2.17}$$

where U_0 is the interaction strength. Here, a contact interaction is adopted. If the fluctuation of the field is small, one can write the field operator as

$$\hat{\Psi}(\vec{r}) = \sqrt{n + \delta n(\vec{r})}\, e^{i\theta(\vec{r})}, \tag{2.18}$$

where n is the the mean density, δn is the density fluctuation operator, and θ is the local phase operator. The density and the phase operator obey the commutation relation

$$[\delta n(\vec{r}), \theta(\vec{r}')] = -i\delta(\vec{r} - \vec{r}'). \tag{2.19}$$

Plugging Eq. (2.18) into Eq. (2.17), one can find a new quadratic Hamiltonian $\hat{H}'$ in terms of the operator θ and δn,

$$\hat{H}' = \frac{\hbar^2 n}{2m}\int (\nabla\theta(\vec{r}))^2\, d^2r + \int \left[\frac{\hbar^2 n}{2m}(\frac{\nabla\delta n(\vec{r})}{2})^2 + 2U_0 n^2(\frac{\delta n(\vec{r})}{2})^2\right] d^2r. \tag{2.20}$$

Next, by expanding the two operators in sinusoidal modes, one gets

$$\theta = \sum_{\vec{k}>0} \sqrt{2}\left(\theta_{c,k}\cos(\vec{k}\cdot\vec{r}) + \theta_{s,k}\sin(\vec{k}\cdot\vec{r})\right), \tag{2.21}$$

$$\delta n = \sum_{\vec{k}>0} \sqrt{2}\left(\delta n_{c,k}\cos(\vec{k}\cdot\vec{r}) + \delta n_{s,k}\sin(\vec{k}\cdot\vec{r})\right), \tag{2.22}$$

where $\vec{k} = \frac{2\pi}{L^2}(n_x\hat{x} + n_y\hat{y})$, which are the eigenmodes of a 2D box with a size of L^2. Plugging Eqs.(2.21) and (2.22) into Eq. (2.20), one can find for each wave vector k the corresponding Hamiltonian is given by

$$\hat{H}_k = L^2\left(\frac{U_0}{2}\left(\delta n_{c,k}^2 + \delta n_{s,k}^2\right) + \frac{n\hbar^2k^2}{2m}\left(\theta_{c,k}^2 + \theta_{s,k}^2\right)\right). \tag{2.23}$$

At a sufficiently low temperature, the contribution to $\hat{H}_k$ from the density fluctuation $\delta n/n$ is much smaller than the contribution from the phase modulation θ. In this case, one can, to a

good approximation, keep only the phase modulation term in Eq. (2.23). If the temperature is still much larger than $U_0 n$, only the excitation and a smaller wave vector k are relevant, and classical statistics apply. Thus, for every quadratic degree of freedom the energy is $k_b T/2$, and one finds that

$$\langle \theta_{c,k}^2 \rangle = \langle \theta_{c,k}^2 \rangle = \frac{1}{n\lambda_{db}^2} \frac{\pi}{k^2 L^2}. \tag{2.24}$$

Since the density fluctuation is neglected, the first-order correlation Eq.(2.3) can be written as

$$\begin{aligned} G^{(1)}(r) &= n\langle e^{-i(\theta(\vec{r})-\theta(0))} \rangle \\ &= e^{-\langle (\theta(\vec{r})-\theta(0))^2 \rangle/2}. \end{aligned} \tag{2.25}$$

The second equality holds because of the assumption of a Gaussian fluctuation in the phase fluctuation. The phase fluctuation is given by

$$\langle (\theta(\vec{r}) - \theta(0))^2 \rangle = \sum_{k>0} 2\langle \theta_{c,k}^2 \rangle \left(\cos(\vec{k} \cdot \vec{r}) - 1 \right)^2 + \sum_{k>0} 2\langle \theta_{c,k}^2 \rangle \sin(\vec{k} \cdot \vec{r})^2. \tag{2.26}$$

Using Eq. (2.24), one obtains

$$\langle (\theta(\vec{r}) - \theta(0))^2 \rangle = 4(\frac{1}{n\lambda_{db}^2} \frac{\pi}{k^2 L^2}) \sum_{k>0} \frac{1 - \cos(\vec{k} \cdot \vec{r})}{k^2}. \tag{2.27}$$

Taking $L \to \infty$, one can replace $\sum$ with $(\frac{L}{2\pi})^2 \int d^2k$. Then, one finds

$$\begin{aligned} G^{(1)}(r) &= n e^{\frac{-1}{2\pi n \lambda_{db}^2} \int_0^{1/\xi} \frac{1-\cos(\vec{k}\cdot\vec{r})}{k^2} d^k} \\ &= n \left(\frac{\xi}{r} \right)^{1/n\lambda_{db}^2}, \end{aligned} \tag{2.28}$$

where $1/\xi$ is the cutoff wave vector. Therefore, at a temperature of $T \ll T_{BKT}$, one expects an algebraic decay in the first-order correlation function. At infinity, the spatial extent of coherence will eventually go to zero. However, for a finite system, the phase fluctuation can still be very small. This algebraic decay of the coherence is the definition of a *quasi-condensate*. This power-law decay of the first-order correlation function at large r is first

obtained by Kane and Kadanoff [29]. Although there are other different definitions for a quasicondensate in recent literatures, I use the original definition throughout my thesis to avoid confusion. Regarding the regime that is beyond mean-field behavior and lacks a long spatial extent of coherence, we call it "a very interesting regime."

2.3 Berezinskii-Kosterlitz-Thouless (BKT) transition

In a 2D system, the long-wavelength excitations from phonons are strong enough to destroy the condensate or LRO, but not strong enough to completely suppress the superfluid. As was first pointed out by Kane and Kadanoff [29] and then proved by Berezinskii [6], there exists a normal-to-superfluid phase transition at the critical temperature T_{BKT}. Later, Kosterlitz and Thouless [7] found that this phase transition is related to the unbinding of the vortex-antivortex pairs that exist in a 2D system at a finite temperature, as shown in Fig. 2.2. At a temperature lower than T_{BKT}, the 2D system is a superfluid, but it doesn't possess a long-range order. This *noncondensate superfluid* is called a quasicondensate.

The critical temperature of the BKT transition can be estimated as follows. Consider the energy of a free vortex E_v that appears in an infinite homogeneous 2D system. The vortex considered here is a quantum object that appears in a superfluid. The atomic density at the center of the vortex is zero, and the phase winding around the vortex is 2π. The antivortex has the same properties, but has a phase winding of -2π. The velocity of the superfluid is

$$\vec{v}_s = \frac{\hbar}{m}\vec{\nabla} f(\vec{r}), \tag{2.29}$$

where $f(\vec{r})$ is the function representing the phase variation in a super system. Therefore, the superfluid velocity around a vortex can be found to be

$$\vec{v}_s = \frac{\hbar}{mr}\hat{\theta}, \tag{2.30}$$

where r is the distance from the center of the vortex. The energy of the vortex can be written

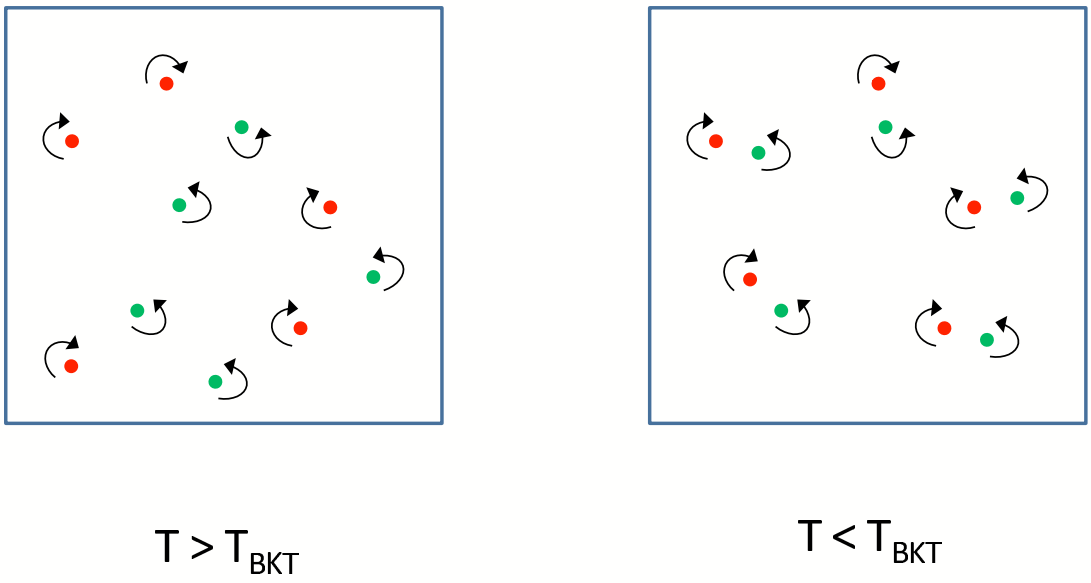

Figure 2.2: A 2D system cannot have a long-range order or condensate, but it can still undergo a BKT transition that is a normal-to-superfluid transition. At $T > T_{BKT}$, the thermal fluctuation can proliferate free vortices or free antivortices in the atomic cloud. Those vortices destroy the phase coherence of the system. However, at $T < T_{BKT}$, vortex and antivortex are bound. In this regime, the coherence of the system decays according to a power law. The phase is often referred to as quasicondensate.

as

$$E_v = \int_{\xi}^{R} \frac{1}{2} n_s \left(\frac{\hbar}{mr}\right)^2 d^2r, \tag{2.31}$$

where R is the size of the system, and ξ is the healing length of the vortex. Creating a free vortex increases the entropy of the system as

$$S_v = \ln \frac{R^2}{\xi^2}. \tag{2.32}$$

Consider the free energy $F = E_v - TS_v$, i.e.,

$$F = k_b T(n_s \lambda_{db}^2 - 4) \ln \frac{R^2}{\xi^2}. \tag{2.33}$$

One can see that the proliferation of free vortices would become energetically favorable if the phase-space density was smaller than 4. One can also convert this critical phase-space density to the critical temperature T_{BKT}. Then, one gets

$$T_{BKT} = \frac{\pi \hbar^2 n_s}{2m k_b T}. \tag{2.34}$$

When the temperature of the 2D system is lower than T_{BKT}, the system is in a superfluid phase, and the vortex-antivortex pairs are bound. However, when the temperature of the system is warmed up to T_{BKT}, the vortex-antivortex pairs become unbound, and free vortices proliferate. Then, the phase of the system becomes normal.

2.4 Experiments on 2D ultracold bosonic atoms

The first effort to create a 2D ultracold atom system was that of Ref. [30]. Next, a series of papers from the Paris group [8, 9, 13, 31, 32] focused on the fluctuating regime in a 2D ultracold atom system. The Paris group observed the phase fluctuations of a 2D Bose gas. First, the group loaded a 3D cloud into a 1D optical lattice. The lattice sliced the 3D cloud into many 2D layers. Second, the researchers used microwave pumping to get rid of all but two central layers for interfering. From the interference pattern they obtained, they

extracted information about correlations in the 2D layers according to the method proposed in [33]. The exponent that described the coherence changed from 0.5 to 0.25, which was expected as the system passed the BKT transition. The researchers saw dislocations (or defects) show up in the interference pattern. They also found that the probability of seeing dislocations had a temperature dependence. Both experimental results encouraged them to relate their observations to the BKT physics. Their observations also successfully generated much interest in theoretical studying the fluctuating regime in a 2D ultracold atom system.

In a later paper [13], the same group identified the BKT transition with an observation of bimodality (a Gaussian + an inverse parabola) in a time-of-flight (TOF) image. Right before the observation of the bimodal distribution, the researchers measured the critical number by integrating the measured optical depth over the whole TOF image. Comparing their measurements to the predictions of the ideal gas model, they saw a substantial deviation that was, however, very different from what was expected in a 3D system.

In this paper [13], the researchers identified the BKT transition with the observation of a bimodal distribution. However, the appearance of bimodality strongly depended on the two models chosen for fittings. It is not clear to me that the two models, a Gaussian and a inverse parabola, are accurate enough to describe a 2D cloud at BKT temperature. Also, since the ideal and mean-field models lack of the magic of phonons and vortices, using either one to describe a system close to the BKT transition is, in principle, wrong. However, in a trapped system, the area of the fluctuating regime is small compared to the size of the system. Therefore, a global parameter like the critical number is not very different for a mean-field model or for a beyond mean-field model.

In another experiment [14], the Gaithersburg group loaded sodium atoms into a light sheet that created a single-layer 2D system. After releasing the atoms from the trap, a three-component (superfluid quasicondensate, non-superfluid quasicondensate, and normal phase) density distribution was observed. The “non-superfluid quasicondensate” used in

the Gaithersburg group's paper represented the regime where the density fluctuation of the system was suppressed, but without a long coherence length. Considering that an ideal Bose-gas model would also predict a three-component like distribution, a description of a three-component distribution was just not very accurate for describing the lower-dimension gas.

Chapter 3

Experimental details

3.1 Optical lattice

Optical potentials provide a variety of opportunities for studying ultracold atoms. Laser beams can interfere with each other and create a rich variety of interference patterns. Even before the creation of the Bose-Einstein condensate (BEC), scientists used this amazing tool to study cold atoms in optical lattices. In the post-BEC era, superfluids in periodical potentials have been the focus of studies involving ultracold atoms. Greiner *et. al.* [34] loaded a condensate into a 3D optical lattice and transferred the system from a superfluid state into a Mott state. This work has triggered a new generation of experiments with the possibility of realizing a quantum computer in an ultracold atom system. Also, the ease of creating a high spatial frequency in an optical potential is conducive to creating lower-dimensional systems.

An atom interacts with a light field via an induced-dipole moment. Considering the atom and light as a classical driven, damped oscillator, one can derive the interaction energy and the scattering rate, respectively, as [35]

$$U_{int} = \frac{3\pi c^2}{2\omega_0^3}\frac{\Gamma}{\Delta}I, \tag{3.1}$$

$$\Gamma_{sc} = \frac{3\pi c^2}{2\hbar\omega_0^3}\left(\frac{\Gamma}{\Delta}\right)^2 I, \tag{3.2}$$

where c is the speed of light, ω_0 is the natural frequency of the classical atomic oscillator,

Δ is the detuning of the driven frequency to the natural frequency ω_0, Γ is the on-resonant damping rate, and I is the field intensity. Equation (3.1) and (3.2) give a good approximation to a real atom if $\Gamma \ll \Delta$, and there is no saturation effect.

A couple things can be easily seen from Eqs. (3.1) and .(3.2). First, if the light is red detuned ($\Delta < 0$), the shift of the interaction energy is negative. If there exists a spatial dependence in the field, atoms would be pushed towards the field maximum (the nodes of the optical lattice). If the light is blue detuned ($\Delta > 0$), atoms would be pushed towards the field minimum (the antinodes of the optical lattice). Second, the interaction energy scales as (I/Δ), whereas the photon scattering rate scales as I/Δ^2. Therefore, using a large detuning and a large intensity can keep the photon-scattering rate low while providing a large enough potential depth for trapping.

For a two-beam interference pattern, the field intensity can be written as

$$I(z) = I_0 \cos^2\left(\frac{\pi}{d} z\right), \tag{3.3}$$

where I_0 is the maximum intensity, and d is the period of spatial modulation determined by

$$d = \frac{\lambda}{2\sin\left(\frac{\theta}{2}\right)}, \tag{3.4}$$

where θ is the angle between the two interfering beams, and λ is the wavelength of the laser. If the interfering beams are elliptical Gaussian beams with waists of σ_x and σ_z and a power P, the maximum intensity I_0 is given by $2P/\pi\sigma_x\sigma_z$. When an atom placed in such a field, the interference pattern will create an array of trapping sites. This array of trapping sites is called a 1D optical lattice. For a single trapping site, the trapping frequency can be approximated as

$$\omega_z = \sqrt{\frac{\alpha}{\Delta}\left(\frac{2P}{\pi\sigma_x\sigma_z}\right)}\,\frac{\pi}{d}, \tag{3.5}$$

where $\alpha = 3\pi c^2\Gamma/m_{Rb}\omega_0^3$.

In our experiments, the wavelength for the interfering laser is 532 nm. The angle between the two interfering beams is 8°, which gives a lattice constant of 3.8 μm. The

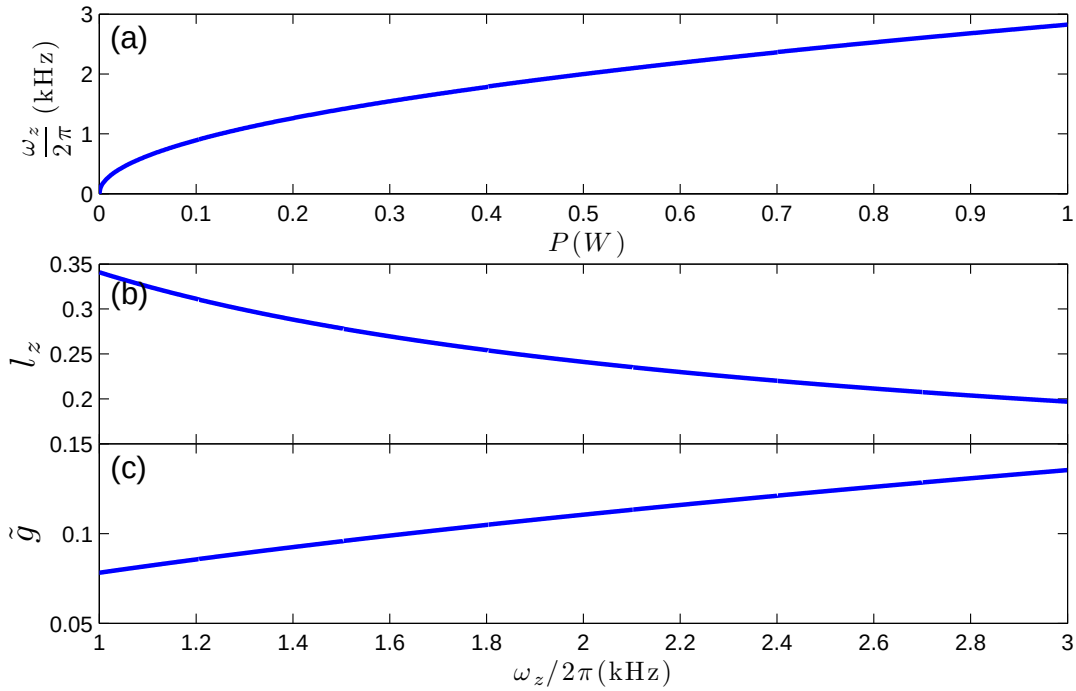

Figure 3.1: (a) Trapping frequency for a ^{87}Rb atom at the bottom of a single trapping site in the 1D optical lattice as a function of the optical power per interfering beam. (b) size of the 2D Bose gas in the lattice direction as a function of trapping frequency (c) The dimensionless 2D interaction strength $\tilde{g}$ as a function of trapping frequency.

waist of the interfering beams, σ_x and σ_z, is 225 μm and 84 μm, respectively. Figure 3.1(a) shows the relation between the input power and the trapping frequency at the bottom of a single trapping site. We measure the power of a single beam to be 300 mW. Using the model above, one gets a trapping frequency of 1.55 kHz, which is in fine agreement with the measured-trapping frequency of 1.4 kHz. Figure 3.1(b) gives the size, l_z, of the 2D Bose gas in the tight confinement ($\hat{z}$) direction. Figure 3.1(c) gives the dimensionless 2D interaction strength, $\tilde{g} \equiv \sqrt{8\pi}(a_s/l_z)$, where a_s is the 3D scattering length of the atom, and $\tilde{g} = 0.09$ in our experiments, which compares to $\tilde{g} = 0.13$ [9, 13] and 0.146 [32] in the Paris group and $\tilde{g} = 0.02$ in the Gaithersburg group [14]. As one can see from Fig. 3.1(c), $\tilde{g}$ has a very weak dependence on the power of the interfering beams. To reach $\tilde{g} = 1$, which is the value for a strongly interacting system like a ^{4}He film, one has to increase the power by a hundredfold. Another way to increase $\tilde{g}$ is to reduce the lattice constant, d. As the lattice constant becomes smaller and smaller, one has to worry about atoms tunneling between different layers, however.

The experimental setup is shown in Fig. 3.2. The laser light is provided by a Verdi V10, which has a wavelength of 532 nm. The light passes through an acousto-optic modulator (AOM), which is used to control and stabilize the intensity of the beam. The intensity-stabilizing module is made of a microwave source, a microwave amplifier, a mixer, and a feedback circuit that was designed by the JILA shop. After the AOM, the light is guided through a single-mode polarization-maintaining (PM) fiber. When the lattice is not in use, we keep the lattice continuously on at its close-to-maximum value such that the fiber and the AOM can thermally equilibrate at their operating temperature. The light is blocked by a mechanical shutter after the fiber. Before the shutter is open, the intensity of the optical lattice is abruptly turned off by the intensity-stabilizing module. After the shutter is opened, the optical lattice is gradually ramped up to the desired value in one second. The two interfering beams are focused onto the atomic cloud by a cylindrical lens. The

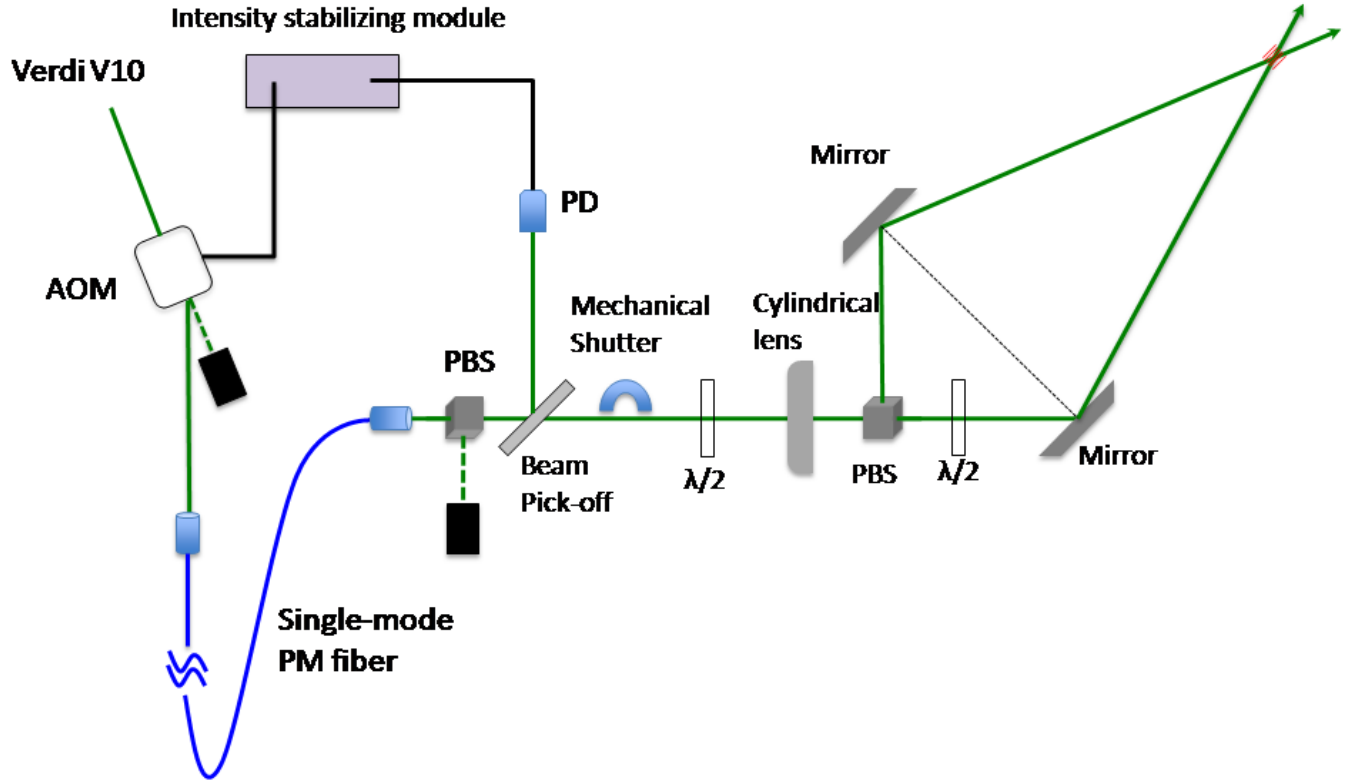

Figure 3.2: Experimental setup for the 1D optical lattice. The total power we injected into the fiber was ∼1.8 W. The power output from the fiber was ∼0.8 W. The laser light first passed through a polarizing beam-splitting (PBS) cube to select a single polarization. A few percent of the laser light was split out by a pick-off window and sent to the intensity-stabilizing module. After the laser beam was split into two interfering beams by the second PBS, they passed two mirrors (indicated by the dashed line) that was mounted on the same post to increase rejection off common vibration modes.

resulting waists of the beams are 225 μm (long axis) and 84 μm (short axis). The laser light is separated into two beams by a polarizing beam-splitting (PBS) cube. The power of the two beams is carefully balanced by rotating the $\lambda/2$ plate in front of the PBS. The $\lambda/2$ plate after the PBS cube rotates the polarization back for maximal interference. The two mirrors on the two arms of the interferometer are mounted to the same post to increase the rejection off common vibration modes.

3.2 Time-averaged orbiting magnetic trap

In our experiments, the optical lattice is blue-detuned. Atoms are trapped in the nodes of the lattice, which are intensity minima. The optical lattice only provides confinement in the z (or gravity) direction. The radial confinement comes from a time-averaged orbiting magnetic trap, a so-called TOP trap [36]. The TOP trap was used for the creation of the first BEC in 1995 [37]. It is made of an anti-Helmholtz coil (quadrupole field) along the z-axis and a pair of Helmholtz coils (bias field) along the x- and y- axes. The bias field generated by the Helmholtz coils can be made to rotate according to

$$B_b = B_{0x}cos(\omega_T t)\hat{x} + B_{0y}sin(\omega_T t + \phi)\hat{y}. \tag{3.6}$$

The rotating bias field shifts the center of the quadrupole trap generated by the anti-Helmholtz coil in a circular trajectory. To be able to confine atoms in the trap, the condition

$$\omega \ll \omega_T \ll \omega_L \tag{3.7}$$

must be met [38]. Here ω is the trap frequency, and ω_L is the Larmor frequency splitting between the spin states of an atom in a magnetic field. One of the advantages of the TOP trap is its ability to become very round. By changing the value of B_{0x}/B_{0y} and ϕ separately, we are able to minimize the difference of the trapping frequencies in two independent axes in the horizontal plane to within 3%. A 3% is far from the record roundness achieved in this

lab [39]. However, it is good enough for the current experiment. Using a transverse round trap allows us to easily take an azimuthal average of our data to minimize statistical noise.

Because of gravity, the position of the cloud often sags from the trap center. The trapping potential under the influence of gravity can be written as

$$U(x,y,z) = \frac{1}{T}\int_0^T \mu \left| B_{TOP}(\vec{x},y,z,t) \right| dt + mgz, \tag{3.8}$$

where μ is the Zeeman-dependent magnetic moment of an atom, m is the mass of an atom, g is the gravitational acceleration, T is the oscillating period of the bias field $\vec{B}_b$, and

$$\vec{B}_{TOP} = \sqrt{(\frac{B'_z}{2}x + B_0 cos(\omega_T t))^2 + (\frac{B'_z}{2}x + B_0 sin(\omega_T t))^2 + (B'_z z)^2}. \tag{3.9}$$

The equilibrium position can be found by solving

$$\frac{\partial U(0,0,z)}{\partial z} = 0, \tag{3.10}$$

which gives

$$z_{min} = \frac{-(B_0/B'_z)}{\sqrt{(\frac{\mu B'_z}{mg})^2 - 1}}. \tag{3.11}$$

If the bias field is suddenly ($1/\omega \gg t \gg 1/\omega_L$) turned off, the magnetic field around the equilibrium position, (0, 0, z_{min}), can be expressed as

$$|B(x,y,z)| = \sqrt{(B'_z z_{min} + B'_z(z - z_{min}))^2 + (\frac{B'_z}{2}x)^2 + (\frac{B'_z}{2}y)^2}. \tag{3.12}$$

If z_{min} is large enough such that $B'_z z_{min} \gg (B'_z/2)\delta R$, where δR is the extent of the atomic sample, the field can be approximated as

$$\vec{B}(x,y,z) \approx (B'_z z_{min} + B'_z(z - z_{min}))\hat{z}. \tag{3.13}$$

In the experiment, an extra bias field of 24 G is added along the the z direction to further reduce the magnetic-field curvature in the x and y directions. This magnetic gradient is used, in conjunction with a microwave pumping pulse, for selecting a single atomic layer for imaging.

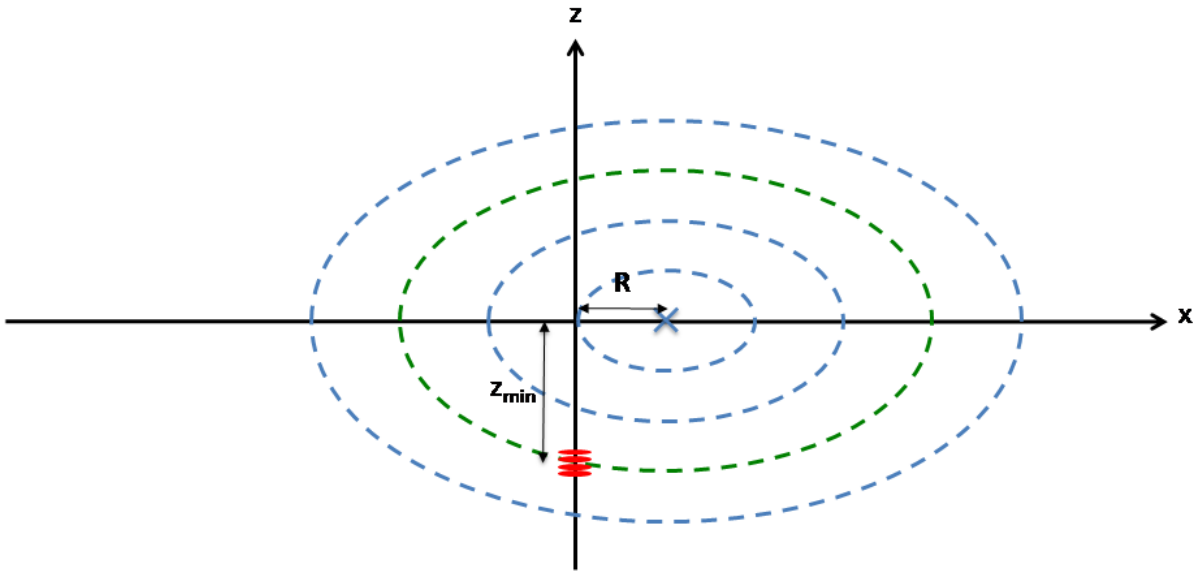

Figure 3.3: Instantaneous X-Z cross-section of the TOP trap. The contours represent the same magnitude of the magnetic field at a particular time. The blue cross indicates the center of the quadrupole trap, and the red blobs indicate atoms loaded into a 1D optical lattice. The circle in the x-y plane with radius R is called the "circle of death." Atoms can escape from here after a Majorana spin flip. Because of the gravity sag, the equilibrium position is offset by z_{min} from the center of the TOP trap. With the current experimental setup, z_{min} is larger than the size of the cloud. Therefore, the only atom-ejection mechanism comes from the RF knife.

Since the radial confinement only comes from the TOP fields, it is possible to implement rf evaporative cooling in the system. Evaporative cooling provides an easy and accurate handle for manipulating the temperature of the system. The working principle of evaporative cooling is selectively forcing hotter atoms in the atomic distribution away from the trap, which lower the temperature of the system after thermal equilibration. This selective removal comes from two mechanisms in a TOP trap. First, the applied radio-frequency field (RF knife) pumps atoms with higher energy from a trappable state to an untrappable state at the edge of the cloud. Second, atoms with higher energy can move to the center of the rotating magnetic-quadrupole field where atoms can undergo a Majorana spin flip and escape from the trap. Both mechanisms help in the early stage of the evaporative process. In the final stage of evaporation, only the selective removal from the RF knife is relevant, as shown in Fig.3.3. The temperature of the central layer vs frequency of the RF knife is plotted in Fig. 3.4.

3.3 Imaging

Our detection of atoms is the absorption-imaging method. The advantage of absorption imaging is that it is easy to set up compared to other imaging methods. One locks the probing light to one of the atomic transitions and shines the light onto the atoms. The photons in the probing beam will be scattered by the atoms and cast a shadow on the probing beam. This shadow is then imaged onto a CCD camera. Two separate images are often taken during the imaging process, one with atoms and the other without atoms. A quantity called optical depth (OD) is often extracted after an imaging sequence. If the atomic transition is a cycling transition, a single atom can scatter many photons, which helps increase the signal-to-noise ratio (SNR) of the images. Assume that the probing beam is fired for a long enough time, such that the photon scattering process reaches a steady state and can be faithfully described

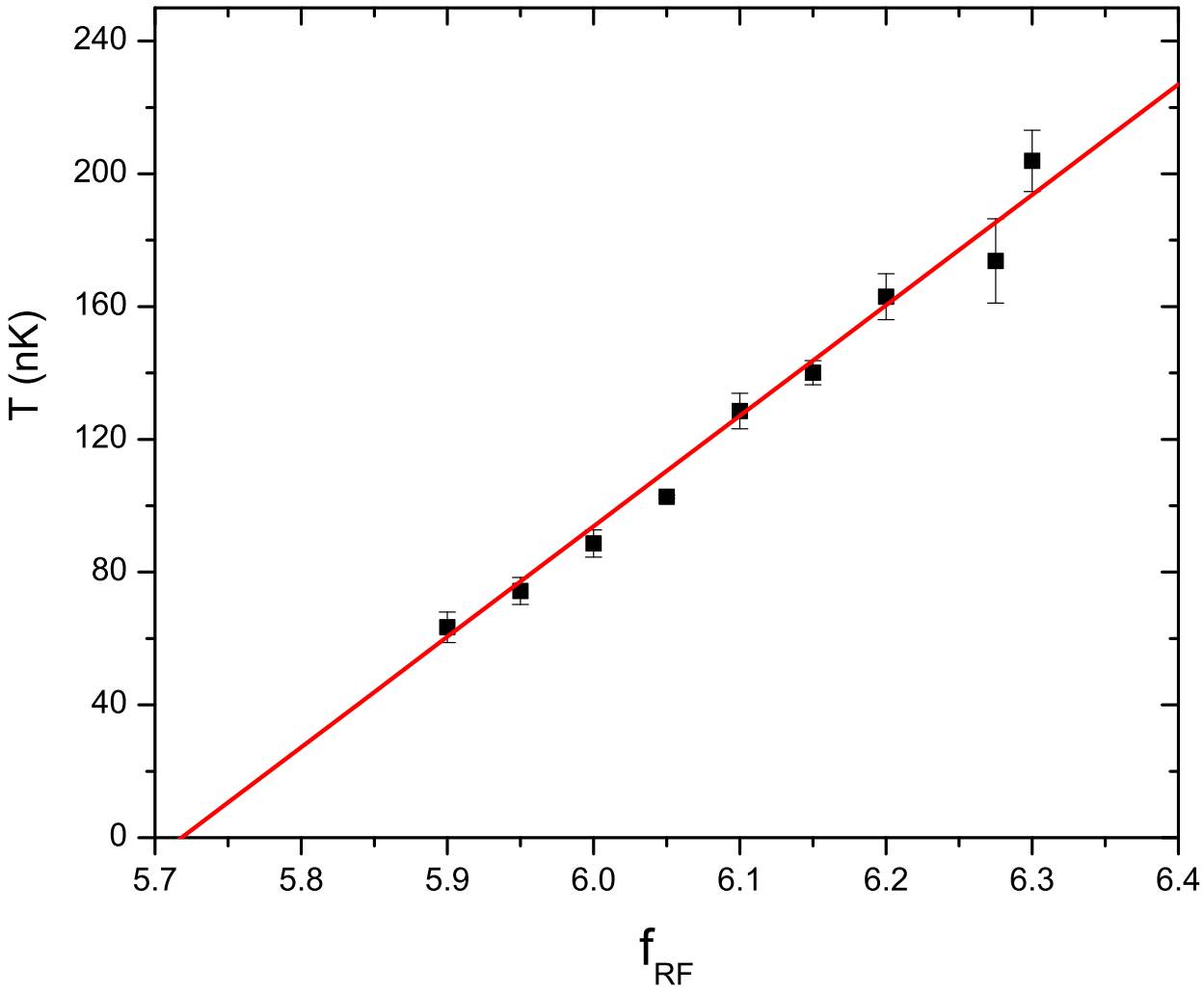

Figure 3.4: Temperature vs frequency of the RF knife. The temperature is obtained from the fit of the *in-situ* images of the atoms in the central layer of the 1D optical lattice. The red line is the linear fit to the data.

as

$$I_s(x,y) = (1-\alpha)I_0 e^{-OD(x,y)} + \alpha I_0, \tag{3.14}$$

where α represents the small fraction of the light in I_0 that cannot interact with the atomic sample because of polarization imperfection and tails in the laser-frequency distribution. Here $OD(x,y)$ is defined as

$$OD(x,y) = \int n(x,y,z)\sigma_0 dz, \tag{3.15}$$

where $n(x,y,z)$ is the density of the atomic sample, and σ_0 is the scattering cross-section. As one can see, $OD(x,y)$ can be found by taking

$$OD(x,y) = \ln \frac{(1-\alpha)I_0}{I_s(x,y) - \alpha I_0}. \tag{3.16}$$

However, the CCD camera does not distinguish the light that can interact with the atom from light that cannot. The quantity we actually measure from the camera is OD_{meas} which is defined as

$$OD_{meas} = \ln \frac{I_0}{I_s(x,y)}. \tag{3.17}$$

Equation (3.16) can be rewrittten using OD_{meas}. One can show that

$$OD(x,y) = OD_{meas}(x,y) + \ln(1-\alpha) - \ln(1-\alpha e^{-OD_{meas}(x,y)}). \tag{3.18}$$

If α and $\alpha e^{OD_{meas}}$ are both small numbers ($\ll 1$), the difference between $OD(x,y)$ and $OD_{meas}(x,y)$ can be approximated as

$$OD - OD_{meas} = \alpha(e^{OD_{sat}} - 1). \tag{3.19}$$

In our experiment, $\alpha \approx 3\%$, which gives about a 10% correction if the maximum OD reaches 2. OD_{meas} reaches its saturation value OD_{sat}, when $(1-\alpha e^{OD_{sat}}) = 0$. Thus, α can be determined by saturating OD_{meas} according to

$$\alpha = e^{-OD_{sat}}. \tag{3.20}$$

Although one can correct this saturation effect, it is not recommended because the OD_{meas} is particularly sensitive near OD_{sat}. Any imaging imperfection can cause large fluctuations in the OD correction. Often times, α is also position dependent. If one can stay away from the saturation value of OD_{meas}, one can still have a relatively linear mapping from OD_{meas} to OD. However, a 3% non-interacting light gives a saturation value of 3.5. The linear range ($< 10\%$ correction) for the OD_{meas} would just be $0 < OD_{meas} < 2$. This lack of a linear dynamic range is one of the drawbacks of the absorption-imaging method. In our experiments, we limited OD_{meas} to a value smaller than 2 by putting only a small number of atoms into the imaging state. We also allowed the atomic cloud to expand axially for 1 ms, which helps reduce the atomic density by a factor of 8, before the probing beam was fired. This trick does not change the optical depth of atoms, but does help reduce imaging artifacts. To convert the optical depth to a real atomic density, one has to know σ_0, which is the scattering cross-section. However, the scattering cross-section depends strongly on the polarization, the detuning of the probing beam, and the population of the atoms. This makes accurate determination of the value of σ_0 difficult. In our experiments, the scattering cross-section, together with the transfer percentage, is the fitting parameter η. For a two-level atom interacting with resonant light, the on-resonant scattering cross-section σ_0 can be easily calculated [40]; $\sigma_0 = 3\lambda^2/2\pi$.

Our line-of-sight is along the axis of tight confinement, which means we do not need to do a deconvolution of our images to get the 2D density distribution. After the probing sequence, we extract the OD image according to Eq. (3.17). As mentioned earlier, our trap is axially symmetric. Thus, the OD images also share the same symmetry. The axial symmetry in the image of the atomic sample allows us to take azimuthal averages to minimize the statistical noise in the absorption images, as shown in Fig. 4.3.

In our experiment, the intensity of the probing beam I is approximately 0.1 I_s, where I_s is the saturation intensity for the atomic transition. The photon-scattering rate of the

atoms, Y, is given by

$$Y = \Gamma \rho_{ee}, \tag{3.21}$$

where Γ is the decay rate of the excited state, which is $(26\,ns)^{-1}$ for the transition of $|F = 2\rangle \rightarrow |F' = 3\rangle$, and ρ_{ee} is the population in the excited state, which is obtained by solving the optical Bloch equation [40]. ρ_{ee} is given by

$$\rho_{ee} = \frac{S_0/2}{1 + S_0 + (\frac{2\Delta}{\Gamma})^2}, \tag{3.22}$$

where $S_0 \equiv$ (probing beam intensity I / saturation intensity I_s), Δ is the probing detuning, and Γ is the natural linewidth of the excited state. In the low-intensity regime, the scattering rate is proportional to the intensity, i.e., $Y \simeq \Gamma(S_0/2)$. In this case, the attenuation of the light passing the atomic sample is well described by the Beer's law, which leads to Eq. (3.14).

The intensity of the probe beam is 0.1 I_s with a resonant frequency. The duration of the probing time is set to 50 μs. During this time duration, an atom can scatter on average 100 photons. This scattering gives a 0.75 MHz Doppler shift and moves the atom 1.4 μm away from its original position (the imaging plane). These are both negligible effects.

3.3.1 *In-situ* imaging method

In this method, the atoms are first prepared in the $|F, m_f\rangle = |1, -1\rangle$ state in the TOP trap. Then, the 1D optical lattice is turned on. The 1D optical lattice slices the atomic cloud into many layers. Tunneling between layers is negligible. Therefore, every single layer can be viewed as an isolated 2D system. Atoms in individual layers are allowed to thermally equilibrate before probing occurs.

We implement the *in-situ* imaging method as follows: First, we turn off the rotating bias field such that the atomic cloud sees a transient magnetic-field gradient B'_z . Second, we turn on an extra bias field along the $\hat{z}$ direction to reduce the magnetic-field curvature across the 2D cloud. Third, we apply a weak microwave pulse to pump a small fraction of

the atoms in one layer from $|1,-1\rangle$ to $|2,-1\rangle$, as shown in Fig. 3.5(a). Fourth, we turn off the the optical lattice to reduce the stray light on the camera. We also turn off most of the magnetic fields to increase the pumping efficiency for the probe light. Finally, we fire the probing beam, which is resonant at the $|F=2\rangle \rightarrow |F'=3\rangle$ transition with σ^+ polarization. Details of the experimental sequence are shown in Fig. 3.6.

By sweeping the frequency of the microwave pulse, we can see a layer structure on the number of atoms we transfer into the imaging state, as shown in Fig. 3.7. Given that the magnitude of B'_z is 7.8 G/mm, a measured energy splitting of $h * 40$ kHz between adjacent layers gives a lattice constant of 3.8 μm. This measured lattice constant is in good agreement with the one calculated from Eq. (3.4), which using the measured angle, $\theta = 8°$, between the two interfering beams.

3.3.2 Focusing-imaging method

Measuring momentum-space distribution is more difficult than it first sounds. Conceptually, it can be done by turning off atom-atom interactions, turning off the confinement, allowing the cloud to expand ballistically for a very long time, and delaying the absorption image until the position of each atom is determined by its initial momentum (not by its initial position in the cloud). Comparing this process to the well-known time-of-flight method, we anticipate two difficulties: turning off interactions and obtaining a sufficiently long expansion time.

To remedy these problems, one needs to find a way to turn off the interactions and make the required expansion time shorter. The method we use is a temporal-focusing technique that we refer to as the"focusing" imaging method. We first select a single layer via microwave pulses. Then, we turn off the optical lattice and let the layer expand into a purely magnetic trap (TOP). Because of the 140:1 aspect ratio of the cloud, the resulting expansion is initially purely axial, which very rapidly reduces the 3D density (and thus the strength of the atom-

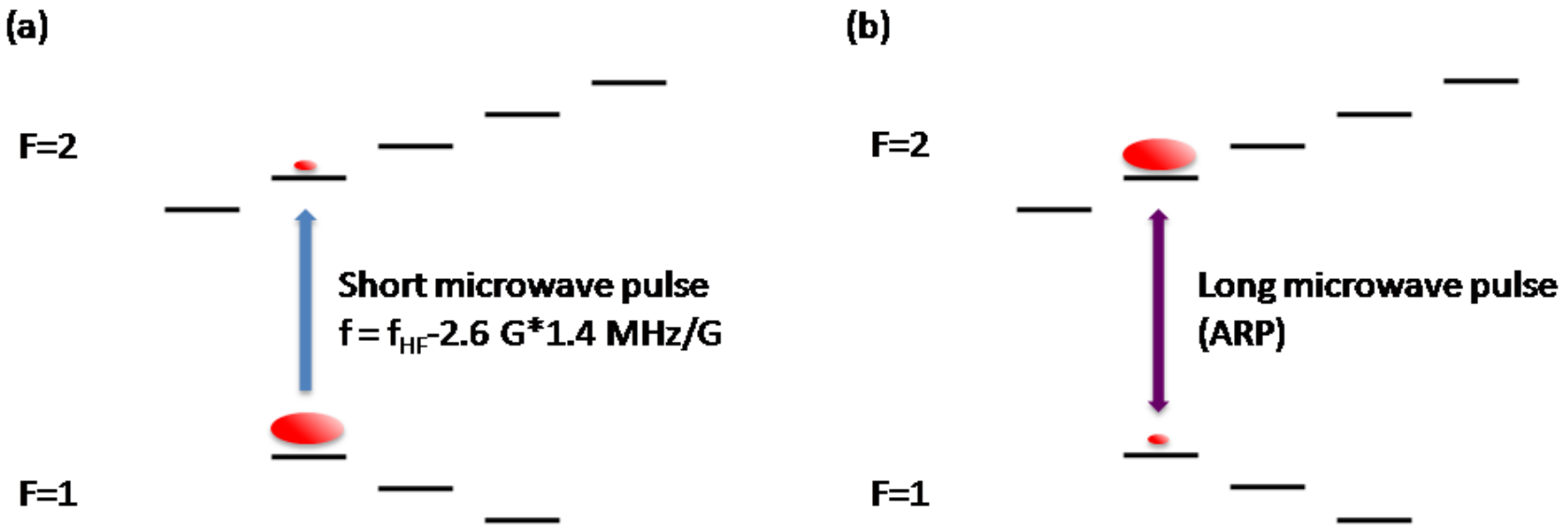

Figure 3.5: Drawing of the atomic population during the imaging processes. (a) In the *in-situ* imaging method, a weak microwave pulse pumps a small number of atoms in one layer from $|1,-1\rangle$ to $|2,-1\rangle$ for imaging. (b) In the focusing-imaging method, a second strong microwave pulse, together with a time-varying magnetic field, is applied to swap the population between $|1,-1\rangle$ and $|2,-1\rangle$. The atoms in $|1,-1\rangle$ will still be trapped, while the atoms in the $|2,-1\rangle$ will be ejected from the trap. During focusing, after the atoms in $|2,-1\rangle$ are all gone, a pumping laser is fired to put the atoms in $|1,-1\rangle$ back to $|2,-1\rangle$ for imaging.

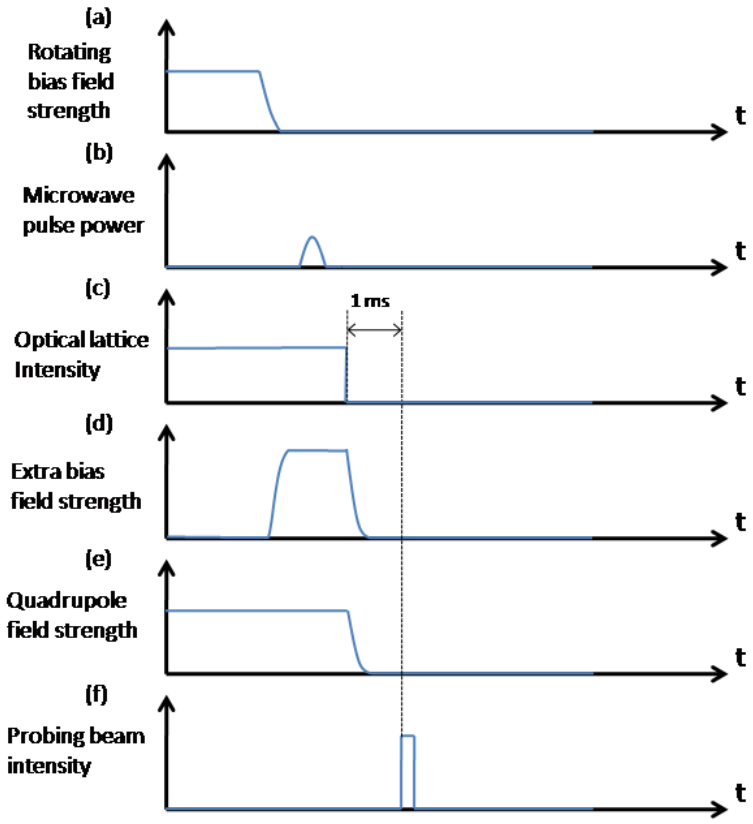

Figure 3.6: Qualitative schematic (not to scale) of the experimental timing of the *in-situ* imaging method. (a) The magnitude of the rotating bias field B_0 is 7.3 G. The rotating bias field is turned off 1 ms before the microwave pulse fires. (b) The duration of the microwave pulse is 50 μs. (c) The 1D optical lattice is turned off 1 ms before the probing occurs. (d) The magnitude of the extra bias field B_{ex} is 24 G. This extra bias field is turned on at the same time as the rotating bias field is turned off. (e) The magnitude of the magnetic-field gradient is 7.8 G/mm. (f) The duration of the probing beam is 50 μs.

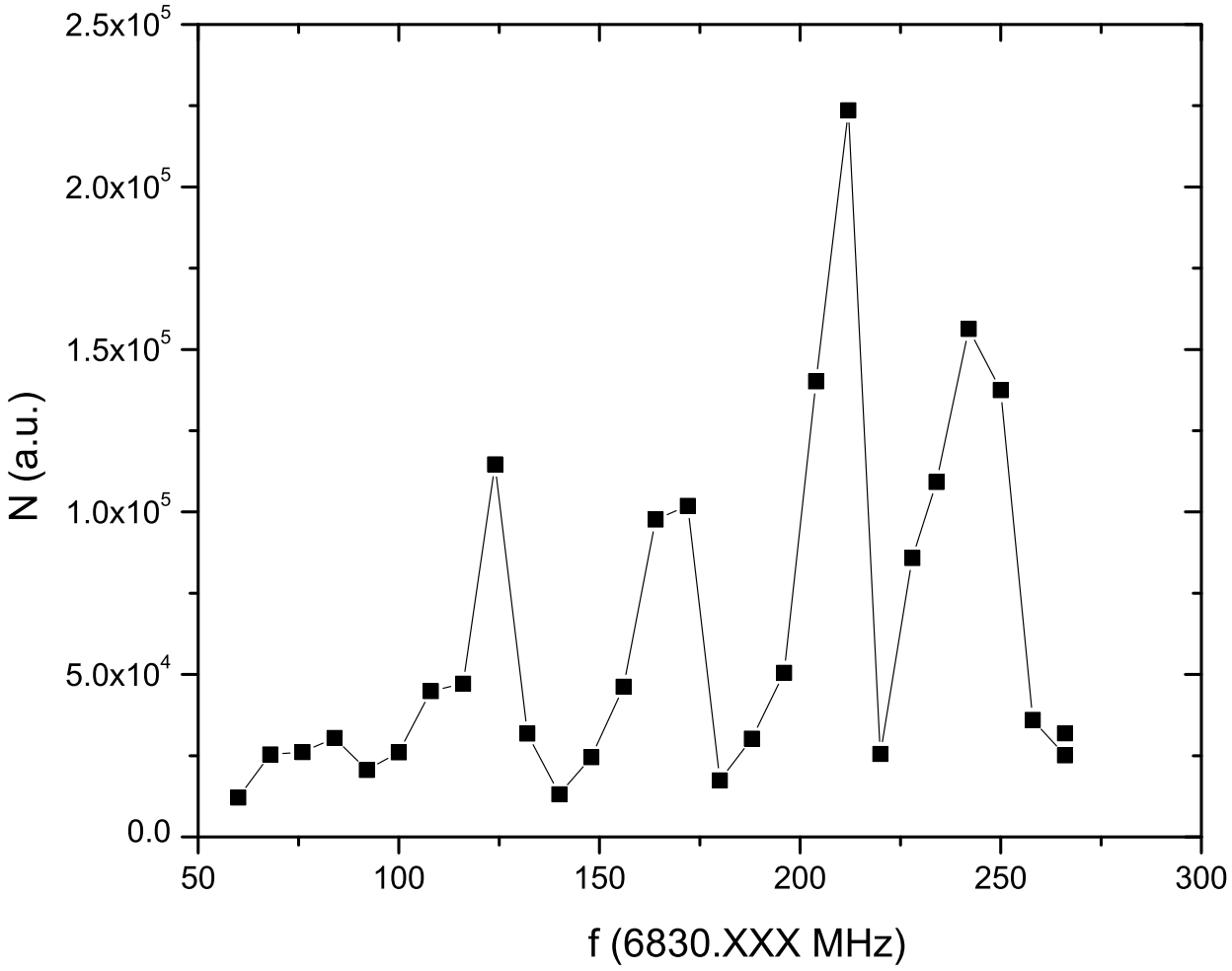

Figure 3.7: Atom number N vs microwave frequency f of the short pumping microwave pulse. This plot shows a layer structure of the atomic sample. The data is taken continuously over one hour. The lattice constant derived from the data is 3.8 μm.

atom interactions). This expansion does not affect the in-plane coordinate- or momentum-space distributions. After the near-instantaneous suppression of the (repulsive) atom-atom interactions, each atom undergoes essentially free motion in the radially symmetric harmonic confinement in the x-y plane. At the focused time, $t_f = \frac{1}{4}\frac{2\pi}{\omega_r}$, the initial radial-momentum distribution is mapped onto the final-coordinate space distribution, and vice versa. At the point, we take an absorption image and scale the spatial coordinate by $m\omega_r$ to get the momentum-space distribution that existed just as the focusing sequence began. This focusing technique is an extension to 2D of a procedure originally developed for imagining 1D momentum distributions [11, 12].

The focusing-imaging method proceeds as follows: First, we turn off the rotating bias field in the TOP trap. Then we use a short microwave pulse to pump a small fraction (5%) of the atoms that are in one single layer from $|1,-1\rangle$ to $|2,-1\rangle$. An extra bias field is added to reduce the magnetic curvature across the 2D cloud. This step is identical to step 1 of the *in-situ* imaging method. Second, we turn off the optical lattice, and fire the second microwave pulse and ramp down the extra bias field. This step exchanges the population in $|1,-1\rangle$ and $|2,-1\rangle$ through an adiabatic rapid passage (ARP), as shown in Fig. 3.5(b). Third, we turn the rotating bias field back on and shift the extra bias field to a new value. Fourth, we wait until the momentum-space distribution is mapped onto the coordinate space. Finally, we turn off most of the magnetic fields before firing the probing beam. The details of the experimental sequence are shown in Fig. 3.8.

The mapping of the in-plane momentum-space distribution and the in-plane coordinate-space distribution at the focused time t_f can be understood using a classical harmonic oscillator model. This model works well for describing the in-plane motion of a 2D Bose gas since the interaction between atoms is greatly suppressed soon after the optical lattice is turned off. The equations of motion of an atom with a initial velocity $\dot{r}(0)$ at the initial position

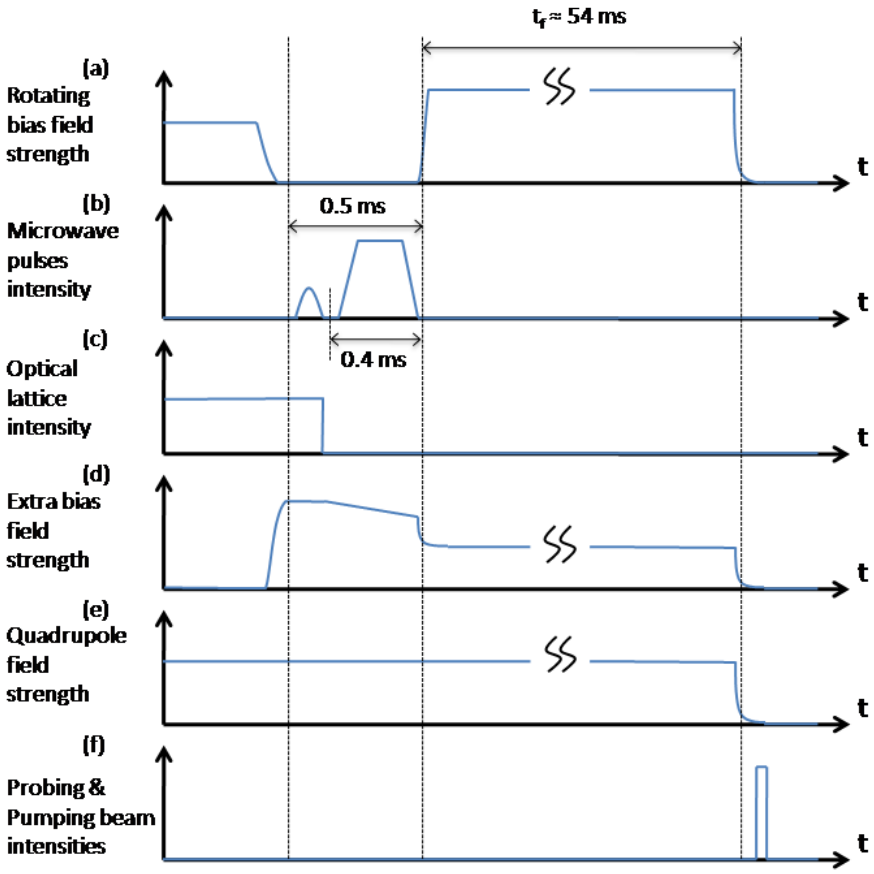

Figure 3.8: Qualitative schematic (not to scale) of the experimental timing of the focusing-imaging method. (a) The rotating bias field is switched back after the second microwave (ARP) pulse. The magnitude of the bias field is changed from its original value of 7.3 G to 35 G. Therefore, the trapping frequencies of the TOP trap change from $(\omega_r, \omega_z) = 2\pi(10.2, 22.4)$Hz to $2\pi(4.5, 10.8)$Hz. We switch to a weaker trap to increase the focused time t_f, and thus, increase the sensitivity of the imaging method. (b) The second microwave (ARP) pulse is on for 400 μs. (c) The optical lattice is turned off after the first microwave pulse. (d) The extra bias field is ramped down during the ARP pulse, then switched to 13 G to bring the center of new TOP trap back to the imaging plane (its original position). The magnetic fields (a), (d), and (e) are turned off before the probing occurs to avoid off-resonant pumping. During the probing process, a pumping beam is added to pump atoms from the $|1, -1\rangle$ state to the $|2, -1\rangle$ state to interact with the probing beam. (f) Within 1 ms, after most of the magnetic fields are turned off, the probing beam fires.

$r(0)$ in a harmonic potential are

$$r(t) = r(0)cos(\omega_r t) + \frac{\dot{r}(0)}{\omega_r} sin(\omega_r t), \tag{3.23}$$

$$\dot{r}(t) = -r(0)\omega_r sin(\omega_r t) + \dot{r}(0)cos(\omega_r t), \tag{3.24}$$

where ω_r is the trapping frequency of the confining harmonic potential. At the focused time, $t_f = \pi/2\omega_r$, one gets

$$m\dot{r}(0) = m\omega_r r(t_f), \tag{3.25}$$

$$\omega_r r(0) = -\dot{r}(t_f). \tag{3.26}$$

From Eqs. (3.25) and (3.26), one can see the initial radial momentum-space distribution is mapped onto the final coordinate-space distribution at the focused time t_f, and vice versa, to within a scaling factor of $m\omega_r$. At this point we can probe the cloud and reconstruct the momentum distribution more accurately as compared to previous experiments [13, 14].

If the ratio of the trapping frequencies, ω_z/ω_r, is set to 2, at the focused time, the axial motion of atoms makes a half oscillation and returns to its original size, while the radial motion of atoms bring them to the center of the trap. At the focused time, the density of the focused cloud might have an even higher density than it had before focusing. The trapping frequency ratio in our experiment is set to a value slightly below 2. In this case, when the in-plane momentum-space distribution is mapped to coordinate space, the size of the cloud in the axial direction is not yet at its minimum. Therefore, it lowers the density of the cloud at focused time such that the interactions do not influence the focussing dynamics.

Chapter 4

Analysis of *in-situ* images

In our experiment, the thermal energy of the system, k_bT, is on the same order with $\hbar\omega_z$. Therefore, there will be populations on the axial excited state. The line of sight of our imaging system aligns along the $\hat{z}$ axis. Therefore, in the images we cannot distinguish those populations from a ground-state population, which is the one that we are really interested in. To extract a ground-state signal for BEC physics from our data, we calculate the axial excited-state populations via a model, which is, in essence, the same model that the Paris group calls the Hartree-Fock, mean-field, local-density approximation [10].

4.1 The semiclassical mean-field model

For bosons, the mean occupation of a single-particle state with wavevector k is given by the the Bose-Einstein distribution, $N_k = \frac{1}{e^{(E_k-\mu)/k_bT}-1}$, where E_k is the energy of the state. For our system, the thermal energy $k_BT \gg \hbar\omega_r$, but $k_BT \sim \hbar\omega_z$. We treat the atomic motion semiclassically in the horizontal direction, while preserving discrete harmonic-oscillator quantum levels in the z-direction. Thus, we get the two dimensional (2D) coordinate-space density in the j^{th} axial level

$$n_j(\vec{r}) = \frac{1}{h^2}\iint \mathrm{d}^2\vec{p}\frac{1}{e^{(\varepsilon(\vec{p})+\theta_j(\vec{r})-\mu_j)/k_bT}-1}, \tag{4.1}$$

where h is Planck's constant, $\varepsilon(\vec{p}) = \frac{p^2}{2m}$ is the free particle dispersion, and the local chemical potential for the j^{th} level is given by

$$\mu_j = \mu^{global} - \frac{1}{2}m\omega_r^2 r^2 - j\hbar\omega_z - \sum_{l\neq j} 2(\frac{4\pi\hbar^2}{m}a_s f_{lj} n_l(\vec{r})). \tag{4.2}$$

The intralevel interaction energy is given by

$$\theta_j(\vec{r}) = 2(\frac{4\pi\hbar^2 a_s}{m}) f_{jj} n_j, \tag{4.3}$$

and the relevant mean-field interaction energies depend on f_{jl}, which are the appropriately normalized overlap integrals over the axial dimension between densities associated with the axial quantum states j and l. With per-particle interaction energies comfortably less than the axial energy spacing $\hbar\omega_z$, it is safe to treat interlevel axial interactions with what is, in essence, first-order perturbation theory. Evaluating the integral in Eq.(4.1), one gets

$$n_j(\vec{r}) = -\ln(1 - e^{(-(\theta_j(\vec{r}) - \mu_j(\vec{r}))/k_b T)})/\lambda_{db}^2, \tag{4.4}$$

where the deBroglie wavelength $\lambda_{db} = \sqrt{\frac{2\pi\hbar^2}{mk_b T}}$. For any given value of μ and T, n_j are determined self-consistently. For $k_b T \lesssim \hbar\omega_z$, the model converges in just a few iterations.

To get a better understanding of Eq. (4.4), one can break down the model into three approximations: (1) the local-density approximation (2) the semiclassical approximation, and (3) the mean-field approximation. These approximations are discussed below:

4.1.1 Local-density approximation

The local-density approximation can be applied to a system where the density of the atomic cloud does not change significantly over the distance of the de Broglie wavelength of an atom. This approximation works surprisingly well with magnetic traps, especially a weak trap, like the one with $\omega_r = 2\pi * 10$ Hz in our experiment . The local-density approximation divides the system into many small boxes. Atoms inside each box are treated as if they were in a homogeneous potential with a potential offset determined by the external potential.

In this way, we can define a "local" chemical potential, a "local" density, and a "local" phase-space density in each box.

4.1.2 Semiclassical approximation

The benefit of using the local density approximation is that it is very easy to find the energy excitations for a free particle inside a box. For an ideal Bose gas confined in a box potential, the total number of atoms in excited states as a function of the chemical potential is given by

$$N_{ex} = \sum_{i>0} \frac{1}{e^{(E_i-\mu)/k_bT} - 1}, \tag{4.5}$$

where $E_i = \frac{\hbar^2}{2m}(\frac{2\pi}{L}\vec{n}_i)^2$, and μ is the chemical potential. Replacing the summation in Eq. (4.5) with the integral, one gets

$$N_{ex} = \frac{L^q}{(2\pi\hbar)^q} \int d^q\vec{p}\, \frac{1}{e^{(\varepsilon(p)-\mu)/k_bT} - 1}, \tag{4.6}$$

where $\varepsilon(p) = p^2/2m$, and q is the dimensionality of the system. As one can see, the dispersion relation is a classical single-particle dispersion. This is the "classical" part of the model. For two dimensions, $q = 2$, and the integral in Eq. (4.6) can be carried out, leading to Eq. (**??**).

In a 2D harmonic trap, as a result of the local-density approximation, the chemical potential in Eq. (**??**) is offset by the external potential; it should be replaced by the "local" chemical potential, i.e.,

$$\mu' = \mu - \frac{1}{2}m\omega_r^2 r^2. \tag{4.7}$$

This substitution leads to the semiclassical model for an ideal Bose gas in a 2D harmonic trap without mean fields, i.e.,

$$n_{ex} = \frac{1}{\lambda_{db}^2} \ln(1 - e^{(\frac{1}{2}m\omega_r^2 r^2 - \mu)/k_bT}). \tag{4.8}$$

4.1.3 Mean-field approximation

Considering an interacting Bose gas, the easiest way to take into account the interactions might be via the introduction of mean fields. In the framework of mean-field theory, a many-body system with interactions is replaced with a free particle moving in an effective potential. The mean field in our system consists of two parts: Intralevel and interlevel interactions. The "level" here means the energy levels of the axial-confining potential, which we assume is quadratic.

Consider a quasi-2D system where the horizontal-confining potential is homogeneous and the axial-confining potential is quadratic. If N_j is the number of atoms in the j^{th} axial excited state, the density in the j^{th} level is

$$\frac{N_j}{L^2}\left|\psi_j(z)\right|^2, \tag{4.9}$$

where L^2 is the area of the quasi-2D system. An atom in the j^{th} axial level feels a mean field created by the other atoms in the same level:

$$\begin{aligned}\theta_j =& 2\frac{U_0 N_j}{L^2}\int dz\left|\psi_j(z)\right|^4 \\ =& 2(U_0 f_{jj})n_j \\ =& 2u_{jj}n_j,\end{aligned} \tag{4.10}$$

where n_j is the 2D density and $U_0 = 4\pi\hbar^2 a_s/m$. The factor of two arises from an implicit assumption that the second-order correlation function at zero distance is two, as it would be for fully fluctuating nondegenerate ideal bosons. The overlap integral represents the joint probability of finding two atoms in the same level at the same position, z. As one can see from Eq. (4.10), the 3D interaction strength U_0 is renormalized by the overlap integral, f_{jj}, to get the effective 2D interaction strength u_{jj}. The assumption that the scattering process is still 3D is verified by the fact that the axial length of the quasi-2D system is still much greater than the 3D-scattering length, i.e., $l_z \gg a_s$ [41].

Similarly, for an atom in the j^{th} level, the mean field created by all the atoms in the i^{th} level is $2u_{ij}n_i$. u_{ij} is defined as

$$\begin{aligned} u_{ij} =& U_0 f_{ij} \\ =& U_0 \int dz \left|\psi_i(z)\right|^2 \left|\psi_j(z)\right|^2 . \end{aligned} \tag{4.11}$$

Thus, the total interlevel mean field is

$$\sum_{i>j} 2u_{ij}n_i. \tag{4.12}$$

For convenience, the interlevel mean-field energies are bundled with the chemical potential μ, radial-confining potential $\frac{1}{2}m\omega_r^2 r^2$, and the axial-excitation energy $j\hbar\omega_z$ such that the local chemical potential is

$$\mu_j = \mu - \frac{1}{2}m\omega_r^2 r^2 - j\hbar\omega_z - \sum_{i>j} 2u_{ij}n_i(\vec{r}), \tag{4.13}$$

which is is identical to Eq. (4.2). With Eqs. (4.8), (4.10), and (4.13), one recovers Eq. (4.4).

4.1.4 The "no-condensate" model

Looking at Eq. (4.4), it's clear why we call this the no-condensate model. For a given value of T, we can choose a value of μ_0 such that the model predicts an arbitrarily large n_0, even one for which $n_0\lambda_{db}^2 \gg 1$, without requiring a singularity at $p = 0$. More importantly, however, this is a model from which all the many-body "magic" associated with degenerate bosons has been intentionally omitted. There's no hint of the presence of anything like a phonon or other collective excitation. Still, the no-condensate model should do very well where the phase-space density $\rho_j \equiv n_j\lambda_{db}^2 < 1$. As for the calculated value of $n_0(\vec{r})$, a comparison with the naive no-condensate n_0 allows us to quantify the tell-tale discrepancy.

Several interesting features can be found by solving Eq. (4.4). Figure 4.1 shows the solutions of Eq. (4.4) graphically for five different chemical potentials. First, from Fig. 4.1, one can see that as μ_j/kT reaches 0.24 and beyond, the density that satisfied Eq. (4.4) is

well approximated by $(\pi/\tilde{g})(\mu_j'/k_bT)\lambda_{db}^2$. With the fact that $\mu_j' \sim \mu - \frac{1}{2}m\omega_r^2 r^2$, the density profile is an inverse parabola, as shown in Fig. 4.2. Since Eq. (4.4) is a no-condensate model, the appearance of bimodality does not imply the existence of a condensate phase, as opposed to the 3D case. Second, one can see from Fig. 4.1 that there always exists a solution for Eq. (4.4) for any chemical potential. This is another way of saying that this model predicts no condensate.

4.2 Compressiblity

The isothermal compressibility is a quantity that measures a system's ability to be compressed at fixed temperature. The definition of the isothermal compressibility is given by

$$\kappa \equiv -\frac{1}{V}\left(\frac{\partial V}{\partial P}\right). \tag{4.14}$$

Using a thermodynamic relation, one can prove that

$$\begin{aligned} \left(\frac{\partial \bar{N}}{\partial \mu}\right)_{T,V} &= \frac{\bar{N}^2}{V}\kappa, \\ \text{or} \quad \left(\frac{\partial \bar{n}}{\partial \mu}\right)_{T,V} &= \bar{n}^2\kappa, \end{aligned} \tag{4.15}$$

where $\bar{N}$ is the average number of atoms in the system, and $\bar{n} = \bar{N}/V$. The quantity

$$\left(\frac{\partial \bar{n}}{\partial \mu}\right)_{T,V}, \tag{4.16}$$

which we call *scaled* compressibility, is extracted from our data and compared to the no-condensate model.

An analysis of a coordinate-space image proceeds as follows. The interesting physics lie in $n_0(\vec{r})$, but we measure a density integrated through all the axial states, $n_{meas}(\vec{r}) = \sum n_j(\vec{r})$. Initially, we get an estimate of T, μ, and the OD scale (a multiplicative factor that relates the observed OD to the n_{meas}). In principle, the OD scale is calculable from the crosssection of an atom absorbing light from a probing laser beam. However, drifts in the

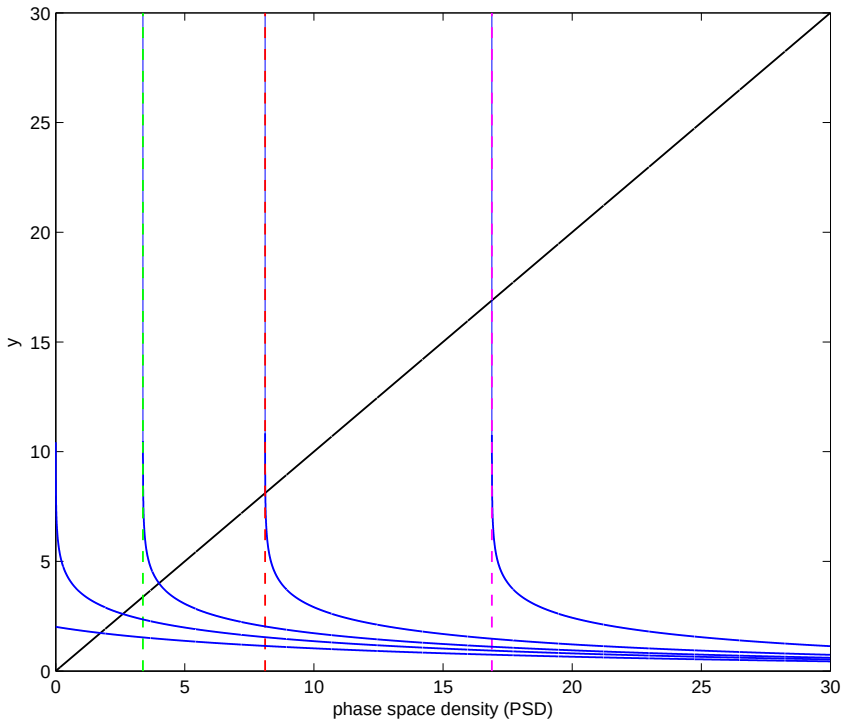

Figure 4.1: The solution of Eq. (4.4) for five different chemical potentials. The blue curves represent $y = -\ln(1 - e^{(-(\theta_j(\vec{r})-\mu_j(\vec{r}))/k_bT)})$ for five different chemical potentials μ'/k_bT, -0.14, 0 , 0.1, 0.24, and 0.5 (from left to right). The black curve represents $y = n\lambda_{db}^2$. The intersection for each blue curve and the black curve gives the density that satisfies Eq. (4.4). The three dashed lines indicate the values of the phase-space density where the last three blue curves diverge.

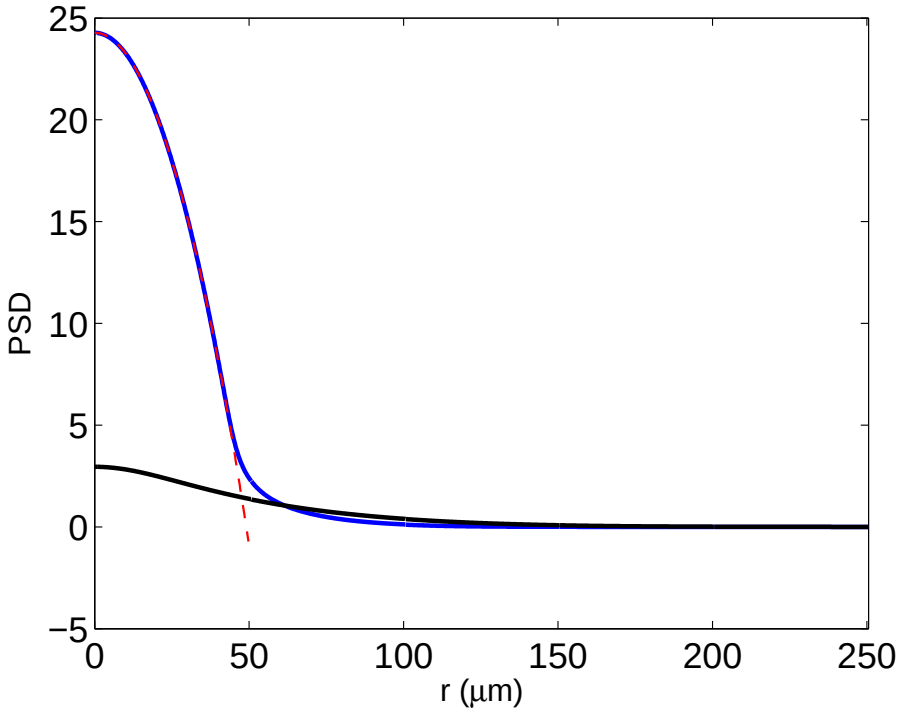

Figure 4.2: Coordinate-space distributions calculated from Eq. (4.4). The blue curve is calculated with a chemical potential $\mu = 50$ nK and a temperature T = 70 nK. The black curve is calculated with $\mu = 6$ nK, and T=180 nK. The dashed line is an inverse parabola for comparison with the central part of the distribution from the blue curve.

efficiency of our microwave-selection pulse cause uncertainties in the OD scale. The estimate comes from comparing the results of the no-condensate model to observed n_{meas} and fitting the parameters T, μ and OD scale to the low phase-space regions of the cloud. With the chemical potential and temperature obtained from the fit, we can use Eq. (4.4) to evaluate the excited-state distributions. Then, we find numerically a self-consistent solution to solve n_j and n_0, where $n_0 = n_{meas} - \sum n_k$, as shown in Fig. 4.3.

Once the corrected ground-state distribution, n_0, is extracted from n_{meas}, we calculate the scaled compressibility, κ_s, at each imaging pixel, according to

$$\kappa_s = \frac{dn_0}{d\mu_{local}} = \left.\frac{dn_0}{dr}\right|_{r=i} * \left.\frac{d\mu_0}{dr}\right|^{-1}_{r=i}, \tag{4.17}$$

where i is the number index for camera pixels. Although μ is not a quantity we can know with great accuracy in a model-independent way, $d\mu_0/dr = -dV_{eff}/dr \approx -m\omega_r r$ is readily determined quite precisely, as the corrections to V_{eff} arising from the mean field of the axially excited atoms are small and calculable. dn_0/dr is determined pixel by pixel from the values extracted from our coordinate-space images. Combining the two spatial variations for each pixel according to Eq. (4.17), we then get the scaled compressibility at every discrete radius in our images. We plot the result vs the local ground-state phase-space density, $\rho_0 = n_0\lambda_{db}^2$, in Fig.4.4.

We compare our empirically scaled compressibility with the value given by the no-condensate model at the same density. For an observed value of n_0, we numerically solve the no-condensate prediction, $n_0 = -\ln(1 - exp(\mu_0 - \theta_0(n_0))/k_bT)/\lambda_{db}^2$, for μ_0. We then numerically determine how n_0 would change for a small change in μ_0. Thus, we extract a scaled no-condensate compressibility, which is plotted in Fig.4.4.

As a check of the local-density approximation that is central to our analysis, we show images from two very different classes. The first, Fig. 4.4(a), for images with $T = 171$ nK and a central ρ_0 of about 9, and the second, Fig. 4.4(b), for images with $T = 128$ nK and a central ρ_0 of about 30. In both cases, the shape of the data is the same, and, in particular,

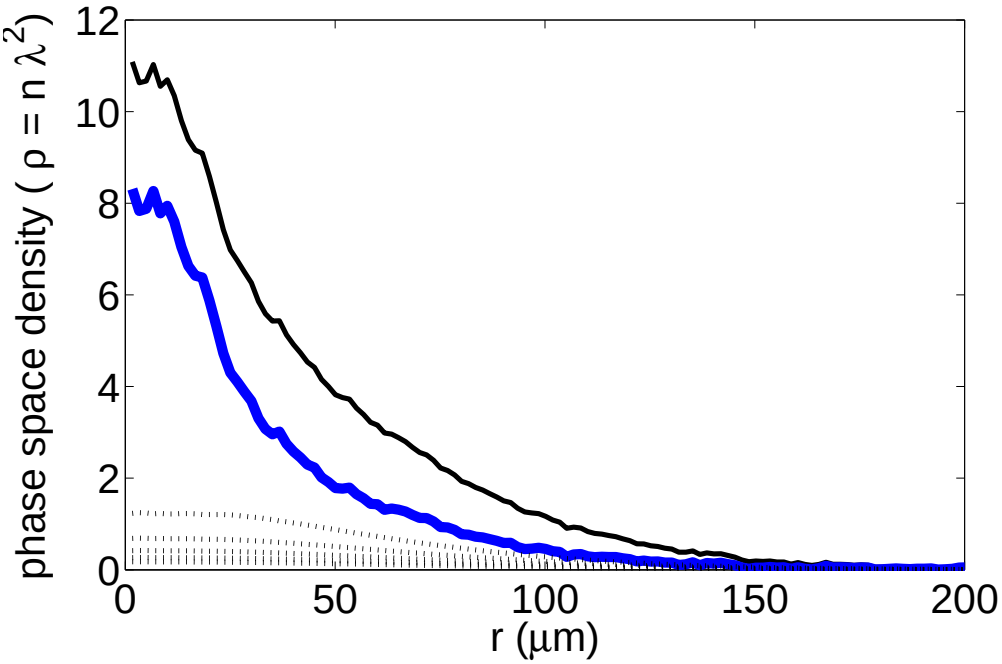

Figure 4.3: Azimuthally averaged data from a coordinate-space image. The thin line shows the measured density n_{meas} obtained from an *in-situ* image. The dashed lines are the calculated distributions from excited axial levels n_j, j=1 to 5, from top to bottom. The thick line shows the pure axial ground-state distribution after correcting for $n_{j>0}$.

the value of ρ_0 for which the empirical κ begins to deviate strongly from the no-condensate model κ in both cases is about 4.

A note on the overall reliability of our data: when we allow our fitting routine to consider only low phase-space regions of images, so that we can extract model-independent fit values of T, μ^{global}, and the OD scale, we find that the fits are insufficiently orthogonal in the latter two parameters. Large uncertainties in μ^{global} and OD scale result. We improve the precision by fixing the OD scale using independent measurements of very low T clouds in which the atoms are in a Thomas-Fermi inverted parabola with negligible noncondensed wings. In this limit, we make the assumption that μ^{global}=$u_{00}n_0(0)$. Fixing our OD scale with this assumption means that our scaled values of κ, as shown in Fig. 4.4, are constrained to saturate to 2.0 at very high ρ_0. In essence, we get high-precision measurements of the behavior for exotic intermediate values of ρ_0, for the price of assuming a priori a good understanding of low-degeneracy, mean-field behavior at high T, and long-coherence pure-condensate behavior at low T.

4.2.1 Discussion

From the thermodynamic relations [42, 43], the number fluctuation for an ideal Bose gas can be expressed in terms of scaled compressibility $(\partial n_k/\partial\mu)$, i.e.,

$$\langle n_k^2\rangle - \langle n_k\rangle^2 = k_b T\frac{\partial\langle n_k\rangle}{\partial\mu}, \tag{4.18}$$

where k represents the k^{th} excited state for a 2D box. The mean occupation number for the state k is given by Bose statistics as

$$n_k = \frac{1}{e^{(\frac{\hbar^2k^2}{2m}-\mu)}-1}. \tag{4.19}$$

Differentiating Eq. (4.19) with respect to μ, one can rewrite Eq. (4.18) as

$$(\Delta n_k)^2 = \langle n_k\rangle + \langle n_k\rangle^2, \tag{4.20}$$

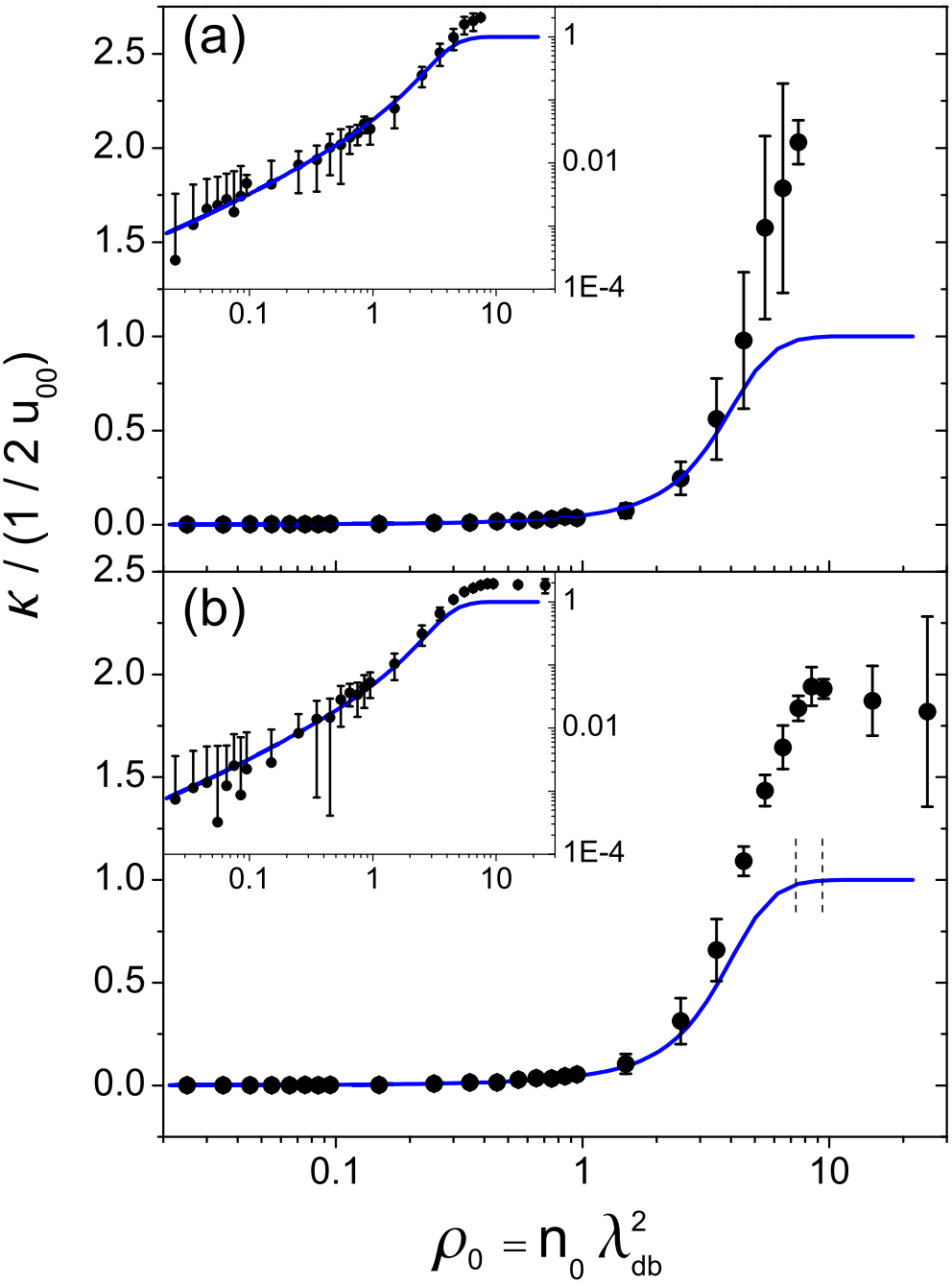

Figure 4.4: Compressibility κ vs phase-space density ρ_0. (a) Measured κ extracted from images of samples at the same T as for the image in Fig. 5.2(c). Black circles are data averaged over the values calculated from images of three separate clouds. The blue curves are κ_{nc} derived from the no-condensate model. (b) Same but with κ extracted from images of lower-T samples. The paired vertical dotted lines indicate the location of the jump in coherence discussed in the text.

where $\Delta n_k = \sqrt{\langle n_k^2 \rangle - \langle n_k \rangle^2}$. One can see that the number fluctuation of state k comes from two parts: The first term in Eq. (4.20) is atom shot noise, and the second term is excess noise coming from the bunching effect [44, 45]. If there are N atoms occupying α states in a 2D box, one can show, using Eq. (4.20), that the number fluctuation of those N atoms in the 2D box can be written as

$$\langle N^2 \rangle - \langle N \rangle^2 = \langle N \rangle + \sum_{k=0}^{\alpha-1} \langle n_k \rangle^2, \tag{4.21}$$

where $N = \sum_k n_k$.

What we measured In Fig. 4.4 is the scaled compressibility of atoms in every camera pixel projected in coordinate space. Therefore, the measured compressibility is

$$\left. \frac{\partial N}{\partial \mu} \right|_i, \tag{4.22}$$

where i is the number index of camera pixels. Using Eq. (4.18), (4.20), and (4.21), one can show

$$\begin{aligned} \frac{\partial N}{\partial \mu} &= \sum_k \frac{\partial \langle n_k \rangle}{\partial \mu} \\ &= \frac{1}{k_b T} \sum_k \left(\langle n_k \rangle + \langle n_k \rangle^2 \right) \\ &= \frac{1}{k_b T} (\Delta N)^2. \end{aligned} \tag{4.23}$$

Therefore, one can that see our measured scaled compressibility is proportional to the number fluctuation, and the proportionality constant is $k_b T$. I would like to emphasize that the above derivations come from considering an ideal Bose gas model. If interactions exist in the regime close to degeneracy, the above relations will become inaccurate. The number fluctuation can be directly measured from the experiment [46]. However, those measurements require careful calibration of the imaging system and a more stringent control over experimental conditions.

The plateau in Fig. 4.4(b) ($\rho_0 \gtrsim 8$) can be understood as follows. We know that the chemical potential is defined as the energy change due to adding one particle into the system

while keeping the entropy fixed, i. e.,

$$\mu = \left.\frac{\partial E}{\partial N}\right|_s. \tag{4.24}$$

The entropy of the system is kept constant if the atom is added into the ground state, and there is only one ground state. In this case, the only energy associated with adding one particle is the interaction energy with other atoms in the ground state, i.e.,

$$\mu = n_0 u_{00} + 2\sum_{i>0} u_{i0} n_i, \tag{4.25}$$

where u_{ij} is defined in Eq. (4.11). If the temperature of the system T is much smaller than T_{BKT}, one can ignore the contribution from the second term on the right-hand side of Eq. (4.25). Then, the scaled compressibility is given by

$$\frac{\partial n}{\partial \mu} \sim \frac{1}{u_{00}}. \tag{4.26}$$

Therefore, for a pure condensate, one expects the value of the plateau in Fig. 4.4 to be $1/u_{00}$. Of course, we won't reach that value at any finite temperature. However, the plateau indicates a macroscopic population in the ground state, thus, the existence of a quasicondensate in our system.

The plateau can also be understood as the interactions suppressing the number fluctuations. Assume there are N particles confined in a 2D box, and those atoms equally occupy the lowest α states. From Eq. (4.21), one can show that the number fluctuation of the box is given by

$$\langle N^2\rangle - \langle N\rangle^2 = \langle N\rangle + \frac{\langle N\rangle^2}{\alpha}. \tag{4.27}$$

In the case of $\langle N\rangle \gg 1$ and $\alpha \sim O(1)$, one would expect the number fluctuation of the system to show a quadratic dependence on the mean number of atoms $\langle N\rangle$. However, number (or density) fluctuations require energy when interactions become important. In this case, these interactions will suppress the number (or density) fluctuation. Therefore,

the plateau indicates that the interactions in the system have become important. This also signals the existence of a quasicondensate.

Chapter 5

Analysis of focusing images

For an infinite homogenous system, the first-order correlation function is the Fourier transform of the momentum-space distribution. Thus, the inverse width of the momentum-space distribution gives the spatial extent of the coherent fraction in the system. At the temperature $T \lesssim T_{BKT}$, the first-order correlation function starts to decay algebraically instead of exponentially. In a small system like ours, the system is still pretty coherent. Therefore, one expects a sharp peak with a width of $\sim 1/R$, where R is the size of coherent part of the cloud, to appear in a momentum-space distribution, as shown in Fig. 5.1(a).

In Fig.5.2, we show the azimuthally averaged coordinate-space and momentum-space distributions side by side. These images are taken back and forth between coordinate space and momentum space to ensure that the effects of temporal drifts in the experiment are minimized. As the temperature decreases, a sharp peak emerges from the center of the momentum-space density distribution at T = 171 nK, as shown in Fig.5.2(g); however, down to this temperature, there is no obvious change in the shape of the ground-state distribution in coordinate space, as shown in Fig.5.2(a)-(c). A more peaked distribution in coordinate space appears at a lower temperature, as shown in Fig.5.2(d). The width of the peak in momentum distribution is inversely proportional to the spatial extent of coherence of the high density part of the cloud. One would expect a delta-function-like distribution for a highly coherent system at $T \ll T_{BKT}$. However, because of finite imaging resolution, we are not able to see that. Still, the width we observe from the images gives a spatial extent of

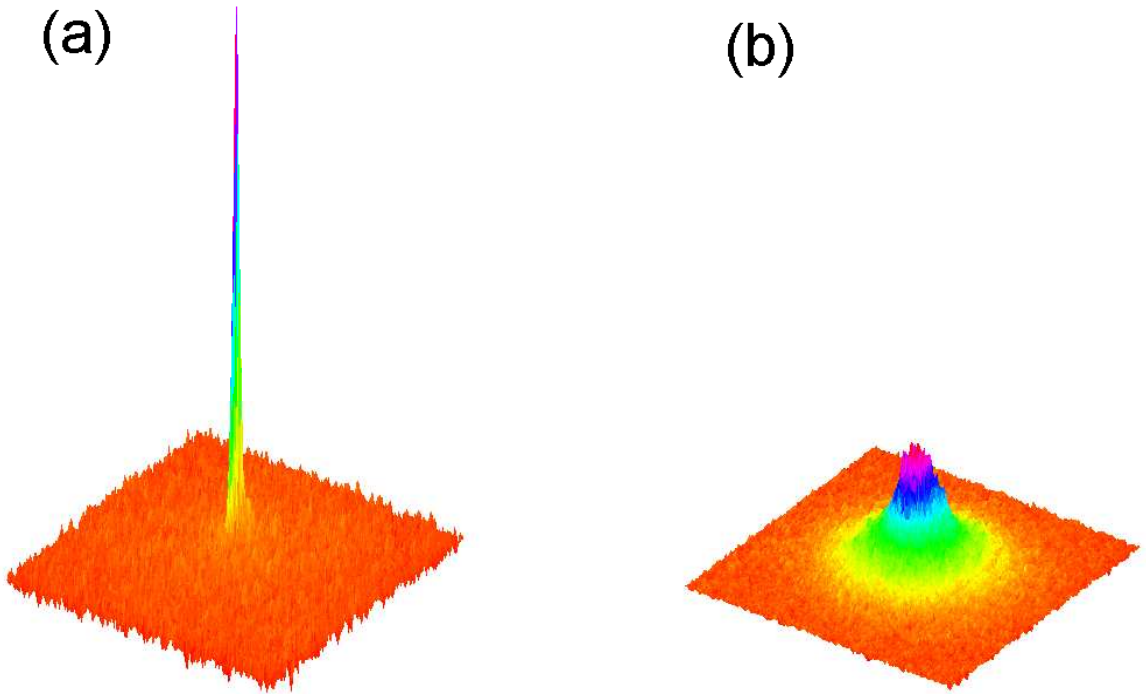

Figure 5.1: (a) The momentum-space density distribution at $T \lesssim T_{BKT}$ and (b) the in-trap density distribution under the same experimental conditions. The azimuthally averaged data of both the momentum-space and the coordinate-space distributions are shown in Fig. 5.2 (g) and 5.2 (c), respectively. At $T = T_{BKT}$, a sharp spike emerges from the center of the momentum-space distribution, signaling the appearance of a coherent fraction in the system. At $T = T_{BKT}$, there is no obvious bimodality in the coordinate-space density distribution.

coherence of about 9 μm in diameter, which is comparable to the spatial extent of the high density region in the cloud. From coordinate-space images taken under the same conditions for which the coherence spike first appears in momentum space, we determine that coherence happens when the central phase-space density ρ_0 reaches a value of 8.0(0.7) [47] (this critical value ρ_c is determined from looking at many more pairs of images than are presented in Fig. 5.2).

We emphasize that from the coordinate-space distribution alone, the identification of a transition temperature would require model-dependent analysis of the smoothly varying distribution. With access to both distributions at once, we readily see that a modest change in the central phase-space density of $< 15\%$ causes the distribution at $p = 0$ to jump by a factor of three. Unambiguous, qualitative bimodality appears only in the coordinate-space images at values of ρ_0 that are 50% higher.

5.1 Mean-field model for momentum-space distribution

Can we model momentum-space density distributions? One reasonable starting point for calculating the momentum-space density distribution is using the ideal-gas model. In this model, there is no phonon, no vortex, no mean field, and no quasicondensate. Not only is this the simplest model, but also it gives us a good estimate of the temperature because interactions have little effect on high-energy atoms. Using the semiclassical, local-density, and mean-field approximations, the number of atoms with momentum p at position r is given by

$$N(p, r) = \frac{1}{e^{(p^2/2m + m\omega_r^2 r^2/2 - \mu)/k_b T} - 1}, \tag{5.1}$$

where ω_r is the radial trapping frequency of the harmonic trap. Integrating Eq. (5.1) over the coordinate space, one then gets the momentum-space density distribution, i.e.,

$$n(p) = \frac{1}{(\lambda m \omega_r)^2} \ln\left(1 - e^{-(\frac{p^2}{2m} - \mu)/k_b T}\right). \tag{5.2}$$

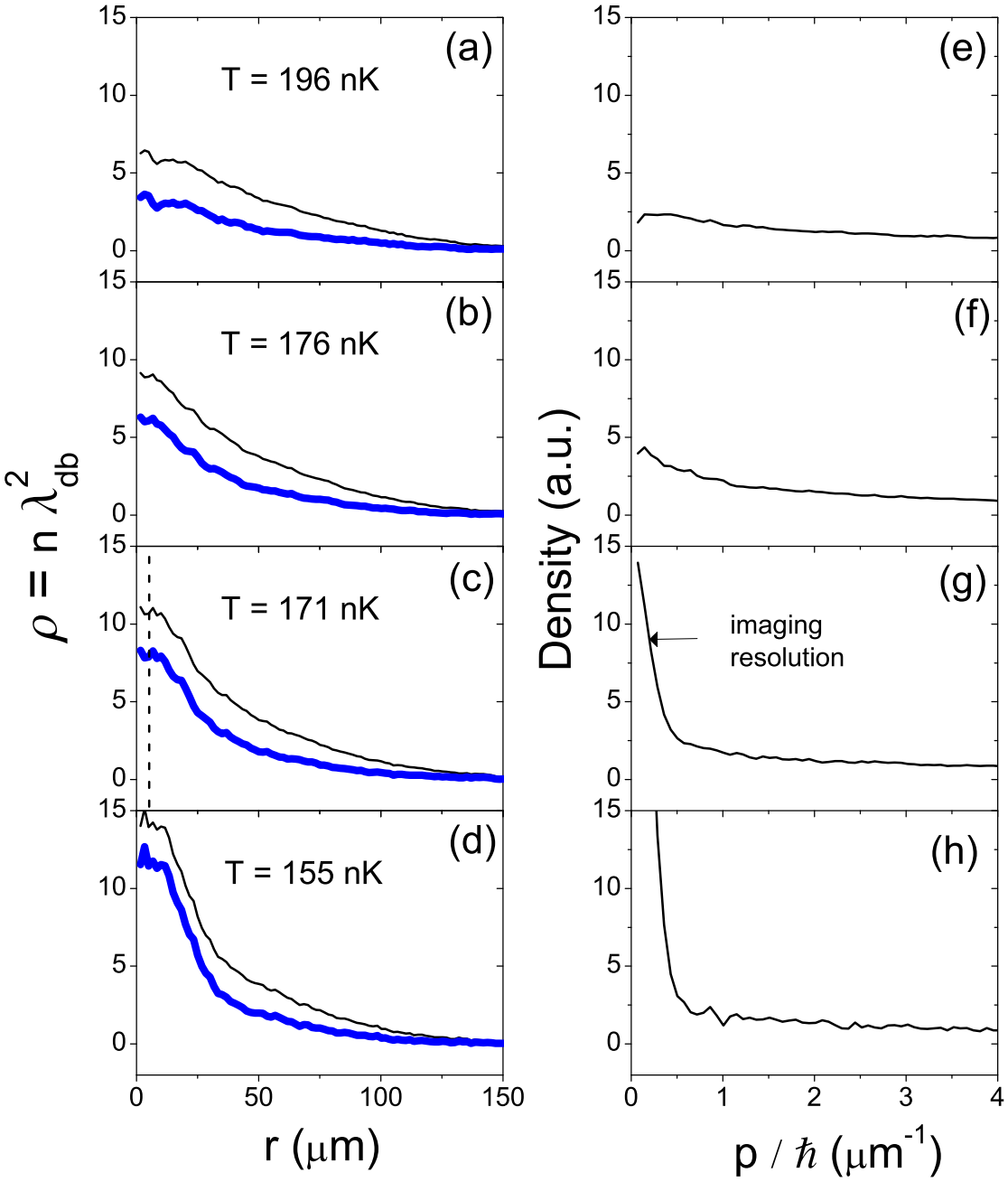

Figure 5.2: (a)-(d) Coordinate-space distributions and corresponding (e)-(h) momentum-space distributions. Two distributions in the same row are taken under near-identical conditions. The thin black curves give the azimuthal averages of n_{meas} from the raw images. The thick blue curves in the coordinate-space distributions are the ground-state distribution n_0 after correcting for $n_{k>0}$. The spike in momentum that first appears in (g) has no corresponding dramatic change in coordinate space (c). The vertical dotted line in (c) represents the inverse of the momentum resolution limit indicated in (g) and is thus a lower limit on the coherence length of the population of low-p (high-coherence) atoms represented by the area (about 1.4 % of total) under the spike in (g).

Figure 5.3 shows a fit to our data using Eq. (5.2). In the fitting routine, temperature T is the only fitting parameter. The fitting points are weighted linearly according to their distance to the center of the system. Because Eq. (5.2) does not include contributions from density-dependent mean fields, quasicondensates, or phonons, we therefore exclude the central region, $r < \sqrt{2\mu/m\omega_r^2}$, from the fitting routine.

At large r, Eq. (5.2) shows the asymptotic behavior as

$$\eta e^{\frac{\mu}{k_b T}} e^{-\frac{1}{2}m\omega_r^2 r^2}. \tag{5.3}$$

One can see in Eq. (5.3) that the OD scale η and the chemical potential μ are strongly coupled. Therefore, it is very difficult for the fitting routine to get both the correct η and the correct μ at the same time. However, one can at least get the temperature right from fitting at large r. In this case, the signal-to-noise ratio in the tail of the distribution becomes very important. We improve the precision by fixing the OD scale using independent measurements of very low T clouds in which the atoms are in a Thomas-Fermi inverted parabola with negligible noncondensed wings.

To include the mean-field contribution, I first use Eq. (4.4) to calculate the in-trap distributions for a trial set of T and μ. Once the in-trap distributions n_j are found, the total mean-field potential at the j^{th} axial level, M_j, can be calculated, which gives

$$M_j(r) = \sum_i 2u_{ij} n_i(r). \tag{5.4}$$

Then, according to Bose-Einstein statistics, the atoms with momentum p at the j^{th} level are given by

$$n_j(p) = \frac{1}{(2\pi\hbar)^2} \int_0^\infty d^2p \, \frac{1}{e^{(\frac{p^2}{2m} - \mu_j)/k_b T} - 1}, \tag{5.5}$$

where $\mu_j = \mu - \frac{1}{2}m\omega_r^2 r^2 - M_j(r)$. Considering the fact that the image is taken in coordinate space, one has to multiply the coordinates in real space by $m\omega_r$ to get the momentum coordinates. Also, one has to consider that an image is taken pixel by pixel. With these

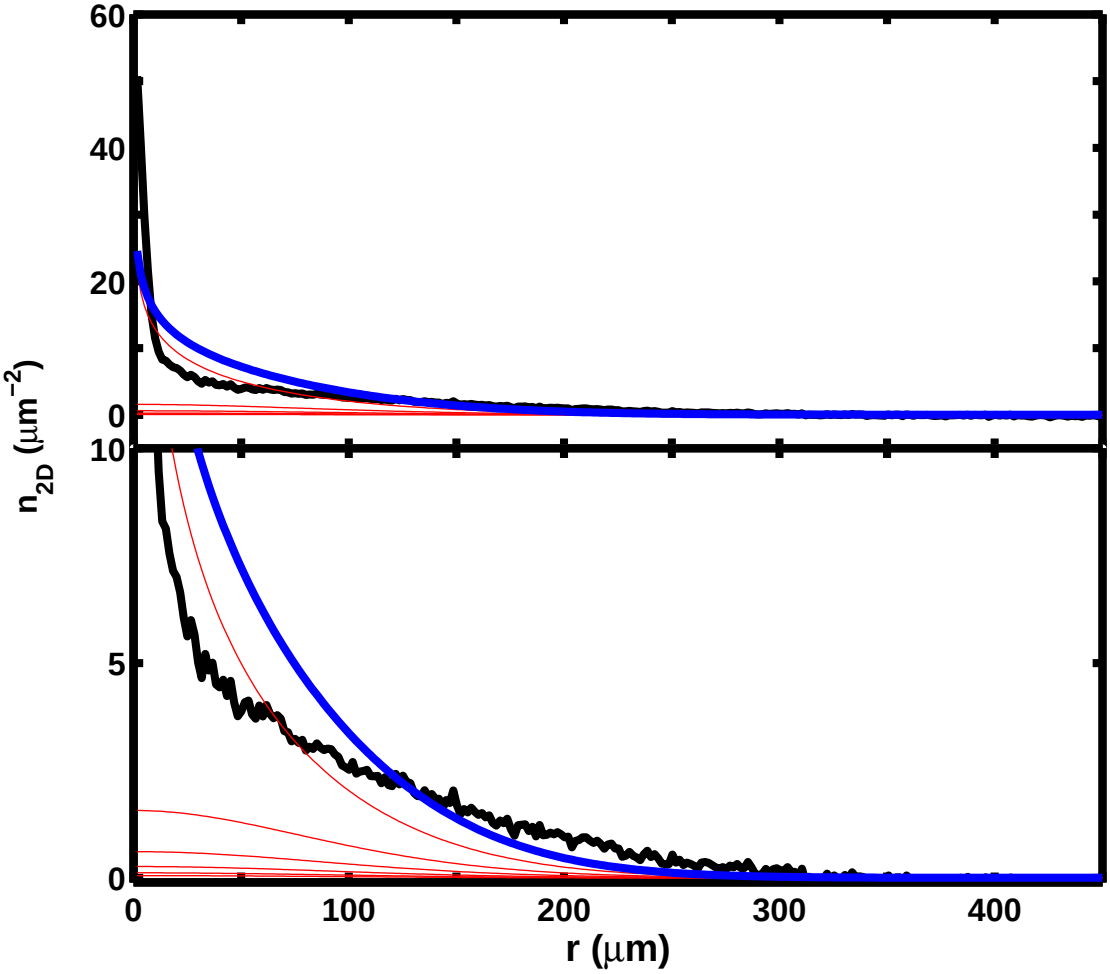

Figure 5.3: The ideal-gas model fit to the azimuthally averaged data that is shown in Fig. 5.2(g). The full-scale plot is shown in (a), while in (b), only $0 < n_{2D} < 10$ is shown to emphasize the departure of the measured data (Black curve) and the fitting curve (Blue curve). The five red curves represent $n_j(p)$ with j = 0 to 5 from top to bottom. In this fit, the chemical potential is fixed at zero, and a central area with a radius 80 μm is ignored by the fitting routine. The boundary of this ignored area indicates the highest possible momentum for a phonon in the system. The fitting curve shows a sharp peak at the center of the distribution, which comes from the distribution of the lowest axial level, $j = 0$. As one can see in the figure, the fitting is not satisfactory.

consideration, Eq. (5.5) can be written in the form of

$$n_j(p) = \frac{1}{(2\pi\hbar)^2} \sum_i \frac{1}{e^{(\frac{p^2}{2m} - (\mu - \frac{1}{2}m\omega_r^2(i\delta)^2 - M(i\delta)))/k_bT} - 1} * 2\pi i\delta^2, \tag{5.6}$$

where i is the the number index of camera pixels, and δ is the pixel size in momentum space. After summing up all the j^{th} that are populated, one can compare the resulting total momentum-space density distribution to the azimuthally averaged data pixel by pixel.

To summarize the fitting procedure, one has to (1) choose a trial set of μ, T, and OD scale; (2) find a consistent solution for $n_j(r)$; (3) from $n_j(r)$, calculate $M(r)$; (4) once $M(r)$ is found, calculate the j^{th}-level momentum-space distribution; (5) summing contributions from all j levels, compare the resulting value to the data and calculate the total deviation-square value, and (6) stop the routine if a stable minimum of the total deviation-square value is found; otherwise return to step 1.

Figure 5.4 shows the fit to a focusing image. As one can see from Fig. 5.4(b), the two curves from the data and the mean-field model start to resolve at the momentum which corresponds to the chemical potential. Since the mean-field model does not include any phonon contribution, this deviation is understandable. Although this mean-field model in momentum space can not account for contributions from phonons and vortices, this model gives an accurate description on the nondegenerate part of the system. This part of the system is what we are least interested in. However, by subtracting the mean-field model curve from a measured momentum-space density distribution, one can obtain the part in an image that is beyond the mean-field description. For an image taken at $T \lesssim T_{BKT}$, the residual distribution has a Gaussian-like shape. This residual density distribution includes the contribution from a quasicondensate as well as atoms in the fluctuating region, as shown in Fig. 5.5. We then fit the residual distribution to a Gaussian, and determine the extent of the coherence by the inverse of the fitted-Gaussian width. Considering the broadening from imaging errors to the measured density distribution, the measured width of the sharp spike in the density distribution is overestimated. Therefore, the broadened width sets the lower

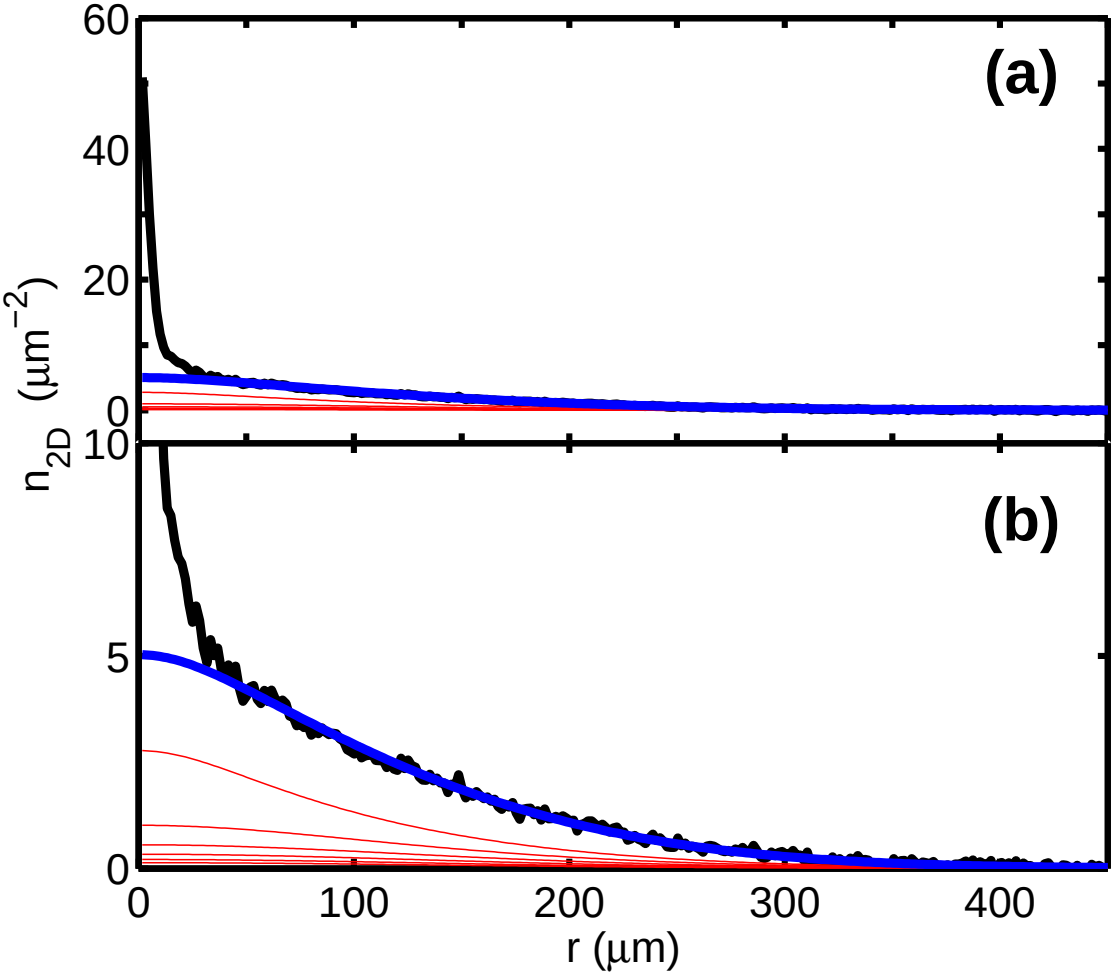

Figure 5.4: The mean-field model fit to the azimuthally averaged data shown in Fig. 5.2(g). In the fitting routine, chemical potential μ and temperature T are the fit parameters. The full-scale plot is shown in (a), while in (b), only $0 < n_{2D} < 10$ is shown to emphasize the departure of the measured data (black curve) and the fitting curve (blue curve). The five red curves represent $n_j(p)$ with j = 0 to 5 from top to bottom. One can see the sharp central peak in the fitting curve of Fig. 5.3 is suppressed by mean fields. After including mean-field contributions, the fit is now satisfactory.

bound of the real spatial extent of coherence. Considering our imaging resolution, the minimum detectable width of a Gaussian distribution in momentum space implies that coherence extends over a central disk of radius 4.5 μm. Figure 5.6 shows the fitting temperatures of several focusing images. The temperatures from fitting momentum-space images shows a good agreement with the temperatures obtained from fitting of *in-situ* images, of course, as one expects.

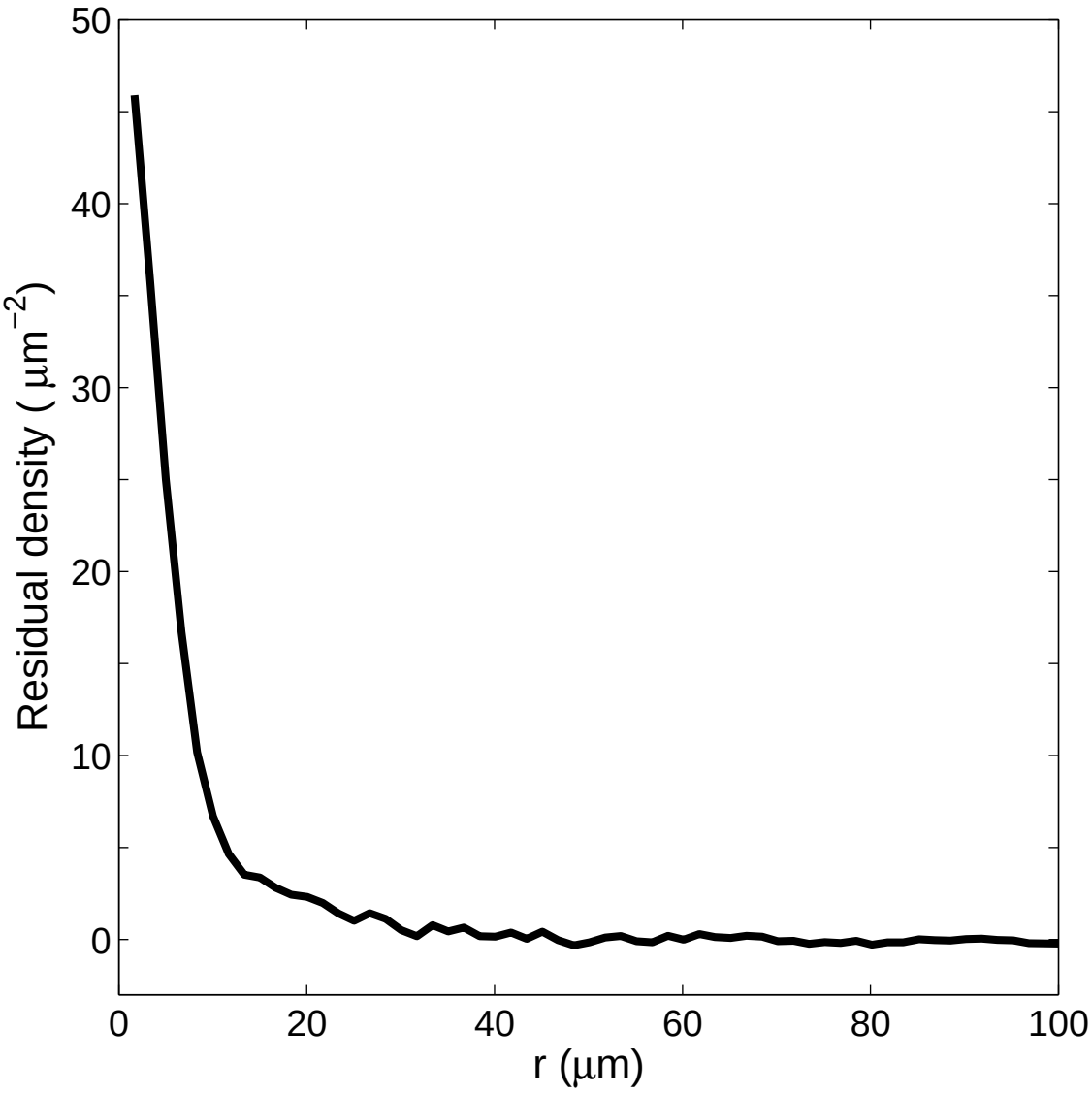

Figure 5.5: Residual density distribution. The density distribution is obtained by subtracting the mean-field model fit (blue line) from the measured density distribution (black line) in Fig. 5.4. The distribution includes the atoms that are beyond mean-field description. The width of the distribution is limited by the imaging resolution, not by the coherence of the system.

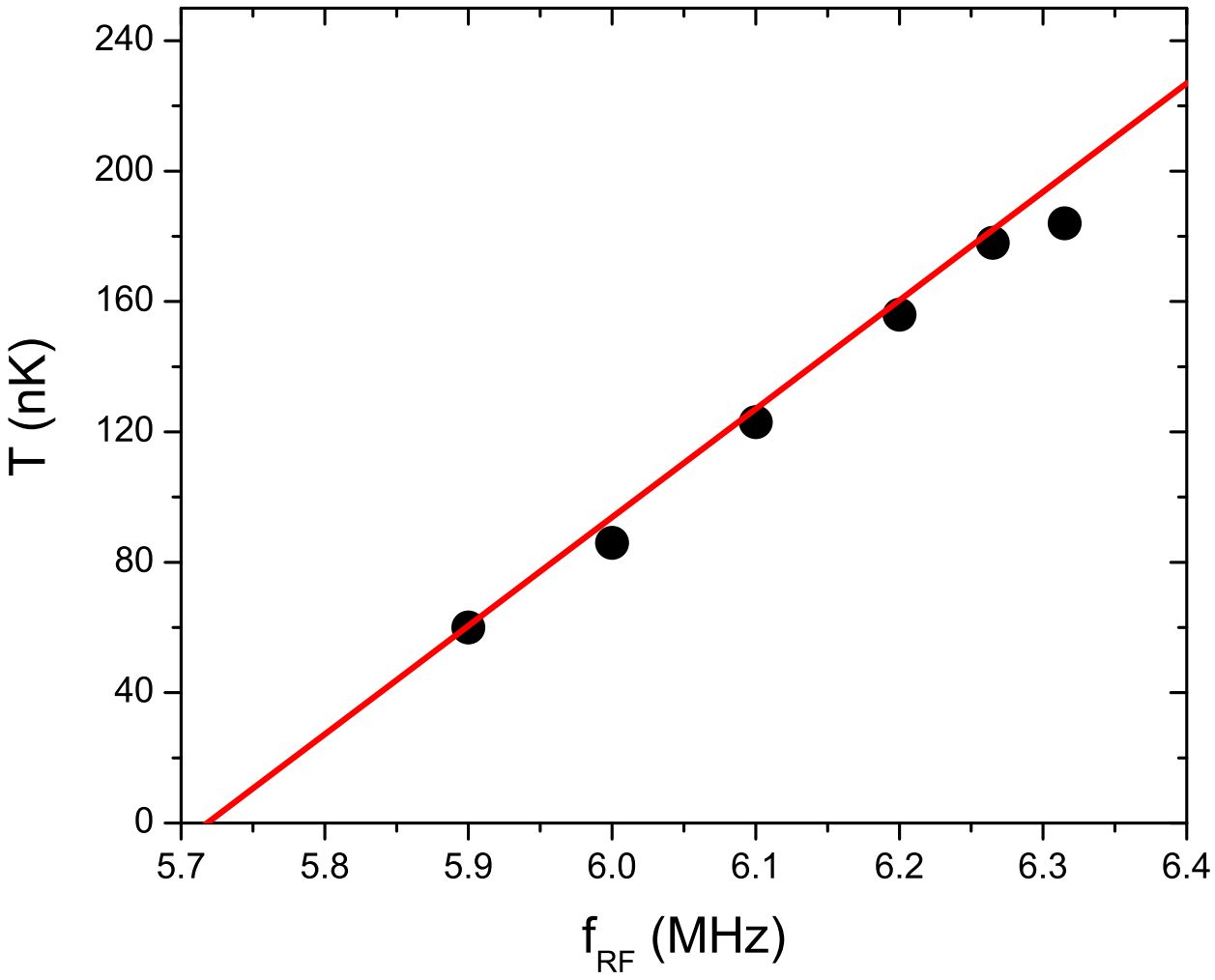

Figure 5.6: Temperatures obtained from fitting focusing images vs final rf-knife frequency. The temperatures fit by the mean-field model in momentum space show a good agreement with the temperature obtained from fitting *in-situ* images in coordinate space. The red line comes from the fitting of the temperatures shown in Fig. 3.4

Chapter 6

Conclusion and outlook

6.1 Conclusion

In Fig. 4.4, we see that the deviation of the measured scaled compressibility κ from the mean-field predicted value κ_{nc} starts at a phase-space density of $\rho_0 \sim 3$. From Fig. 5.2, we see that the long coherence does not appear in an atomic cloud until $\kappa/\kappa_{nc} = 1.7$, or the phase-space density $\rho_0 = 8$. When $3 < \rho_0 < 8$, a very interesting regime is identified. A 2D Bose gas in this regime is beyond the mean-field description, but it does not yet possess a coherent fraction, or quasicondensate. This regime, which does not exist in three dimensions, is a product of the enhanced interactions associated with reduced dimensionality. The appearance of a long coherence in a 2D Bose gas starts at $\rho = 8(0.7)$, which is in a very good agreement with the prediction of the BKT transition from the Monte-Carlo simulation [15].

We tried very hard to present our data in a model-free fashion. Of course, there are assumptions in our analyses. We assumed that the semiclassical, mean-field, and local-density approximations are good for describing the atomic populations in the axial-excited states. We don't assume any model for the ground-state population. Nor as we assume the phase-space density at which the BKT transition occurs. All our measurements are done locally, pixel by pixel. We do not measure global quantities, e.g., the critical number N_c of the system for the BKT transition. I would like to emphasize that the goal of our measurements

was not to prove the existence of the BKT transition in a 2D system, which had already been proven first in 2D systems [48, 49, 50] and then in a 2D ultracold-atom system [9]. Our goal for the experiment described in this thesis was to provide better measurements to compare with theory.

6.2 Outlook

How interactions participate in the statistical behavior of a many-body system is always an interesting topic. In lower dimensional systems, enhanced interactions come from reduced dimensionality. In an extreme 2D case, the microscopic collision behavior of atoms will be also influenced by reduced dimensionality. These properties make a 2D ultracold-atom system an extremely interesting playground for physicists. I think there are still many interesting experiments to be done and many interesting questions to be answered. From my perspective, I list some of these experiments and questions here.

(1) The first possible extension of this work would be to go to a more strongerly interacting regime, where $\tilde{g} \gtrsim 1$. In this regime the interaction between atoms is so large that any quasicondensate would be seriously depleted. How the quasicondensate becomes depleted as a function of $\tilde{g}$ is an interesting question.

(2) The second possible extension would be to measure directly the first-order correlation at a temperature $T < T_{BKT}$. The theory tells us the first-order correlation function has an algebraic decay on the separation between two points in the system. Can we measure it? How does the decay change as a function of temperature? How does the finite-size effect influence the first-order correlation function?

(3) How does a 2D quasicondensate establish its phase coherence? By controlling how quickly the system enters the BKT regime, one can study couple interesting questions: How much time does the system need to establish its coherence? How many

excitations will this process induce into the system as a function of the ramping speed?

(4) What are the properties of a vortex state in a 2D system? A vortex lattice should be melted by the increasing effect of thermal fluctuations. Can one see the melting process? How does a vortex lattice melt? There are also predictions that at an extremely high rotation rate and at extremely low temperature, the system will show a quantum Hall-like behaviors. Can we realize this regime?

Bibliography

[1] Both appendix A and B have already appeared in print in *Phys. Rev. Lett* .

[2] S. Tung, V. Schweikhard, and E. A. Cornell, Observation of vortex pinning in Bose-Einstein condensates, *Phys. Rev. Lett.* **97**, 240402 (2006).

[3] V. Schweikhard, S. Tung, and E. A. Cornell, Vortex proliferation in the Berezinskii-Kosterlitz-Thouless regime on a two-dimensional lattice of Bose-Einstein condensates, *Phys. Rev. Lett.* **99**, 030401 (2007).

[4] V. Schweikhard, I. Coddington, P. Engels, S. Tung, and E. A. Cornell, Vortex-lattice dynamics in rotating spinor Bose-Einstein condensates, *Phys. Rev. Lett.* **93**, 210403 (2004).

[5] I. Coddington, P. C. Haljan, P. Engels, V. Schweikhard, S. Tung, and E. A. Cornell, Experimental studies of the equilibrium vortex properties in Bose-condensed gas, *Phys. Rev. A* **70**, 063607 (2004).

[6] V. L. Berezinskii, Destruction of long-range order in one-dimensional and two-dimensional system possessing a continuous symmetry group-II Quantum systems, *Soviet Physics JETP* **34**, 610 (1971).

[7] J. Kosterlitz, and D. J. Thouless, Ordering, metastability and phase transitions in two dimensional systems, *J. Phys. C: Solid State Physics* **6**, 1181 (1973).

[8] Z. Hadzibabic, S. Stock, B. Battelier, V. Bretin, and J. Dalibard, Interference of an array of independent bose-einstein condensates, *Phys. Rev. Lett.* **93**, 180403 (2004).

[9] Z. Hadzibabic, P. Krüger, M. Cheneau, B. Battelier, and J. Dalibard, Berezinskii-kosterlitz-thouless crossover in a trapped atomic gas, *Nature* **441**, 1118 (2006).

[10] Z. Hadzibabic, P. Krüger, M. Cheneau, S. P. Rath, and J. Dalibard, The trapped two-dimensional bose gas: from Bose-Einstein condensation to Berezinskii-Kosterlitz-Thouless physics, *New J of Phys* **10**, 045006 (2008).

[11] I. Shvarchuck, C. Buggle, D. S. Petrov, K. Dieckmann, M. Zielonkoski, M. Kemmann, T. G. Tiecke, W. von Klitzing, G. V. Shlyapnikov, and J. T. M. Walraven, Bose-Einstein condensation into nonequilibrium states studied by condensate focusing, *Phys. Rev. Lett.* **89**, 270404 (2002).

[12] A. H. van Amerongen, J. J. van Es, P. Wicke, K. V. Kheruntsyan, and N. J. van Druten, Yang-Yang thermodynamics on an atom chip, *Phys. Rev. Lett.* **100**, 090402 (2008).

[13] P. Krüger, Z. Hadzibabic, and J. Dalibard, Critical point of an interacting two-dimensional atomic bose gas, *Phys. Rev. Lett.* **99**, 040402 (2007).

[14] P. Cladé, C. Ryu, A. Ramanathan, K. Helmerson, and W. D. Phillips, Observation of a 2D bose gas: From thermal to quasicondensate to superfluid, *Phys. Rev. Lett.* **102**, 170401 (2009).

[15] N. V. Prokofév, O. Ruebenacker, and B. V. Svistunov, Critical point of a weakly interacting two-dimensional Bose gas, *Phys. Rev. Lett.* **87**, 270402 (2001).

[16] V. Schweikhard, Ultracold Bose gases under rotation, in lattice potentials, and both, Ph.D. thesis, University of Colorado at Boulder (2008).

[17] C. J. Pethick, and H. Smith, *Bose-Einstein condensation in dilute gases* (Cambridge university press, Cambridge, 2002).

[18] R. E. Peierls, Quelques propriétés typiques des corps solides, *Ann. Inst. Henri Poincaré* **5**, 177 (1935).

[19] N. D. Mermin, and H. Wagner, Absence of ferromagnetism or antiferromagnetism in one- or two-dimensional isotropic Heisenberg models, *Phys. Rev. Lett.* **17**, 1307 (1966).

[20] P. C. Hohenberg, Existence of long-range order in one and two dimensions, *Phys. Rev.* **158**, 383 (1967).

[21] O. Penrose, and L. Onsager, Bose-Einstein condensation and liquid Helium, *Phys. Rev.* **104**, 576 (1956).

[22] L. Pitaveskii, and S. Stringari, *Bose-Einstein condensation* (Oxford university press, Oxford, 2003).

[23] M. Naraschewski, and R. J. Glauber, Spatial coherence and density correlations of trapped Bose gases, *Phys. Rev. A* **59**, 4595 (1999).

[24] G. B. Arfken, and H. J. Webber, *Mathematical methods for physicists* (Academic press, MA, USA, 2005).

[25] I. Bouchoule, N. J. van Druten, and C. I. Westbrook, Atoms chips and one-dimensioanl bose gases, *ArXiv:0901.3303* .

[26] D. S. Petrov, M. Holzmann, and G. V. Shlyapnikov, Bose-Einstein condensation in quasi-2D trapped gases, *Phys. Rev. Lett.* **84**, 2551 (2000).

[27] D. S. Petrov, D. M. Gangardt, and G. V. Shlyapnikov, Low-dimensional trapped gases, *J. Phys. IV* **116**, 5 (2004).

[28] Z. Hadzibabic, and J. Dalibard, Two dimensional bose fluids: An atomic physics perspective, *ArXiv:0912.1490* .

[29] J. W. Kane, and L. P. Kadanoff, Long-range order in superfluid Helium, *Phys. Rev.* **155**, 80 (1967).

[30] A. Gölitz, J. M. Vogels, A. E. Leanhardt, C. Raman, T. L. Gustavson, J. R. Abo-Shaeer, A. P. Chikkatur, S. Gupta, S. Inouye, T. Rosenband, and W. Ketterle, Realization of Bose-Einstein condensates in lower dimensions., *Phys. Rev. Lett.* **87**, 130402 (2001).

[31] S. Stock, Z. Hadzibabic, B. Battelier, M. Cheneau, and J. Dalibard, Observation of phase defects in quasi-two-dimensional Bose-Einstein condensates, *Phys. Rev. Lett.* **95**, 190403 (2005).

[32] S. P. Rath, T. Yefsah, K. J. Günter, M. Cheneau, R. Desbuquois, M. Holzmann, W. Krauth, and J. Dalibard, Equilibrium state of a trapped two-dimensional Bose gas, *Phys. Rev. A* **82**, 013609 (2010).

[33] E. A. A. Polkovnikov, and E. Demler, Interference between independent fluctuating condensates, *Proc. Natl. Acad. Sci. USA* **103**, 6125 (2006).

[34] M. Greiner, O. Mandel, T. Esslinger, T. W. Hänsch, and I. Bloch, Quantum phase transition from a superfluid to a Mott insulator in a gas of ultracold atoms, *Nature* **415**, 39 (2002).

[35] R. Grimm, and M. Weidemüller, Optical dipole traps for neutral atoms, *Adv. At. Mol. Opt. Phys.* **42**, 95 (2000).

[36] W. Petrich, M. H. Anderson, J. R. Ensher, and E. A. Cornell, Stable, tightly confining magnetic trap for evaporative cooling of neutral atoms, *Phys. Rev. Lett.* **74**, 3352 (1995).

[37] M. H. Anderson, J. R. Ensher, M. R. Matthews, C. E. Wieman, and E. A. Cornell, Observation of Bose-Einstin condensation in a dilute atomic vapor, *Science* **269**, 198 (1995).

[38] J. R. Ensher, The first experiments with Bose-Einstein condensation of ^{87}Rb, Ph.D. thesis, University of Colorado at Boulder (1998).

[39] I. R. Coddington, Vortices in a highly rotating bose-condensed gas, Ph.D. thesis, University of Colorado at Boulder (2004).

[40] H. J. Metcalf, and P. van der Straten, *Laser cooling and trapping* (Springer-Verlag, New York, 1999).

[41] In our experiment, $l_z/a_s \sim 60$.

[42] L. D. Landau, and E. M. Lifshitz, *Statistical physics, part 1* (Butterworth-Heinemann, Oxford, 1976), third edn.

[43] K. Huang, *Statistical mechanics* (Jonh Wiley & Sons, Inc, New York, 1987).

[44] M. Schellekens, R. Hoppeler, A. Perrin, J. V. Gomes, D. Boiron, A. Aspect, and C. I. Westbrook, Hanbury Brown Twiss effect for ultracold quantum gases, *Science* **310**, 648 (2005).

[45] T. Jeltes, J. M. McNamara, W. Hogervorst, W. Vassen, V. Krachmalnicoff, M. Schellekens, A. Perrin, H. Chang, D. Boiron, A. Aspect, and C. I. Westbrook, Comparison of the Hanbury BrownTwiss effect for bosons and fermions, *Nature* **445**, 402 (2007).

[46] In the preparation of this thesis, I learned that Cheng Chin's group at University of Chicago were studying universal behavior of a 2D Bose gas. In their experiment, they measured the number fluctuation directly from the noise of their images. .

[47] Our observed value $\rho_c = 8.0(0.7)$ is consistent with predictions from [15], which give $\rho_c = 8.3$. our observation that $\kappa/\kappa_{nc} = 1.7$ at $\rho_0 = \rho_c$ could be compared to theory via e.g. the slopes of lines in fig. 3 in ref. [28] .

[48] G. Agnolet, D. F. McQueeney, and J. D. Reppy, Kosterlitz-Thouless transition in helium films, *Phys. Rev. B* **39**, 8934 (1989).

[49] A. I. Safonov, S. A. Vasilyev, I. S. Yasnikov, I. I. Lukashevich, and S. Jaakkola, Observation of quasicondensate in two-dimensional atomic hydrogen, *Phys. Rev. Lett.* **81**, 4545 (1998).

[50] D. Resnick, J. C. Garland, J. T. Boyd, S. Shoemaker, and R. S. Newrock, Kosterlitz-Thouless transition in proximity-coupled superconducting arrays, *Phys. Rev. Lett.* **47**, 1542 (1981).

[51] D. S. Petrov, G. V. Shlyapnikov, and J. T. M. Walraven, Phase-fluctuating 3D Bose-Einstein condensates in elongated traps, *Phys. Rev. Lett.* **87**, 050404 (2001).

[52] T. Kinoshita, T. Wenger, and D. S. Weiss, Observation of a one-dimensional Tonks-Girardeau gas, *Science* **305**, 1125 (2004).

[53] T. Stöferle, H. Moritz, C. Schori, M. Köhl, and T. Esslinger, Transition from a strongly interacting 1d superfluid to a Mott insulator, *Phys. Rev. Lett.* **92**, 130403 (2004).

[54] K. W. Madison, F. Chevy, W. Wohlleben, and J. Dalibard, Vortex formation in a stirred bose-einstein condensate, *Phys. Rev. Lett.* **84**, 806 (2000).

[55] V. Schweikhard, I. Coddington, P. Engels, V. P. Mogendorff, and E. A. Cornell, Rapidly rotating Bose-Einstein condensates in and near the lowest landau level, *Phys. Rev. Lett.* **92**, 040404 (2004).

[56] J. R. Abo-Shaeer, C. Raman, J. M. Vogels, and W. Ketterle, Observation of vortex lattices in Bose-Einstein condensates, *Science* **292**, 476 (2001).

[57] N. R. Cooper, N. K. Wilkin, and J. M. F. Gunn, *Phys. Rev. Lett.* **87**, 120405 (2001).

[58] D. Jaksch, C. Bruder, J. I. Cirac, C. W. Gardiner, and P. Zoller, *Phys. Rev. Lett.* **81**, 3108 (1998).

[59] P. W. Stephens, P. A. Heiney, R. J. Birgeneau, P. M. Horn, D. E. Moncton, and G. S. Brown, High-resolution x-ray-scattering study of the commensurate-incommensurate transition of monolayer kr on graphite, *Phys. Rev. B* **29**, 3512 (1984).

[60] P. Bak, Commensurate phases, incommensurate phases and the devil's staircase, *Rep. Prog. Phys.* **45**, 587 (1982).

[61] T. Goto, T. Kimura, G. Lawes, A. P. Ramirez, and Y. Tokura, Ferroelectricity and giant magnetocapacitance in perovskite rare-earth manganites, *Phys. Rev. Lett.* **92**, 257201 (2004).

[62] M. Baert, V. V. Metlushko, R. Jonckheere, V. V. Moshchalkov, and Y. Bruynseraede, Composite flux-line lattices stabilized in superconducting films by a regular array of artificial defects, *Phys. Rev. Lett.* **74**, 3269 (1995).

[63] A. N. Grigorenko, S. J. Bending, M. J. V. Bael, M. Lange, V. V. Moshchalkov, H. Fangohr, and P. A. J. de Groot, Symmetry locking and commensurate vortex domain formation in periodic pinning arrays, *Phys. Rev. Lett.* **90**, 237001 (2003).

[64] J. E. Villegas, S. Savel'ev, F. Nori, E. M. Gonzalez, J. V. Anguita, R. Garcia, and J. L. Vicent, A superconducting reversible rectifier that controls the motion of magnetic flux quanta, *science* **3025**, 1188 (2003).

[65] C. Reichhardt, C. J. Olson, R. T. Scalettar, and G. T. Zimányi, Commensurate and incommensurate vortex lattice melting in periodic pinning arrays, *Phys. Rev. B* **64**, 144509 (2001).

[66] J. W. Reijnders, and R. A. Duine, Pinning of vortices in a bose-einstein condensate by an optical lattice, *Phys. Rev. Lett.* **93**, 060401 (2004).

[67] H. Pu, L. O. Baksmaty, S. Yi, and N. P. Bigelow, Structural phase transitions of vortex matter in an optical lattice, *Phys. Rev. Lett.* **94**, 190401 (2005).

[68] C. Wu, H. D. Chen, J. P. Hu, and S. C. Zhang, Vortex configurations of bosons in an optical lattice, *Phys. Rev. A* **69**, 043609 (2004).

[69] R. Bhat, L. D. Carr, and M. J. Holland, Bose-Einstein condensates in rotating lattices, *Phys. Rev. Lett.* **96**, 060405 (2006).

[70] Mask (b): ϕ_1= 2.5 mm and d_1= 11.5 mm. The lattice constant of the triangular optical lattice is 7.8 μm, giving ω_c= 0.806 ω_r.; mask (c): ϕ_2 = 2.5 mm and d_2= 13.5 mm. The lattice constant of the square lattice is 7.0 μm, giving ω_c= 0.866 ωr. The focal lens of two lenses are 300 mm and 250 mm, respectively. .

[71] I. Coddington, P. C. Haljan, P. Engels, V. Schweikhard, S. Tung, and E. A. Cornell, Experimental studies of equilibrium vortex properties in a bose-condensed gas, *Phys. Rev. A* **70**, 063607 (2004).

[72] D. E. Sheehy, and L. Radzihovsky, Vortex lattice inhomogeneity in spatially inhomogeneous superfluids, *Phys. Rev. A* **70**, 051602 (2004).

[73] The chemical potential is determined from the axial Thomas-Fermi radius of the condensate obtained from in-trap images, and is proportional to the peak density of the condensate .

[74] There is a constant measurement offset to the values of $\theta_{OL} - \theta_{VL}$ in this data set. we have used in-trap images of vortex lattices to confirm that the absolute value of $\theta_{OL} - \theta_{VL}$ is zero for locked lattices .

[75] $|s(k_{sq})|$=a_2+$\frac{A_1-A_2}{1+Exp[\frac{U-U_0}{\delta U}]}$; A_1, A_2, U_0, and δU are fit to the data. .

[76] L. J. Campbell, M. M. Doria, and J. B. Kadtke, Energy of infinite vortex lattices, *Phys. Rev. A* **39**, 5436 (1989).

[77] A. Leggett, Bose-Einstein condensation in the alkali gases: Some fundamental concepts, *Rev. Mod. Phys.* **73**, 307 (2001).

[78] D. Jaksch, C. Bruder, J. I. Cirac, C. W. Gardiner, and P. Zoller, Cold bosonic atoms in optical lattices, *Phys. Rev. Lett.* **81**, 003108 (1998).

[79] S. Richardr, F. Gerbier, J. H. Thywissen, M. Hugbart, P. Bouyer, and A. Aspect, Momentum spectroscopy of 1d phase fluctuations in Bose-Einstein condensates, *Phys. Rev. Lett.* **91**, 010405 (2003).

[80] D. Hellweg, L. Cacciapuoti, M. Kottke, T. Schulte, K. Sengstock, W. Ertmer, and J. J. Arlt, Measurement of the spatial correlation function of phase fluctuating bose-einstein condensates, *Phys. Rev. Lett.* **91**, 010406 (2003).

[81] R. Gati, B. Hemmerling, J. Fölling, M. Albiez, and M. K. Oberthaler, Noise thermometry with two weakly coupled Bose-Einstein condensates, *Phys. Rev. Lett.* **96**, 130404 (2006).

[82] M. Tinkham, *Introduction to Superconductivity* (McGraw-Hill, Inc., New York, 1996).

[83] Within a dataset, the ramp-down rate is kept fixed, $t_r = \tau \times v_{OL}/1.3\,kHz$, $\tau = 18\,ms$, if not otherwise indicated .

[84] T. Simula, and P. Blakie, Thermal activation of vortex-antivortex pairs in quasi-two-dimensional Bose-Einstein condensates, *Phys. Rev. Lett.* **96**, 020404 (2006).

[85] A. Trombettoni, A. Smerzi, and P. Sodano, Observable signature of the Berezinskii-Kosterlitz-Thouless transition in a planar lattice of Bose-Einstein condensates, *New J. Phys.* **7**, 57 (2005).

[86] Three circularly polarized laser beams ($\lambda = 810$ nm) intersect in a tripodlike configuration, with $\theta = 6.6^\circ$ angles to the z-axis. Calculation of the optical dipole potential [35] includes counterrotating terms and interaction with both the d1 and d2 lines, as well as the fictitious magnetic field due to the circular polarization. The tilted bias field of the TOP trap makes $\mathcal{P} \approx 0.5$[35] .

[87] J. Javanainen, Phonon approach to an array of traps containing Bose-Einstein condensates, *Phys. Rev. A* **60**, 4902 (1999).

[88] K. Burnett, M. Edwards, C. W. Clark, and M. Shotter, The Bogoliubov approach to number squeezing of atoms in an optical lattice, *J. Phys. B* **35**, 1671 (2002).

[89] To avoid radial flows during v_{OL} ramp-up, r_{TF} is kept constant by balancing the lattice-enhanced mean-field pressure with radial confinement due to the optical lattice envelope, by the choice of a $67\mu m$ $1/e^2$ intensity waist. Axial (z) confinement is due to the magnetic trap alone .

[90] In the axial condensate region between $z = -r_z/3, +r_z/3$, where according to our 3D GPE simulations 85% of the tunnel current is localized and hence the relative phase is measured, axial phase fluctuations [51] vary between $\approx 600\,mrad$ ("cold" data in Fig. B) and $800\,mrad$ ("hot") in the regime $j/t \approx 1$.

[91] j is averaged over junctions within the central 11% of the array area, from which all quantitative experimental results are extracted. .

[92] D. Ananikian, and T. Bergeman, Gross-Pitaevskii equation for Bose particles in a double-well potential: Two-mode models and beyond, *Phys. Rev. A* **73**, 013604 (2006).

[93] M. Naraschewski, and D. Stamper-Kurn, Analytical description of a trapped semi-ideal Bose gas at finite temperature, *Phys. Rev. A* **58**, 2423 (1998).

[94] Following [37], in simulations we count a vortex if all three phase differences in an elemental triangle of junctions are $\in (0, \pi)$, or if all are $\in (-\pi, 0)$.

[95] The very short annihilation time of configuration i pairs [$\tau < 5\,ms$ in fig. B(c)] is not unexpected: their spacing $d/\sqrt{3} = 2.8\,\mu m$ is comparable to the diameter of a vortexcore in the bulk condensate (after v_{OL} rampdown) .

[96] L. Pitaevskii, and S. Stringari, Thermal vs quantum decoherence in double well trapped Bose-Einstein condensates, *Phys. Rev. Lett.* **87**, 180402 (2001).

Appendix A

Observation of vortex pinning in Bose-Einstein condensates [1, 2]

We report the observation of vortex pinning in rotating gaseous Bose-Einstein condensates (BEC). Vortices are pinned to columnar pinning sites created by a co-rotating optical lattice superimposed on the rotating BEC. We study the effects of two types of optical lattice, triangular and square. In both geometries we see an orientation locking between the vortex and the optical lattices. At sufficient intensity the square optical lattice induces a structural cross-over in the vortex lattice.

Some of the most appealing results from recent work in superfluid gases have had to do with lattices, either optical lattices [34, 52, 53] or vortex lattices [54, 55, 56]. These two kinds of lattices could hardly be more different! The former is an externally imposed periodic potential arising from the interference of laser beams, while the latter is the self-organized natural response of a superfluid to rotation. As distinct as these two periodic structures may be, there are reasons for trying to marry them in the same experiment. For one thing, the extreme limits of rapid rotation (in the case of vortex lattices) [57] and deep potentials (in the case of optical lattices) [58] both lead to the same thing: correlated many-body states. For another, there is considerable precedent, from various subdisciplines of physics, for interesting effects arising from the interplay between competing lattices [59, 60, 61]. Moreover, the pinning of superconducting flux vortices to an array of pinning sites in solids is an area of very active research as well [62, 63, 64, 65]. With these considerations in mind, we undertook a preliminary experimental study of the effects of a rotating optical lattice

on a vortex lattice in a Bose-condensed sample of ^{87}Rb. The density of the superfluid is suppressed at the antinodes of the two-dimensional standing wave pattern of the optical lattice. These antinodes then become pinning sites, regions of low potential energy, for the superfluid vortices. Vortices can lower their interaction energy by arranging themselves to be as far apart as possible from one another. The competition between these effects has been examined in several theoretical works [66, 67]. Also [68, 69] discuss similar systems in the strong interacting region

The setup for creating a rotating optical lattice is shown in Fig. A.1(a). A mask with a set of holes is mounted onto a motor-driven rotary stage, and a laser beam (532 nm) is expanded, collimated, and passed through the mask. After the mask the resulting three beams are focused onto the BEC. The interference pattern at the focus constructs a quasi-2D optical lattice. The geometry and spatial extent of the triangular or the square optical lattice is determined by the size and layout of the holes and the focal length of the second lens. For the pinning sites to appear static in the frame of a rotating BEC, the rotation of the two lattices must be concentric, and mechanical instabilities and optical aberrations (which lead to epicyclic motion of the pinning sites) must be particularly minimized. Even so, residual undesired motion is such that the strength of the optical lattice must be kept at less than 30% of the condensate's chemical potential or unacceptable heating results over the experiment duration of tens of seconds. We work perforce in the weak pinning regime.

The experiments begin with condensates containing $\sim 3 \times 10^6$ ^{87}Rb atoms, held in the Zeeman state $|F = 1, m_f = -1\rangle$ by an axial symmetric magnetic trap with trapping frequencies $\{\omega_r, \omega_z\} = 2\pi\{8.5, 5.5\}$Hz. Before the optical lattice, rotating at angular frequency Ω_{OL}, is ramped on, the BEC is spun up [55] close to Ω_{OL}. This leads, before application of an optical lattice, to the formation of a near perfect triangular vortex lattice with a random initial angular orientation in inertial space. Through dissipation a vortex lattice can come to equilibrium with an optical lattice, with their rotation rates and angular orientations locked.

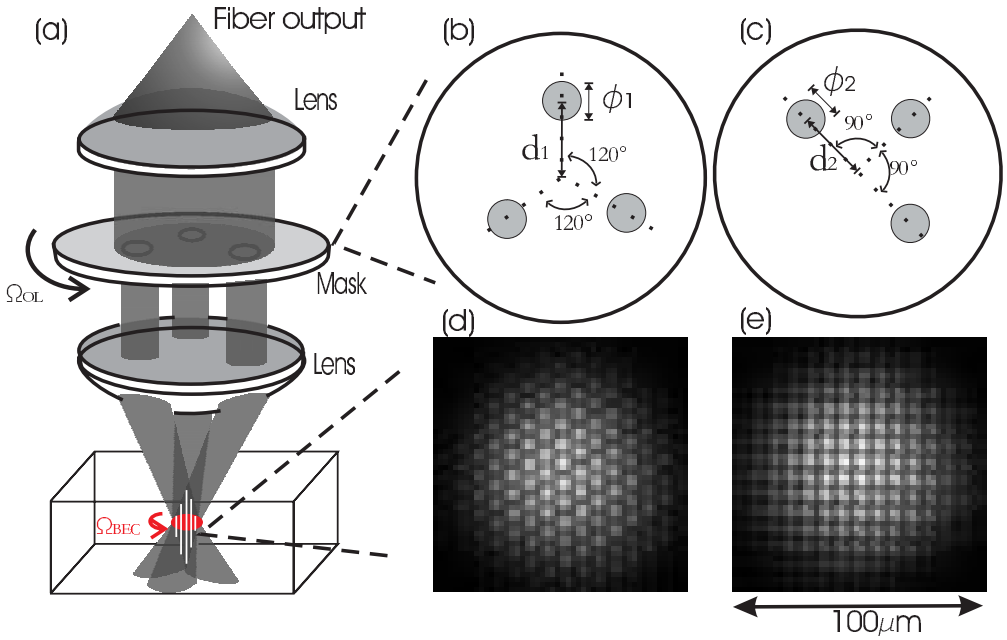

Figure A.1: (a) Schematic diagram of our setup for the rotating quasi-2D optical lattice. Layouts of the masks for a triangular (b) and square (c) optical lattices. (d) and (e) are pictures of triangular and square optical lattices, respectively. For details of the layouts see [70].

In the absence of pinning sites, a vortex lattice with areal density of vortices n_v will rotate at (approximately [71, 72]) $\Omega = (\frac{\hbar\pi}{m})n_v$. This suggests that for an optical lattice with an areal density of pinning sites n_{OL}, locking between the two lattices will be facilitated if the optical lattice rotates at the commensurate frequency $\Omega_c \equiv (\frac{\hbar\pi}{m})n_{OL}$.

We measure the angular difference $\theta_{OL} - \theta_{VL}$ between the orientation of the optical and vortex lattice in reciprocal space (see Figs. 2(a)–2(b)). Fig. A.2(c) shows $\theta_{OL} - \theta_{VL}$ as a function of the pinning strength with an optical lattice rotation rate $\Omega_{OL} = 1.133\Omega_c = 0.913\omega_r$. The strength of pinning is characterized by the ratio U_{pin}/μ (μ is the chemical potential of the condensate [73]), which gives the relative suppression of the superfluid density at pinning sites. We can see the initially random angular difference between the two lattices becomes smaller as the pinning strength U_{pin}/μ increases. For $U_{pin}/\mu \gtrsim 0.08$, the angular differences become very close to the locked value. Figure A.2(d) shows the phase diagram. The data points and error bars mark the minimum pinning strength $(U_{pin}/\mu)_{min}$ above which the lattices lock. We observe two distinct regimes. First, for small rotation-rate mismatch, $(U_{pin}/\mu)_{min}$ is rather independent of the rotation-rate mismatch. Second, for rotation-rate mismatch beyond the range indicated by the dashed line in Fig. A.2(d), angular orientation locking becomes very difficult for any U_{pin}/μ in our experiment. Instead, an ordered vortex lattice with random overall angular orientation observed at low U_{pin}/μ transforms into a disordered vortex arrangement at high U_{pin}/μ.

This box–like shape of the locked region in $U_{pin} - \Omega_{OL}$ space is worth considering. In a simple model, vortex motion in our system is governed by a balance of the pinning force and the Magnus force. The pinning force is $\overrightarrow{F}_{pin}(x) \propto U_{pin}/d$, where U_{pin} and d are the strength of the pinning potential and its period, respectively. The Magnus force, acting on a vortex moving with velocity $\overrightarrow{v}_{vortex}$ in a superfluid with velocity $\overrightarrow{v}_{fluid}$ is $\overrightarrow{F}_{mag}(x) \propto n(x)\,(\overrightarrow{v}_{vortex} - \overrightarrow{v}_{fluid}) \times \overrightarrow{\kappa}$ where $\overrightarrow{\kappa} = (\frac{h}{m})\hat{z}$, and $n(x)$ is the superfluid density. A locked vortex lattice will co-rotate with the pinning potential, giving $\overrightarrow{v}_{vortex}(r) = \overrightarrow{v}_{OL}(r) = \overrightarrow{\Omega}_{OL} \times$

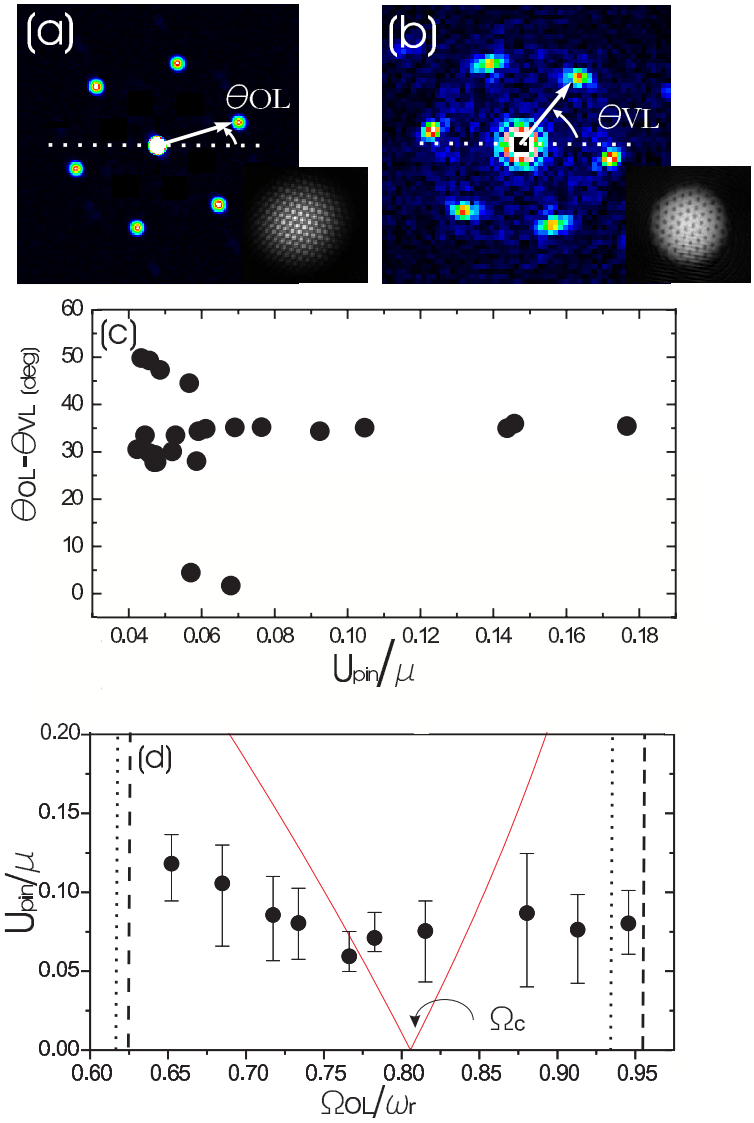

Figure A.2: (a) Triangular optical lattice and (b) vortex lattice in reciprocal space. Inset are the corresponding original real-space CCD-camera images. (c) The difference in orientation $\theta_{OL}-\theta_{VL}$ versus the strength of pinning U_{pin}/μ (the peak of the optical potential normalized by the condensate's chemical potential) for the rotation rates $\Omega_{OL} = 1.133\Omega_c = 0.913\omega_r$. With increasing pinning strength, $\theta_{OL}-\theta_{VL}$ tends towards its locked value [74]. (d) Minimum pinning strength needed for orientation locking between two lattices as a function of the rotation rate of the optical lattice. The dashed and dotted lines are discussed in the text.

$\overrightarrow{r}$, whereas the superfluid velocity in a solid-body approximation is $\overrightarrow{v}_{fluid}(r) = \frac{\hbar\pi}{m} n_v r\hat{\theta} = \overrightarrow{\Omega}_{fluid} \times \overrightarrow{r}$. Comparing the magnitudes of both forces at $r = R(\Omega)/2$, where $R(\Omega)$ is the centrifugal-force modified Thomas-Fermi radius, we obtain a minimum strength for pinning $(U_{pin}/\mu)_{min} \approx (\frac{1}{2\sqrt{3}} R(\Omega)/d) \times (\Omega_{OL} - \Omega_{fluid})/\Omega_c$.

What will be the fluid rotation rate Ω_{fluid} in the presence of the pinning potential? On the one hand, if vortices are tightly locked to the optical lattice sites, we have $\Omega_{fluid} = \Omega_c$. The minimum strength $(U_{pin}/\mu)_{min}$ resulting from this assumption is plotted as solid line in Fig. A.2(d). The lack of predicted decrease of $(U_{pin}/\mu)_{min}$ to zero around Ω_c may be due to long equilibration times in a very shallow pinning potential, as well as slight mismatches in alignment and initial rotation rate of the BEC and the pinning potential. The ease of orientation locking with increasing rotation rate mismatch is less easy to explain in this model. On the other hand, in the weak-pinning regime, the vortex lattice can accommodate a rotation rate mismatch by stretching/compressing away from the pinning sites. This allows the fluid to co-rotate with the optical lattice ($\Omega_{fluid} \approx \Omega_{OL}$) and reduce the Magnus force. This leads to a very low minimum pinning strength, as suggested by our data. However, the vortex lattice's gain in pinning energy decreases rapidly in the locked orientation when the mismatch between vortex spacing and optical lattice constant increases to the point where the outermost vortices fall radially in between two pinning sites. Then the preference for the locked angular orientation vanishes. This predicted limit is indicated by the vertical dotted lines in Fig. A.2(d).

In the absence of a pinning potential, the interaction energy of a square vortex lattice is calculated to exceed that of a triangular lattice by less than 1% [76], thus it is predicted [66, 67] that the influence of even a relatively weak square optical lattice will be sufficient to induce a structural transition in the vortex lattice. This structural cross-over of a vortex lattice is observed in our experiment. Figure A.3 shows how the vortex lattice evolves from triangular to square as the pinning strength increases. Over a wide range of pinning

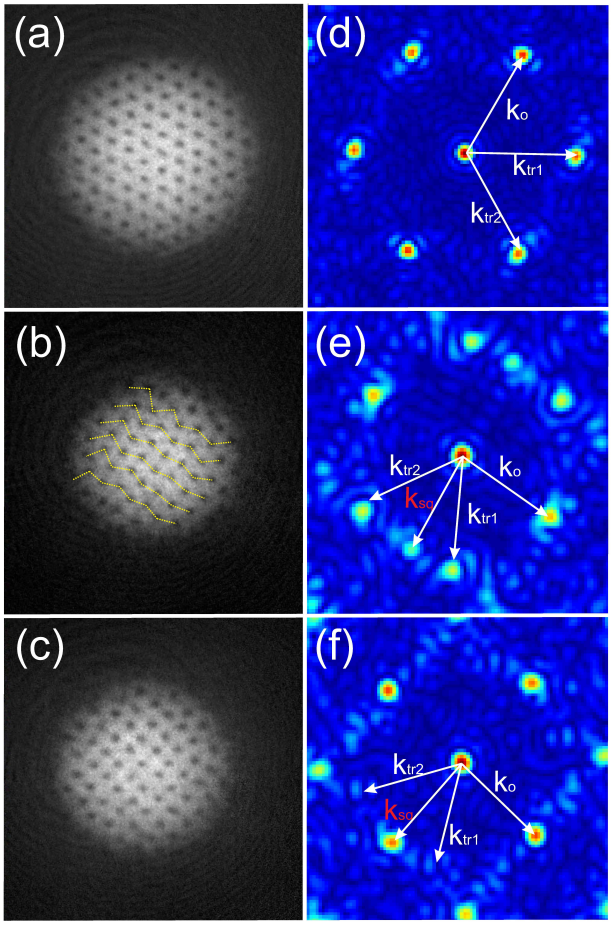

Figure A.3: Images of rotating condensates pinned to an optical lattice at $\Omega_{OL} = \Omega_c = 0.866\omega_r$ with pinning strength U_{pin}/μ=(a) 0.049 (b) 0.084 (c) 0.143, showing the structural cross-over of the vortex lattice. (a)–(c) are the absorption images of the vortex lattices after expansion. (d)–(f) are the Fourier transforms of the images in (a)–(c). k_o is taken by convention to be the strongest peak; k_{tr1}, k_{sq}, and k_{tr2} are at 60°, 90°, and 120°, respectively, from k_o.

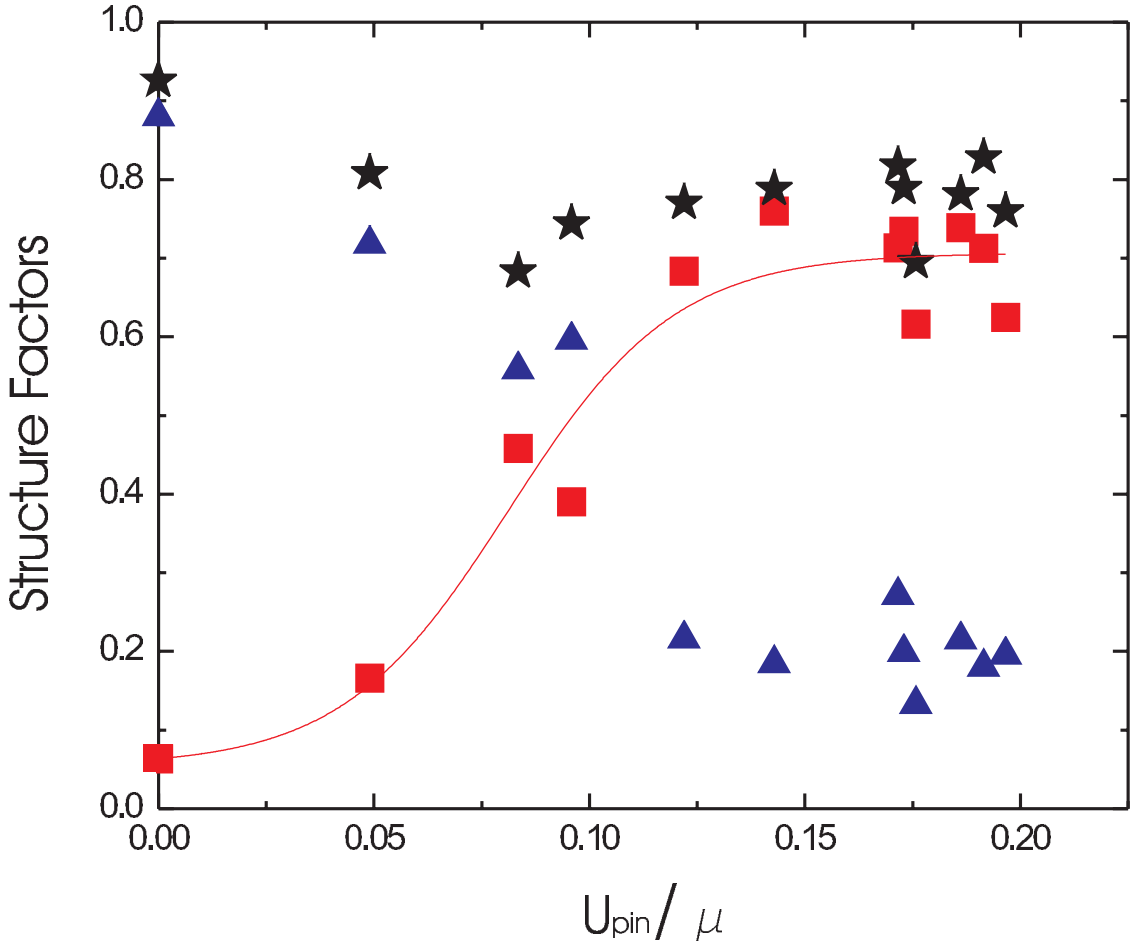

Figure A.4: Structure factors (a) $|S(k_{sq})|$ (■), (b) $|S(k_{tr})|$ (▲) (average of $|S(k_{tr1})|$ and $|S(k_{tr2})|$), and (c) $|S(k_o)|$ (★) versus the strength of the pinning lattice at the commensurate rotation rate Ω_c. $|S(k_{sq})|$ is fitted by [75]. The fitting leads to a maximum value 0.707 of $|S(k_{sq})|$. An ideal square vortex lattice would have $|S(k_{sq})|$=1.

strengths, we observe that there is always at least one lattice peak in reciprocal space that remains very strong. We define this peak to be k_o. Lattice peaks at 60° and 120° from k_o are referred to as k_{tr}, and, together with k_o, their strength is a measure of the continued presence of a triangular lattice. A peak at 90°, referred to as k_{sq}, is instead a signal for the squareness of the vortex lattice. With increasing pinning strength (Fig. A.3(a–c), or (d–f)), we see the triangle to square crossover evolve. At intermediate strengths ($U_{pin}/\mu = 0.084$), a family of zigzag vortex rows emerges, indicated by the dotted lines in Fig. A.3(b); in reciprocal space we see the presence of structure at k_{tr} and k_{sq}.

We quantify the crossover by means of an image-processing routine that locates each vortex core, replaces it with a point with unit strength, Fourier transforms the resultant pattern, and calculates structure factors $|S|$ [67] based on the strength of the images at lattice vectors k_{sq}, k_{tr}, and k_o. In Fig. A.4, we see with increasing optical potential the turn-on of $|S(k_{sq})|$ balanced by the turn-off of $|S(k_{tr})|$. We use a fitting function to smooth the noisy data of $|S(k_{sq})|$. The structure crossover takes place around $U_{pin}/\mu \approx 8\%$, in rough agreement with predictions of $U_{pin}/\mu \approx 5\%$ from numerical simulations [67] and $U_{pin}/\mu \approx 1\%$ from analytic theory for infinite lattices [66]. The fact that one lattice peak remains strong for all pinning strengths (the stars (★) in Fig. 4) suggests that as the pinning strength is increased, one family of vortex rows represented by k_o in Fourier space locks to the square pinning lattice and remains locked as the shape cross-over distorts the other two families of vortex rows into a square geometry. The effects of various rotation rates and optical potential strengths on the squareness of the vortex lattice is summarized in Fig. A.5. We surmise that there are a number of effects at play. When Ω_{OL} differs from Ω_c, pinning strength is required not only to deform the shape of the vortex lattice from triangular to square, but also to compress or expand it to match the density of the optical lattice sites. At higher optical intensities, we know from separate observations that imperfections in the rotation of the optical lattice lead to heating of the condensate, which may limit the obtainable strength of

the square lattice.

A dumbbell-shape lattice defect (Fig. A.6) is sometimes observed in the early stages of the square vortex lattice formation when $\Omega_{OL} > \Omega_c$. In the weak-pinning regime, the defect will relax towards the equilibrium configuration by pushing extra vortices at the edge of the condensate outside the system. Defects of this nature, involving extra (or missing) vortices, are the exception and not the rule in our observations, even for $\Omega_{OL} \neq \Omega_c$. In an infinite system, the physics of the lattice-lattice interaction would likely be dominated by these point defects. In our finite system, would-be incommensurate lattices can accommodate by stretching or compressing.

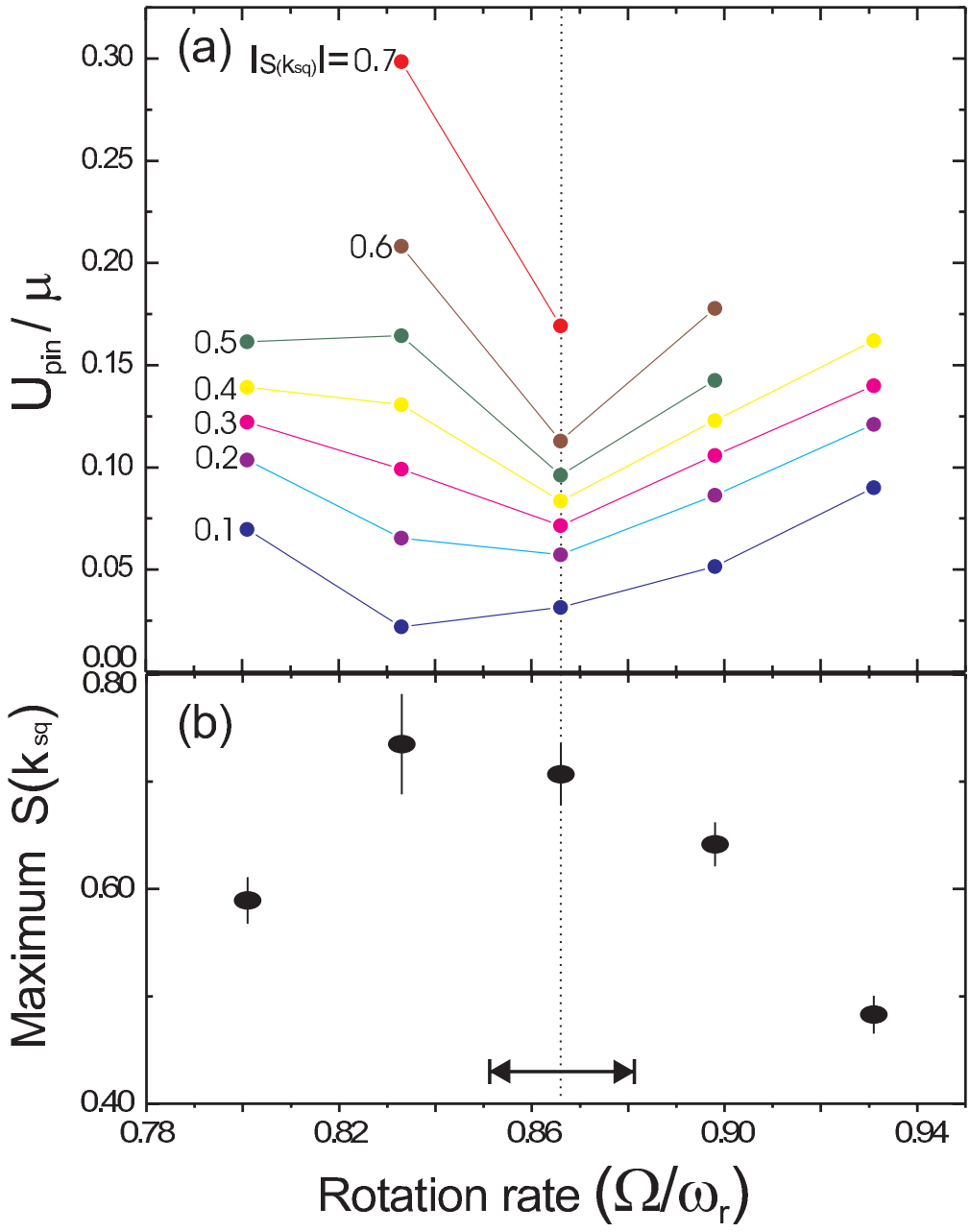

Figure A.5: Effect of square pinning lattice. (a) Contours of $|S(k_{sq})|$ are plotted, showing the effect of the rotation rate and pinning strength on the squareness of the vortex lattice. (b) The maximum observed squareness. In (a) and (b), for each rotation rate, the data points are extracted from fits such as that shown in Fig. A.4 for $\Omega_{OL} = \Omega_c$. The vertical dotted line plus arrow shows the possible range of Ω_c consistent with the uncertainty in n_{OL}.

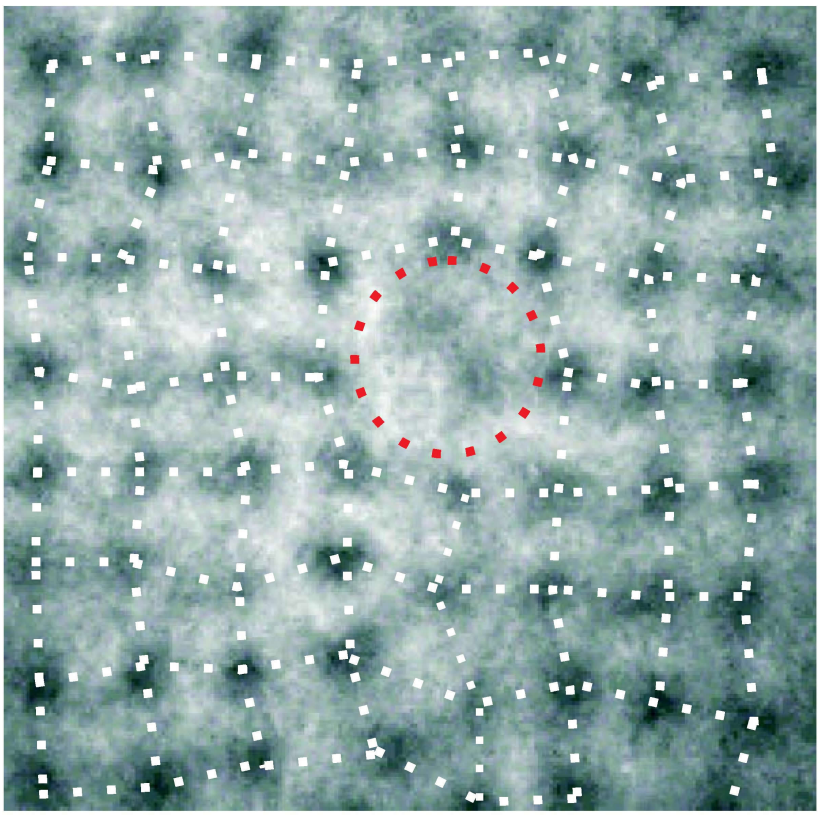

Figure A.6: Image of a dumbbell-shape defect consisting of two vortices locked to one pinning site during the formation of the square vortex lattice. Dotted lines are to guide the eye.

Appendix B

Vortex proliferation in the Berezinskii-Kosterlitz-Thouless regime on a two-dimensional lattice of Bose-Einstein condensates [1, 3]

Appendices We observe the proliferation of vortices in the Berezinskii-Kosterlitz-Thouless regime on a two-dimensional array of Josephson-coupled Bose-Einstein condensates. As long as the Josephson (tunneling) energy J exceeds the thermal energy T, the array is vortex-free. With decreasing J/T, vortices appear in the system in ever greater numbers. We confirm thermal activation as the vortex formation mechanism and obtain information on the size of bound vortex pairs as J/T is varied.

One of the defining characteristics of superfluids is long-range phase coherence [77], which may be destroyed by quantum fluctuations, as in the Mott-insulator transition [34, 78], or thermal fluctuations, e.g. in one-dimensional Bose gases [79, 80] and in a double-well system [81]. In two dimensions (2D), Berezinskii [6], Kosterlitz and Thouless [7] (BKT) developed an elegant description of thermal phase fluctuations based on the unbinding of vortex-antivortex pairs, i.e. pairs of vortices of opposite circulation. The BKT picture applies to a wide variety of 2D systems, among them Josephson junction arrays (JJA), i.e. arrays of superfluids in which phase coherence is mediated via a tunnel coupling J between adjacent sites. Placing an isolated (*free*) vortex into a JJA is thermodynamically favored if its free energy $F = E - TS \leq 0$. In an array of period d the vortex energy diverges with array size R as $E \approx J \log(R/d)$ [82], but may be offset by an entropy gain $S \approx \log(R/d)$ due to the available $\approx R^2/d^2$ sites. This leads to a critical condition $(J/T)_{crit} \approx 1$ independent

of system size, below which free vortices will proliferate. In contrast, *tightly bound* vortex-antivortex *pairs* are less energetically costly and show up even above $(J/T)_{crit}$. The overall vortex density is thus expected to grow smoothly with decreasing J/T in the BKT crossover regime.

Transport measurements, both in continuous superfluids [48, 49] and superconducting JJA [50] have confirmed the predictions of BKT, without however directly observing its microscopic mechanism, vortex-antivortex unbinding. A recent beautiful experiment [9] in a continuous 2D Bose gas measured the phase-phase decay function through the BKT crossover, and saw evidence for thermal vortex formation. For related theoretical studies see e.g. [84]. In this work we present more detailed vortex-formation data, collected in a 2D array of BECs with experimentally controllable Joephson couplings. The system was studied theoretically in [85].

Our experiment starts with production of a partially Bose-condensed sample of ^{87}Rb atoms in a harmonic, axially symmetric magnetic trap with oscillation frequencies $\{\omega_{x,y}, \omega_z\} = 2\pi\{6.95, 15.0\}$ Hz. The number of *condensed* atoms is kept fixed around 6×10^5 as the temperature is varied. We then transform this system into a Josephson junction array, as illustrated in Fig. B. In a $10\,s$ linear ramp, we raise the intensity of a 2D hexagonal optical lattice [86] of period $d = 4.7\mu m$ in the x-y plane. The resulting potential barriers of height V_{OL} between adjacent sites [Fig.B(b)] rise above the condensate's chemical potential around $V_{OL} \approx 250 - 300\,Hz$, splitting it into an array of condensates which now communicate only through tunneling. This procedure is adiabatic even with respect to the longest-wavelength phonon modes of the array [87, 88] over the full range of V_{OL} in our experiments. Each of the $\approx$ 190 occupied sites (15 sites across the BEC diameter $2 \times R_{TF} \approx 68\,\mu m$ [89]) now contains a macroscopic BEC, with $N_{well} \approx 7000$ condensed atoms in each of the central wells at a temperature T that can be adjusted between $30 - 70\,nK$. By varying V_{OL} in a range between $500\,Hz$ and $2\,kHz$ we tune J between $1.5\,\mu K$ and $5\,nK$, whereas the "charging"

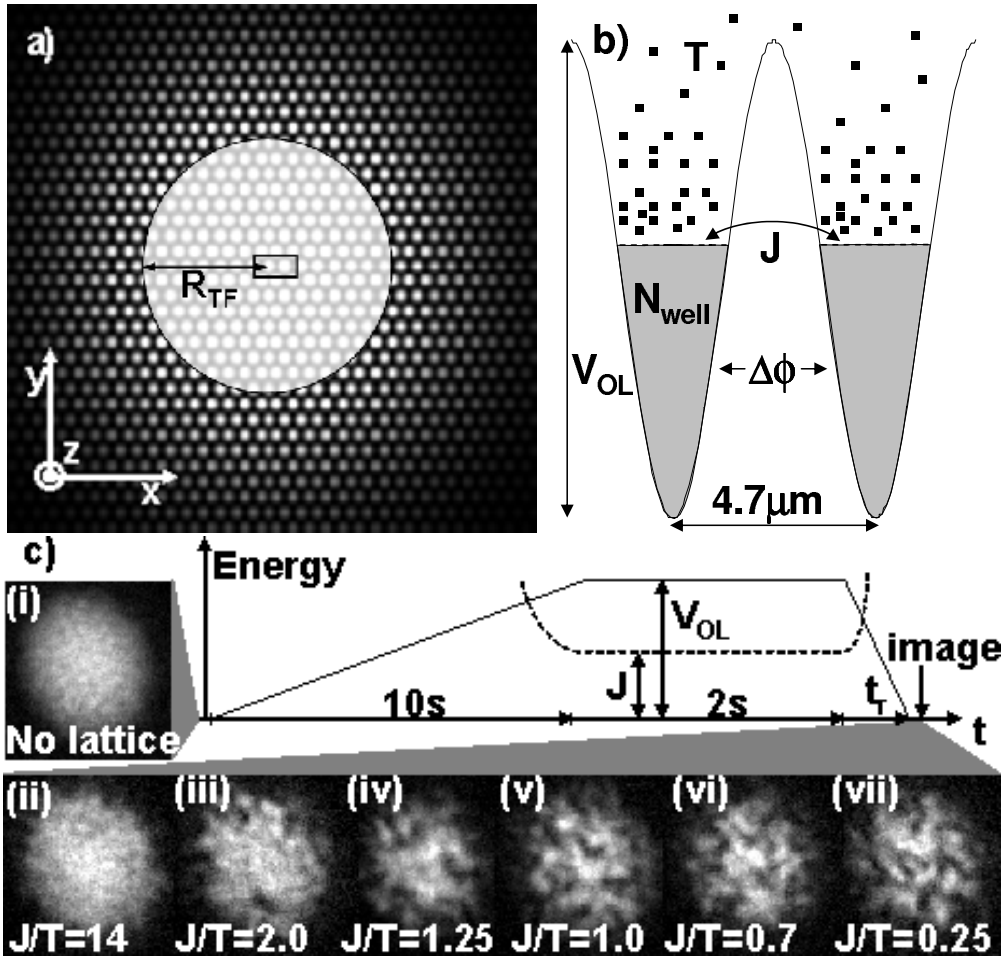

Figure B.1: Experimental system. (a) 2D optical lattice intensity profile. A lattice of Josephson-coupled BECs is created in the white-shaded area. The central box marks the basic building block of our system, the double-well potential shown in (b). The barrier height V_{OL} and the number of condensed atoms per well, N_{well}, control the Josephson coupling J, which acts to lock the relative phase $\Delta\phi$. A cloud of uncondensed atoms at temperature T induces thermal fluctuations and phase defects in the array when $J < T$. (c) Experimental sequence: A BEC (i) is loaded into the optical lattice over $10\,s$, suppressing J to values around T. We allow $2\,s$ for thermalization. To probe the system, we ramp off the lattice on a faster timescale t_r [83] and take images of the recombined condensate. When J is reduced below T (ii)-(vii), vortices (dark spots) appear as remnants of the thermal fluctuations in the array.

energy E_c, defined in [77], is on the order of a few pK, much smaller than both J and T. In this regime, thermal fluctuations of the relative phases $\Delta\phi_{Th} \approx \sqrt{T/J}$ are expected, while quantum fluctuations $\Delta\phi_Q \approx (E_c/4J)^{1/4}$ are negligible [77].

The suppression of the Josephson coupling greatly suppresses the energy cost of phase fluctuations in the x-y plane, *between* condensates, $J[1-\cos(\Delta\phi)]$, compared to the cost of axial (z) phase fluctuations *inside* the condensates [51]. As a result, axial phase fluctuations remain relatively small, and each condensate can be approximated as a single-phase object [90].

After allowing $2\,s$ for thermalization, we initiate our probe sequence. We first take a nondestructive thermometry image in the x-z plane, from which the temperature T and, from the axial condensate size R_z, the number of condensed particles per well, N_{well}, is obtained (see below). To observe the phase fluctuations we then turn down the optical lattice on a time-scale t_r [83], which is fast enough to trap phase winding defects, but slow enough to allow neighboring condensates to merge, provided their phase difference is small. Phase fluctuations are thus converted to vortices in the reconnected condensate, as has been observed in the experiments of Scherer *et al.* [37]. We then expand the condensate by a factor of 6 and take a destructive image in the x-y plane.

Figure B(c) illustrates our observations: (ii)-(vii) is a sequence of images at successively smaller J/T (measured in the center of the array [91]). Vortices, with their cores visible as dark "spots" in (iii)-(vii), occur in the BEC center around $J/T = 1$. Vortices at the BEC edge appear earlier, as here the magnetic trap potential adds to the tunnel barrier, suppressing the *local* J/T below the quoted value. That the observed "spots" are indeed circulation-carrying vortices and antivortices is inferred from their slow $\approx 100\,ms$ decay after the optical lattice ramp-down, presumably dominated by vortex-antivortex annihilation. From extensive experiments on vortices in our system we know that circulation-free "holes" fill so quickly due to positive mean field pressure, that they do not survive the pre-imaging expansion.

Vortices with identical circulation would decay by dissipative motion to the BEC edge, in our trap over $\gtrsim 10\,s$.

To investigate the thermal nature of phase fluctuations, we study vortex activation while varying J at different temperatures. For a quantitative study, accurate parameter estimates are required. The Josephson-coupling energy J is obtained from 3D numerical simulations of the Gross-Pitaevskii equation (GPE) for the central double-well system [92, 81] [Fig.B(b)], self-consistently including mean-field interactions of both condensed and uncondensed atoms [93]. A useful approximation for J in our experiments is [91]: $J(V_{OL}, N_{well}, T) \approx N_{well} \times 0.315\,nK \exp[N_{well}/3950 - V_{OL}/244Hz](1 + 0.59\,T/100nK)$. The finite-$T$ correction to J arises from both the lifting-up of the BEC's chemical potential and the axial compression by the thermal cloud's repulsive mean field, but does *not* take into account the effects of phase fluctuations on J (in condensed-matter language, we calculate the *bare* J). N_{well} is determined by comparison of the experimentally measured R_z, to $R_z(V_{OL}, N_{well}, T)$ obtained from GPE simulations. Both experimental and simulated R_z are obtained from a fit to the distribution of condensed and uncondensed atoms, to a Thomas-Fermi profile plus mean-field-modified Bose function [93]. In determination of all J values, there is an overall systematic multiplicative uncertainty $\Delta J/J = \overset{\times}{\div}1.6$, dominated by uncertainties in the optical lattice modulation contrast, the absolute intensity calibration, and magnification in the image used to determine N_{well}. In comparing J for "hot" and "cold" clouds (see Fig. B) there is a relative systematic error of 15% associated with image fitting and theory uncertainties in the thermal-cloud mean-field correction to J.

The qualitative results of our work are consistent whether we use an automated vortex-counting routine or count vortices by hand, but the former shows signs of saturation error at high vortex density, and the latter is vulnerable to subjective bias. As a robust vortex-density surrogate we therefore use the "roughness" $\mathcal{D}$ of the condensate image caused by the vortex cores. Precisely, we define $\mathcal{D}$ as the normalized variance of the measured col-

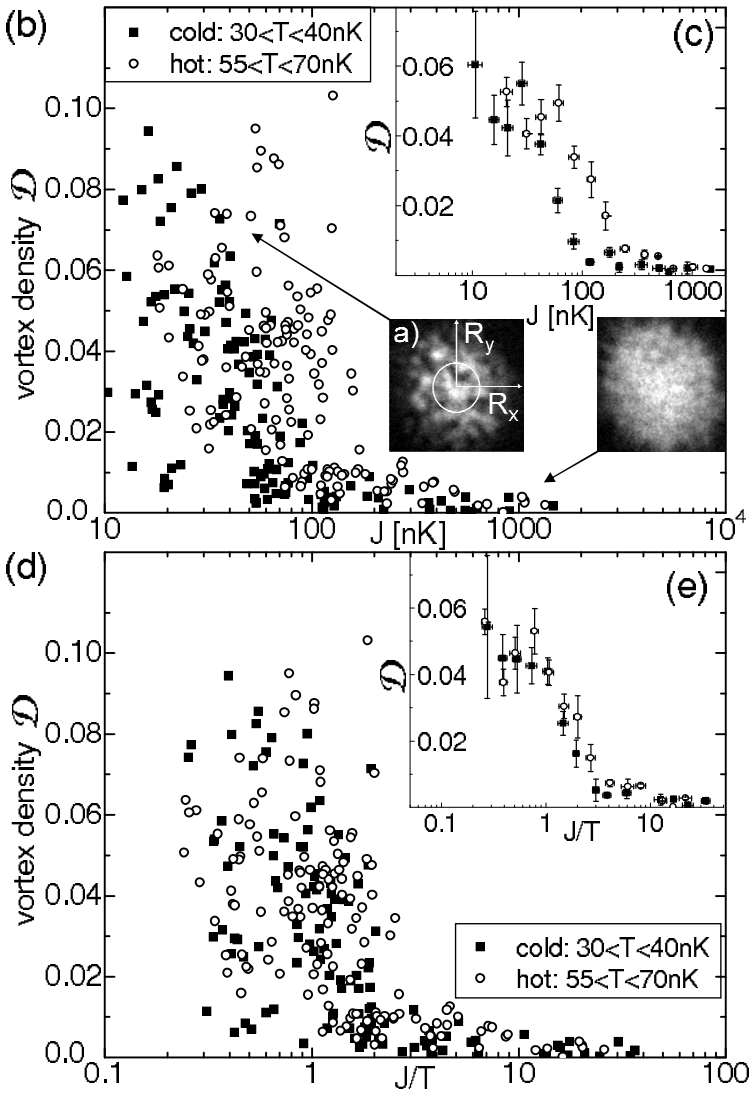

Figure B.2: Quantitative study of vortices. The areal density of vortices is quantified by the plotted $\mathcal{D}$ defined in the text. $\mathcal{D}$ is extracted only from the central 11% of the condensate region [circle in inset (a)] to minimize effects of spatial inhomogeneity. (b) $\mathcal{D}$ vs J for two datasets with distinct "cold" and "hot" temperatures. Each point represents one experimental cycle. The increase in $\mathcal{D}$ with decreasing $J \lesssim 100\,nK$ signals the spontaneous appearance of vortices, while the "background" $\mathcal{D} \lesssim 0.01$ for $J \gtrsim 200\,nK$ is not associated with vortices. Vortices clearly proliferate at larger J for the "hot" data, indicating thermal activation as the underlying mechanism. The large scatter in $\mathcal{D}$ at low J is due to shot noise on the small average number of vortices in the central condensate region. (c) same data as in (b), but averaged within bins of size $\Delta[\log(J)] = 0.15$. Error bars of $\mathcal{D}$ are standard errors. (d) same data as (b), but plotted vs J/T. "Cold" and "hot" datasets almost overlap on what appears to be a universal vortex activation curve, as confirmed by averaging [inset (e)], clearly revealing the underlying competition of J and T.

umn density profile from a fit to a smooth finite-T Bose profile [93], with a small constant offset subtracted to account e.g. for imaging noise. To limit spatial inhomogeneity in J, caused by spatially varying condensate density and optical lattice intensity, to $< 10\%$, $\mathcal{D}$ is extracted only from the central 11% of the condensate area which contains 20 lattice sites [Fig. B(a)]. Comparison to automated vortex-counts shows that $\mathcal{D}$ is roughly linear in the observed number of vortices, irrespective of the sign of their circulation, with a sensitivity of ≈ 0.01/vortex.

Figure B shows results of our quantitative study. In Fig. B(b), we plot $\mathcal{D}$ vs J for two datasets with distinct temperatures. At large $J \gtrsim 200\,nK$ a background $\mathcal{D} \lesssim 0.01$ is observed, that is not associated with vortices, but due to residual density ripples remaining after the optical lattice ramp-down. Vortex proliferation, signaled by a rise of $\mathcal{D}$ above ≈ 0.01, occurs around $J \approx 100\,nK$ for "hot" BECs and at a distinctly lower $J \approx 50\,nK$ for "cold" BECs [confirmed by the averaged data shown in Fig. B(c)], indicating thermal activation as the vortex formation mechanism. Plotting the same data vs J/T in Fig. B(d) shows collapse onto a universal vortex activation curve, providing strong evidence for thermal activation. A slight residual difference becomes visible in the averaged "cold" vs "hot" data [Fig.B(e)], perhaps because of systematic differences in our determination of J at different temperatures.

The vortex density $\mathcal{D}$ by itself provides no distinction between *bound* vortex-antivortex *pairs* and *free* vortices. In the following we exploit the flexibility of optical potentials to distinguish free or loosely bound vortices from tightly bound vortex-antivortex pairs. A "slow" optical lattice ramp-down allows time for tightly bound pairs to annihilate before they can be imaged. By slowing down the ramp-down duration τ [inset of Fig. B (a)], we therefore selectively probe vortices at increasing spatial scales. This represents an attempt to approach the "true" BKT vortex unbinding crossover that is complementary to transport measurements employed so successfully in superconductive and liquid Helium systems.

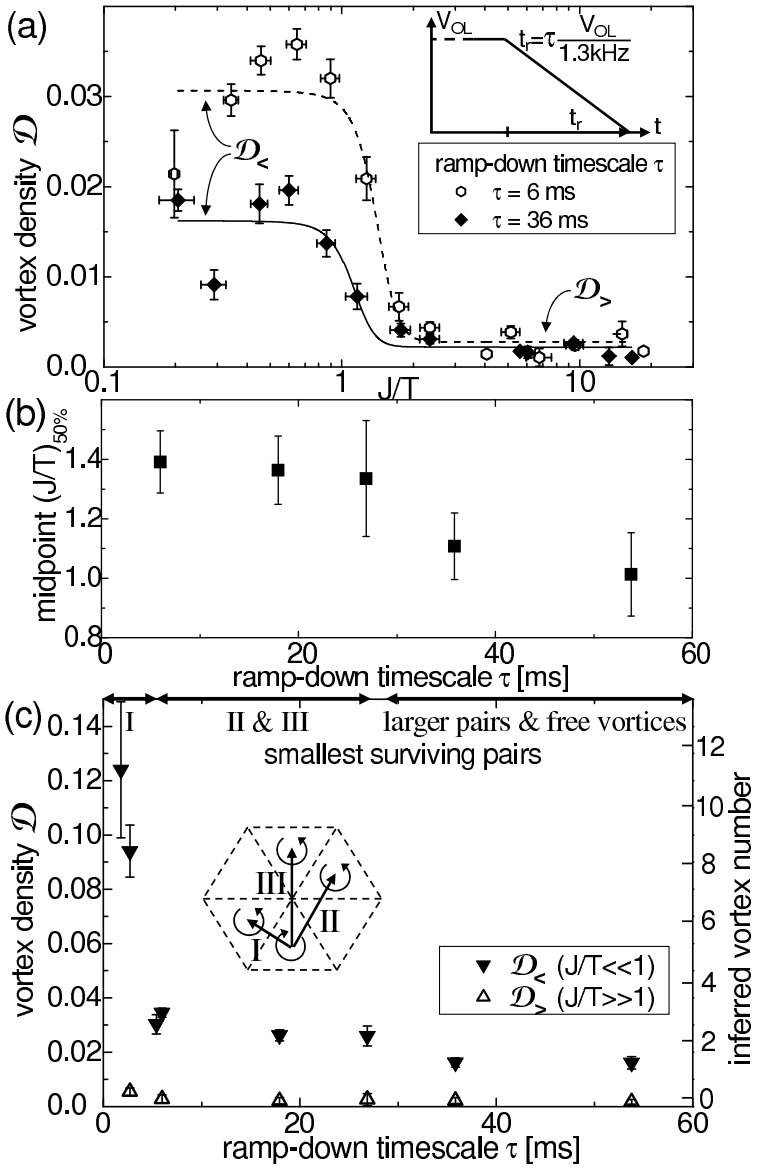

Figure B.3: (a) Vortex density $\mathcal{D}$ probed at different optical lattice ramp-down timescales τ. A slow ramp provides time for tightly bound vortex-antivortex pairs to annihilate, allowing selective counting of loosely bound or free vortices only, whereas a fast ramp probes both free and tightly bound vortices. A fit to the vortex activation curve determines its midpoint $(J/T)_{50\%}$, its $27\% - 73\%$ width $\Delta(J/T)_{27-73}$, and the limiting values $\mathcal{D}_<$ ($\mathcal{D}_>$) well below (above) $(J/T)_{50\%}$. (b) A downshift in $(J/T)_{50\%}$ is seen for slow ramps, consistent with the occurrence of loosely bound or free vortices at lower J/T only. (c) Mapping between ramp-down timescale τ and estimated size of the smallest pairs surviving the ramp (upper axis). The difference $\mathcal{D}_< - \mathcal{D}_>$ measures the number of vortices surviving the ramp (right axis). Comparison to simulated vortex distributions yields a size estimate of the smallest surviving pairs (upper axis). Inset: smallest possible pair sizes in a hexagonal array, I: $d/\sqrt{3}$, II: d, III: $2d/\sqrt{3}$.

Figure B(a) shows vortex activation curves, probed with two different ramp-down times. Two points are worth noticing: First, a slow ramp compared to a fast one shows a reduction of the vortex density $\mathcal{D}_<$ in arrays with fully randomized phases at low J/T. The difference directly shows the fraction of tightly bound pairs that annihilate on the long ramp. Second, a slower ramp shows vortex activation at lower $(J/T)_{50\%}$, confirming that free or very loosely bound vortices occur only at higher T (lower J). Specifically, the data clearly show a range around $J/T \approx 1.4$ where only tightly bound pairs exist. Figure B(b) quantitatively shows the shift of $(J/T)_{50\%}$ from 1.4 to 1.0 with slower ramp time. We can make a crude mapping of the experimental ramp-down time-scale to theoretically more accessible vortex-antivortex pair sizes as follows: In Fig. B(c), we see the decrease of the saturated (low-J/T) vortex density $\mathcal{D}_<$ with increasing ramp timescale τ. The right axis shows the inferred number of vortices that survived the ramp. We compare this number of surviving vortices to simulations [94] of a 20-site hexagonal array with random phases. In these simulations we find, on average, a total of 10 vortices, 6 of which occur in nearest-neighbor vortex-antivortex pairs [configuration I in Fig. B(c)], 1.7 (0.4) occur in configuration II (III) respectively, and 1.9 occur in larger pairs or as free vortices. Experimentally ≈ 11 vortices are observed for the fastest ramps, in good agreement with the expected *total* number of vortices. For just somewhat slower ramps of $\tau \approx 5\,ms$, only 3 vortices survive, consistent with only vortices in configuration II & III or larger remaining (indicated in Fig. B, top axis) [95]. For $\tau \gtrsim 30\,ms$ ramps less than 2 vortices remain, according to our simulations spaced by more than $2d/\sqrt{3}$. Thus we infer that ramps of $\tau \approx 30\,ms$ or longer allow time for bound pairs of spacing $\lesssim 2d/\sqrt{3}$ to decay before we observe them. The downward shift of $(J/T)_{50\%}$ in Fig. B(b) thus tells us that loosely bound pairs of size larger than $2d/\sqrt{3}$, or indeed free vortices, do not appear in quantity until $J/T \leq 1.0$, whereas more tightly bound vortex pairs appear in large number already for $J/T \leq 1.4$.

A further interesting observation concerns the width of the vortex activation curve.

The relative width, determined from fits to data such as the ones shown in Fig. B(a), is $\Delta(J/T)_{27-73}/(J/T)_{50\%} \approx 0.3$, independent of ramp-down duration. This width is neither as broad as in a double-well system [96, 81], where the coherence factor rises over a range $\Delta(J/T)_{27-73}/(J/T)_{50\%} \approx 1.4$, nor as broad as expected from our simulations [94] of an array of uncoupled phases, each fluctuating independently with $\Delta\phi_{RMS} = \sqrt{T/J}$, for which we find $\Delta(J/T)_{27-73}/(J/T)_{50\%} \approx 0.85$. Presumably collective effects in the highly multiply connected lattice narrow the curve. On the other hand, the width is 3 times larger than the limit due to spatial inhomogeneity in J, suggesting contributions to the width due to finite-size effects or perhaps revealing the intrinsically smooth behavior of vortex activation in the BKT regime.

In conclusion, we have probed vortex proliferation in the BKT regime on a 2D lattice of Josephson-coupled BECs. Allowing variable time for vortex-antivortex pair annihilation before probing the system provides a time-to-length mapping, which reveals information on the size of pairs with varying J/T.